

**CRYSTAL STRUCTURE AND OXIDATION
BEHAVIOR OF AL-CONTAINING STAINLESS
STEEL COATINGS PRODUCED BY
CRYOMILLING AND SPARK PLASMA SINTERING**

By

AL-MATHAMI ABDULAZIZ

*Department of Mining and Materials Engineering
McGill University, Montreal*

March 2010

A Thesis submitted to the
Faculty of Graduate Studies and Research
in a partial fulfillment of the
requirements for the degree of
Doctor of Philosophy

ABSTRACT

Three austenitic 316LSS alloys containing 0, 2 and 6wt% Al were prepared by cryomilling and Spark Plasma Sintering (SPS). It was shown that aluminum influences the FCC to BCC strain induced phase transformation that occurs during milling and also the FCC recovery during heat treatment and SPS consolidation. The Al-containing SS had accelerated strain induced transformation in the early stage of milling, while the rate of transformation became similar thereafter for all systems. The degree to which the induced BCC structure reverted to FCC was found dependent upon the Al content. Complete recovery of the FCC during heat treatment was achieved between 565 to 594 °C for nSS6Al and 605 to 618 °C for nSS2Al, depending on the heating rate. However, heat treatment of nSS0Al up to 1000 °C resulted in incomplete reversion of the strain induced structure. The SPS process was found to minimally influence the FCC recovery compared to conventional powder consolidation heat treatments. The energy supplied by the SPS process was insufficient to overcome the activation energy governing the rearrangement of dislocations required to complete the FCC recovery.

The modification of the composition of 316LSS combined with a grain refinement to the nanometer level was investigated to determine the potential gain in oxidation resistance on coatings produced using the SPS technique. For the base alloy, the increased number of diffusion paths present in nanostructured materials yielded a thicker oxide scale, when compared to conventional SS, and this independently on the tested oxidation temperature (500 °C, 800 °C and 1000 °C). For the nanostructured SS, the scale had an enriched Cr-content which improves the resistance to static and cyclic oxidation, and adherence to the substrate. Aluminum was also added at concentrations of 2 and 6 wt% to the base SS,

which caused the scale composition to change to a continuous double layer consisting of an inner Al_2O_3 and an outer Cr_2O_3 for both alloys when oxidized at $1000\text{ }^\circ\text{C}$ and for the 6 wt% Al sample when oxidized at $800\text{ }^\circ\text{C}$. The activation energy for oxidation of the nanostructured coatings was approximately half of the one for the conventional SS. The oxidation rate constant for the Al-containing SS alloys studied was found to be lower than for the Al-free grades, which is associated with the Al_2O_3 layer providing a diffusion barrier. However, the conventional SS had a lower oxidation rate constant than the nanostructured alloy because of the lower volume fraction of grain boundaries providing a slower diffusion of the same elements composing the scale.

RESUME

Trois alliages austénitiques 316LSS contenant entre 0,2 et 6 % massique d'aluminium ont été préparé par broyage à froid et frittage à plasma d'étincelles (Spark Plasma Sintering : SPS). Il a été montré que l'aluminium influence la transformation, induite par tension, Cubique Face Centré (CFC) à Cubique Centré (CC) qui a lieu durant le broyage et aussi le rétablissement de la phase CFC durant le chauffage et la consolidation par SPS. L'alliage SS contenant de l'aluminium à une transformation induite par tension accélérée dans les premières étapes de broyage, tandis que le taux de transformation devient similaire ensuite pour tous les systèmes. Le degré auquel la structure CC retourne en CFC a été trouvé dépendant du pourcentage d'aluminium contenu. La récupération complète de la phase CFC pendant le traitement thermique a été achevé entre 565 et 594 °C pour nSS6Al et entre 605 et 618 °C pour nSS2Al, dépendamment de la vitesse de chauffage. Par contre, un traitement thermique de nSS0Al à plus de 1000 °C résulte en un retour incomplet de la structure induite par tension. Il a été montré que le procédé par SPS influence très peu la récupération de la phase CFC comparé aux traitements thermiques de consolidations de poudres conventionnels. L'énergie apportée par le procédé SPS n'est pas assez importante pour dépasser l'énergie d'activation, qui gouverne le réarrangement des dislocations, requis pour la récupération de la phase CFC.

Pour déterminer le gain potentiel en résistance à l'oxydation des revêtements produits par SPS, la modification de la composition de 316LSS combinée à une réduction de la taille de grain à l'échelle du nanomètre ont été étudiées. Pour l'alliage de base, le nombre accru de voies de diffusion présent dans les matériaux nanostructurés produit un dépôt plus épais

d'oxyde, comparé aux SS conventionnels, et ce indépendamment des températures d'oxydations testées (500 °C, 800 °C et 1000 °C). Pour les SS nanostructurés, le dépôt est enrichi en Cr, ce qui augmente la résistance à l'oxydation statique et cyclique, et l'adhérence au substrat. De l'aluminium a aussi été introduit avec une concentration de 2 et 6 % massique à l'alliage SS de base, ce qui a causé un changement de la composition du dépôt pour une double couche consistant en une phase intérieure d' Al_2O_3 et extérieure de Cr_2O_3 pour les deux alliages quand ils sont oxydés à une température de 1000 °C et seulement pour l'échantillon avec 6 % massique d'aluminium quand oxydés à 800 °C. L'énergie d'activation pour l'oxydation des revêtements nanostructurés est approximativement la moitié de celle des SS conventionnels. La constante de taux d'oxydation pour les SS étudiés contenant de l'aluminium a été trouvée comme plus basse que celle pour les alliages sans aluminium, ce qui peut être associé à la couche d' Al_2O_3 qui fournit une barrière de diffusion. Cependant, le SS conventionnel a une constante de taux d'oxydation plus faible que celle des alliages nanostructurés parce que la fraction volumique des joints de grains est plus faible et donc produit une diffusion plus lente des mêmes éléments composant le dépôt.

ACKNOWLEDGMENTS

All praises and glory to my God who alone made this work to be accomplished.

I wish to express my appreciation with deep gratitude to Professor M. Brochu for his excellent supervision, guidance, encouragement and support during the entire project. I am especially thankful for his extensive long hours and days spent with me. His beneficial suggestions and discussions throughout the project were the keys for success of this work.

I would like to thank all lab technicians for their valuable help in carrying out the experiments, mainly H. Campbell, and M. Riendeau for their hours spent to help me in the analysis work using XRD, SEM, and EDS. Special thanks go to my great nano research group for the amazing 4 years we spent together that were full of help, laughs and good memories.

I would like also to thank Natural Resources Canada (NRCan) for assistance with DSC and XPS measurements, Dwight Lynch and Jason Milligan for assistance with SPS samples consolidation and Saudi Aramco Company, which generously awarded financial support to me.

Finally, I would like to extend my appreciation and gratitude to my Mom, Dad, Wife and my children Turki, Hanin and Reema for their pray, endless love and support throughout my life.

<i>CONTENTS</i>	<i>page</i>
INTRODUCTION	1
LITERATURE REVIEW	5
2.1 Synthesis of Nanostructured Powders Using Cryomilling	5
2.1.1 Nanostructure Evolution Mechanism of Cryomilled Powders	6
2.1.2 Mechanism of Mechanical Alloying Using Cryomilling	7
2.1.3 Alloying and Formation of Nanostructured Stainless Steel and Al-Containing Powders Using Cryomilling	8
2.1.4 High Temperature Stability of Cryomilled Al-Containing Powders	11
2.2 Deformation and Phase Transformation of Stainless Steel during Mechanical alloying and Heat Treatment	12
2.2.1 Deformation Mechanisms and Stability of Austenite Stainless Steels	13
2.2.2 Phase Transformation of Austenite Stainless Steels during Mechanical Alloying and Milling	14
2.2.3 Phase Transformation of Austenite Stainless Steels during Heat Treatment	16
2.3 Spark Plasma Sintering	17
2.3.1 Mechanism of Spark Plasma Sintering	18
2.3.2 Advantage of Spark Plasma Sintering	21
2.4 Oxidation	22
2.5 Thermodynamic Consideration at High Temperature	24
2.6 Oxidation Kinetic	28
2.6.1 Linear Oxidation Rates	31
2.6.2 Parabolic Oxidation Reaction Rates	32
2.6.3 Logarithmic Reaction Rates	34
2.6.4 Combination of Simple Rate Equations	36
2.7 Oxidation of Austenitic Stainless Steel	36

2.8	Aluminum Oxide at High Temperature	40
2.8.1	Properties and Behaviors of Aluminum Oxide in Alloys	40
2.8.2	Oxidation Performance of Al-containing Alloys	41
2.8.3	Difficulties in Forming Protective Aluminum Oxide	45
2.8.4	Aluminum and Aluminum Oxide in Nanostructured Materials	49
METHODOLOGY		55
3.1	Raw Materials	55
3.2	Mechanical Alloying and Nano-Grain Structuring	56
3.3	Powders Consolidation (Hot Press)	58
3.4	Spark Plasma Sintering (SPS)	59
3.5	Measurement of Surface Area Using BET Technique	61
3.6	High Temperature Preparation and Evaluations	62
3.6.1	Powders Annealing	62
3.6.2	High Temperature Oxidation	63
3.6.3	TGA Experiments	63
3.7	Samples Characterizations and Analysis	65
3.7.1	XRD	65
3.7.2	Scanning Electron Microscope (SEM)	66
3.7.3	Transmission Electron Microscope (TEM)	68
3.7.4	X-Ray Photoelectron Spectrometer (XPS)	69
3.7.5	Differential Scanning Calorimetry (DSC)	70
CRYSTAL STRUCTURE, TRANSFORMATION AND THERMAL STABILITY OF NANOSTRUCTURED 316LSS ALLOYED WITH 2 AND 6 wt% ALUMINUM		72
4.1	Introduction	72
4.2	Experimental	74
4.3	Results and Discussion	75
4.3.1	Phase Transformation and grain refinement during Mechanical alloying	75
4.3.2	Phase Transformation during Heat Treatment	80

4.3.3	Grain Growth during Heat Treatment	87
4.3.4	Influence of Precipitations and Heat Treatment Duration on the Grain Growth Behavior	91
4.4	Conclusions	96
MICROSTRUCTURE AND TRANSFORMATION OF AL-CONTAINING NANOSTRUCTURED 316L SS DURING SPS		98
5.1	Introduction	98
5.2	Experimental	100
5.3	Results and Discussions	103
5.3.1	Cryomilling and Microstructure Evolution of the SPS Consolidated Coating	103
5.3.2	Phase Transformation and Grain Growth During SPS and Comparison to Heat Treatment	107
5.3.3	Effect of Process, Phase Microstructure and Consolidation Process on the Hardness	114
5.4	Conclusions	115
THERMAL STABILITY AND OXIDATION BEHAVIOR OF AL-CONTAINING NANOCRYSTALLINE POWDERS PRODUCED BY CRYOMILLING		117
6.1	Introduction	117
6.2	Experimental	119
6.3	Engineering the Starting Powders	120
6.4	Results and Discussions	122
6.5	Conclusions	132
OXIDATION BEHAVIOR OF AL-CONTAINING STAINLESS STEEL COATINGS PRODUCED BY CRYOMILLING AND SPS		134
7.1	Introduction	134
7.2	Experimental	137
7.3	Results and Discussions	139
7.3.1	Fabrication of the Nanostructured Feedstock	139

7.3.2	Thermodynamic Calculations for Oxidation Behaviors	140
7.3.3	Oxidation of the Nanostructured Feedstock	142
7.3.4	Coating Microstructures Obtained by SPS	147
7.3.5	Oxidation of the Al-Free Stainless Steel	148
7.3.6	Oxidation of Al-Containing Stainless Steel	153
7.4	Conclusions	157
GENERAL DISCUSSIONS		159
8.1	Introduction	159
8.2	Mechanical Milling and Alloying using cryomilling versus other Ball Milling	159
8.3	Comparison between SPS and other Processes	162
8.3.1	Microstructure Evolution during Processes Application	162
8.3.2	Oxidation Behaviors	165
GENERAL SUMMARY		168
ANTICIPATED CONTRIBUTION TO ORIGINAL KNOWLEDGE		173
REFERENCES		175
APPENDIX A		183

1. INTRODUCTION

Furnaces and boilers are vital equipment in the oil and gas industry due to the process dependence on their reliability. The corrosion of tube bundles disrupts operations of fired heaters and boilers and causes frequent down times. Oxidation is the most important high temperature corrosion reaction occurring in furnaces and boilers. The oxides of iron, nickel, and cobalt, which are the basis for the majority of modern alloys, are significantly less oxidation resistant than the oxides of some of the solutes such as Al, Cr and Mg. Traditionally, stainless steel and ferritic steels containing Cr (5%Cr-0.5Mo, 7%Cr-0.5Mo and 9Cr-1Mo) are used for the construction of the tube bundles in boilers and furnaces due to considerably lower cost and higher thermal conductivity [1,2]. The effect of the observed corrosion rates on the service life has been estimated for 9% Cr steel [3]. Moreover, the service oxidation occurring for components possessing a wall thickness lower than 6 mm cannot be neglected when made out of 9% Cr steel. Therefore, despite the inherently higher rupture strength of the 9% Cr steel, thin-walled components may not offer advantages over the higher Cr steels in terms of service duration [3].

Figure 1.1 present high temperature corrosion failure of a tube in one of Saudi Aramco gas plant. The cost of corrosion in Saudi Aramco operations is a significant problem that require implementation of new corrosion protection technologies. In Aramco plants, 60% to 70% of a plant maintenance budget is dedicated to corrosion control and corresponds to 25% of the overall operation budget. For plants with limited corrosion problem, 15% to

25% of the maintenance budget is dedicated to corrosion which corresponds to approximately 5% to 10% of the operating budget [4]. In a global picture, 47% of corrosion control expenses for Aramco are assigned to coatings technologies. Despite this effort, corrosion problems are still occurring, justifying the need for further research for coatings with enhanced protection.



Figure 1.1 Tube failure in one of Aramco oil and gas operations due to high temperature corrosion.

Special attention has been paid on nanocrystalline metallic coatings for high temperature corrosion resistance applications. Recently, nanocrystalline coatings were found to possess improved high temperature oxidation and corrosion resistance when compared to

their conventional counterparts [5]. Nanostructures promote selective oxidation, resulting in the formation of protective scales possessing superior adhesion to the substrate [5].

The objectives of this research project are to engineer Al-containing nanostructured austenitic stainless steel coatings to improve the corrosion resistance for high temperature applications found in oil the industry. The aim of engineering nanostructured Al-containing SS coatings is to promote the formation of a highly protective aluminum oxide scale while trying to maintain similar thermal conductivity and coefficient of thermal expansion (CTE) to the substrate. Mechanical alloying and mechanical milling of the austenitic stainless steel was done via cryomilling. Works on cryomilling of nickel and cobalt base alloys aiming at the fabrication of high temperature coatings were previously reported [6, 7], but no work was reported on the fabrication or usage of Al-containing nanostructured austenitic stainless steel system. The simulated coating samples were obtained by Spark Plasma Sintering (SPS) of the nanostructured powders on stainless steel substrates. In addition to the oxidation performance, the effect of cryomilling, heat treatment and SPS processes on the stability and transformation of the microstructure of the austenitic stainless steel and Al-containing stainless steel was investigated in this research project.

Chapter 2 contains a literature review covering the basis of oxidation, including the kinetic and thermodynamic arguments governing the high temperature corrosion performance of basic alloys used in oil industry. Results on the oxidation resistance performance, grain growth and phase transformation of nanostructured materials

containing Al performed by several researchers are also briefly discussed. The experimental methodology used in this work is the subject of Chapter 3. The results of mechanical alloying, phase transformation and grain growth stability of stainless steel containing various concentrations of Al will be discussed in Chapter 4. Chapter 5 discusses the nanostructure powder consolidation using Spark SPS. Specifically, an emphasis was placed on the microstructure evolution, phase transformation and mechanical properties of the stainless steel and Al-containing stainless steel. Chapter 6 presents the results and the discussion part of the oxidation kinetics of the cryomilled powders while Chapter 7 presents the effect of the addition of various Al concentration in stainless steel on the microstructure evolution of the SPS coatings during oxidation. Chapter 8 contains a general discussion comparing the performance of the alloys produced during this work with potential alternative processes like planetary ball milling and hot press consolidation. Summary and conclusions of this work are given in Chapters 9 while the contribution to the original knowledge is presented in Chapter 10.

2 LITERATURE REVIEW

The objective of this chapter is to review and study the fundamental underlying the synthesis of nanostructured stainless steel and Al-containing stainless steel powders using cryomilling, the strain induced phase transformation and its reversion occurring during milling and heat treatment, and its behavior during the consolidation using SPS and its oxidation resistance as a coating. In addition, this Chapter presents the fundamental of high temperature oxidation and particularities of oxidation of stainless steel. In addition the principle behind the formation of the natural aluminum oxide for Al-containing alloys and the obstacles preventing the formation of the Al_2O_3 layer will be discussed.

2.1 Synthesis of Nanostructured Powders Using Cryomilling

Synthesis of nanostructured powders can be achieved using cryomilling. Cryomilling is a mechanical attrition technique in which powders are milled in a slurry formed with milling balls and a cryogenic liquid.

2.1.1 Nanostructure Evolution Mechanism of Cryomilled Powders

During cryomilling, powder particles are subjected to severe mechanical deformation. The mechanism of nanostructure development during milling was suggested by Fecht [8]. The grain refinement mechanism is a three stages process, starting by local deformation, which result in high dislocation density, followed by annihilation and recombination of the dislocations to form nano-scale sub-grains. The final stage is the transformation of the sub-grain boundaries structure to the orientated high-angle grain boundaries structure. Xun et al. [9] illustrated the mechanism of formation of nanostructured grains through milling, as presented in Figure 2.1.

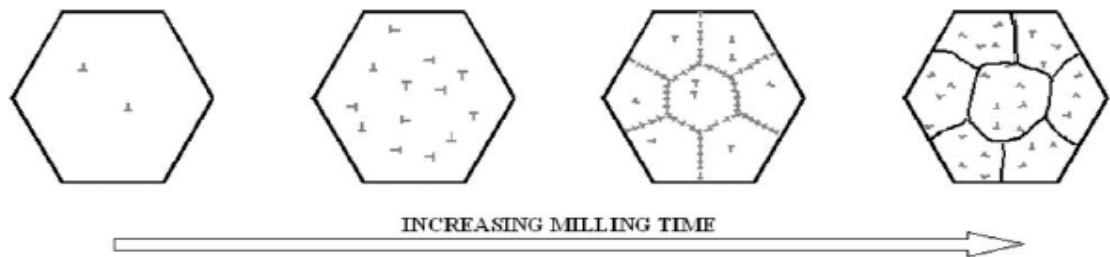


Figure 2.1 Schematic representation mechanism of nanostructured refinement during milling [9].

2.1.2 Mechanism of Mechanical Alloying Using Cryomilling

Mechanical alloying of powders to produce alloys of new compositions with controlled microstructure is the repeated process of fracturing, welding and rewelding of two or multiple powder particles [10]. The two processes, cold welding and fracturing are taken place for particles that are under a continuous sequence of collisions. These repeated impact events enable the particles to be in contact with other particles creating new atomically clean surfaces, which minimize the diffusion distances for elements to create the desired composition [10, 11]. Cold welding is important to make interdiffusion bonds between particles, however excess cold welding would lead to particles agglomeration, which would prevent element diffusion and alloying. Cold welding and fracturing should be balanced to have successful mechanical alloying. For many mechanical alloying systems, this critical balance does not occur naturally [10, 11]. Two methods have been used to control balance between cold welding and fracturing during milling. The first approach is adding processing control agent (PCA) to modify the surface of the deforming particles that provides the clean contact surfaces necessary for cold welding. Processing aluminum-alumina alloys requires the addition of a PCA compound to reduce excessive cold welding of the Al powder. This is obtained by modifying the particles and increasing the exposed clean particle surfaces necessary to metal-to-metal contact. The second technique is by modifying deformation during milling which allow particles to fracture before they are able to weld and agglomerate under large compressive strains. This can be accomplished by cryogenic milling. For example, lead is very difficult to mechanically alloy because it is an extremely soft and ductile material at room

temperature [10]. Cryomilling embrittles the metal and promotes fracturing, establishing the balance of between two processes.

2.1.3 Alloying and Formation of Nanostructured Iron-based and Al-Containing Powders Using Cryomilling

A number of studies were found in the literature on milling stainless steel using Spex and planetary ball milling. However, limited work was done on milling stainless steel within a cryogenic medium. Maggy and Lavernia [12] investigated the microstructure and morphology of cryomilled HVOF 316SS coatings. Pre-alloyed 316 stainless steel powders with a nominal particle size ranging between 11-45 μm were mechanically milled in liquid nitrogen for 10 hr to produce powders with a nanocrystalline grain size of 21 ± 8 nm. No results regarding the milling operation were presented, and their results showed a higher level of porosity for the coatings made with the cryomilled powders when compared with the coatings fabricated using the conventional powders. Also, a higher level of second-phase particles present in the coating made with the cryomilled powders was observed when compared with the conventional coatings. This observation suggests an increased chemical activity of the nanocrystalline particles during thermal spraying or/and solidification. The oxygen content of the cryomilled coatings was higher than that of the conventional coatings despite that both coatings were produced using identical spraying parameters. The increase in oxygen content in the nanostructured

coatings is most likely originating from the increased level of oxygen in the cryomilled powders.

High-energy cryomilling has evolved into a reliable route by which metallic Al-containing alloys with grain size of the order of the nanometer scale may be synthesized from their elemental constituents and few examples are found in the literature. Fe powder was blended with 10 wt% Al followed by cryomilling for 25 hr [13]. The experimental results indicated that cryogenic milling of Fe-10wt.% Al was effective to alloy the blend and to create a nanocrystalline structure. The average grain size obtained from image analysis of TEM micrographs was 11 nm. The average powder particle size ranged between 4 and 16 μm . This particle size is notably smaller than what is obtainable through dry attritor milling for 24 hr [13]. Chemical analysis of different regions of the Fe-10Al cryomilled powders using energy dispersive spectroscopy (EDS) coupled to TEM indicated partitioning of the Al content according to the grain structure, where 18.8 wt.% Al was found in the finest grain regions, 16.6% of the Al was found in the elongated regions, 2.7% in the 100nm equiaxed grains, and 0% in the larger grains [13]. High speed steel M50 (4.5%Mo, 4.0%Cr, 1.0%V, 0.8%C, balance Fe) was mechanically alloyed with 5 wt% Al using cryomilling for 25 hr of milling time using a powder-to-ball weight ratio of 1:20 [14]. X-ray diffraction analysis performed on the milled M50-5% Al powder yielded an average calculated grain size of 15 nm while the TEM dark field micrographs indicated an average grain size of 10 nm. The X-ray diffraction of the cryomilled powders indicated completed alloying after 25 hr of milling by the disappearance of the Al characteristic peaks. Selected area diffractions (SAD) from the TEM micrographs showed

a ring pattern that corresponded to BCC Fe phase. Other phases were not observed in the SAD due to their small volume fraction, as reported by Lau, et al [14].

Cryomilling of pre-alloyed nickel base powders containing Al utilized in thermal spray application was investigated in several studies. Cryomilling of as-received spherical NiCrAlY (Ni-22wt%Cr-10%Al-1%Y) powders leads to the formation of irregular and flake-shaped agglomerates. Furthermore, one could observed an increase in the agglomerate size with milling time. The grain size refinement achieved by the cryomilling process was used to produce nanocrystalline NiCrAlY powders, with a grain size in the nanometric rang, i.e. lower than 50 nm [6]. A commercially available NiCrAlY powder was mechanically cryomilled for HVOF spray and formed bond coat for high temperature application [15]. Mechanical cryomilling of the as-received spherical NiCrAlY powders led to the formation of irregular and flake-shaped morphology, which is attributed to the continuous balance of welding and fracturing processes occurring during the mechanical milling process. TEM micrographs showed an average grain of 26 ± 8 nm. XRD analysis was performed on the as-received and on the cryomilled powders, the Ni, Cr-rich (γ phase) and Ni_3Al (γ' phase) peaks and some traces of AlNi phase ($\text{Al}_{0.42}\text{Ni}_{0.58}$) are observed after 12 hr of milling. The broadening of Ni, Cr-rich (γ phase) and Ni_3Al (γ' phase) peaks was observed after cryomilling. The physical origin of the XRD peak broadening is well known and is due to the small grain size structure of the powder and microstrain introduced into the material during processing [15].

2.1.4 High Temperature Stability of Cryomilled Al-Containing Powders

Improvement of the thermal stability of milled powders against grain growth is of paramount importance in the development of an economical methodology for the production of nanocrystalline powders. Cryomilled Fe and mechanically milled Fe exhibit similar grain growth behavior when exposed to high temperature [16]. The addition of Al as an alloying element to Fe stabilizes the grain size. Heat treatment of cryomilled Fe-10wt% Al for one hour at temperatures of 1073 K and 1223 K revealed that the fine grain sizes are maintained [17]. This level of thermal stability is shown to exceed that of pure Fe processed under identical conditions by a significant margin, as shown by Figure 2.2 [13]. Oxygen and nitrogen uptake during cryomilling greatly influenced the development of new particles formed during the synthesis of Al-containing stainless steel. Cryomilling of Al and its alloys in liquid nitrogen has been reported to result in the in-situ formation of oxy- nitride or AlN particles which impeded grain growth at high temperature [13, 17].

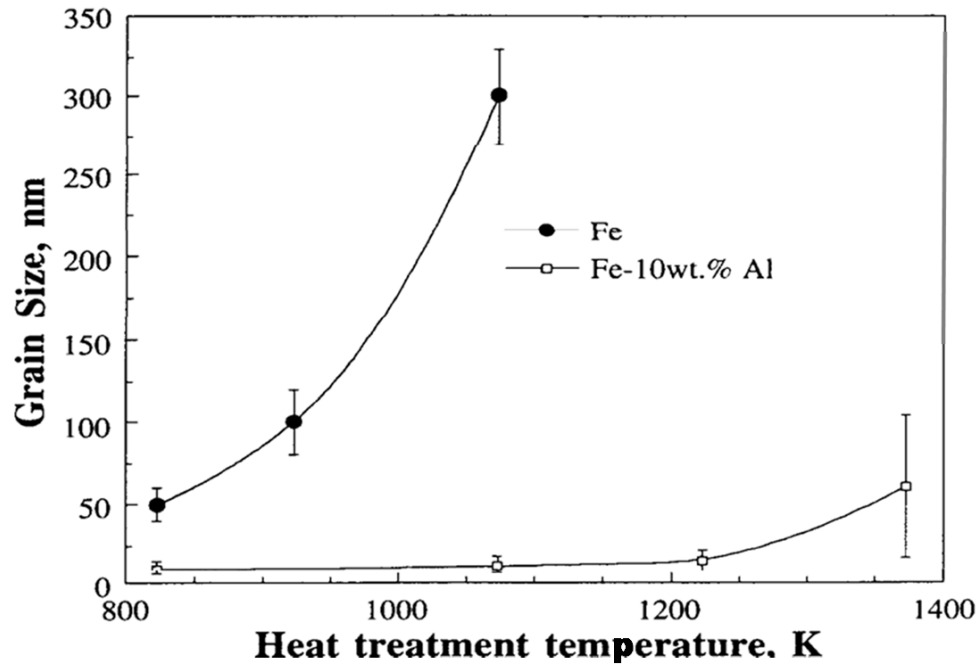


Figure 2.2 Grain size versus heat treatment temperature for 1 hr [13].

2.2 Deformation and Phase Transformation of Stainless Steel during Mechanical alloying and Heat Treatment

The study and improvement of stainless steel alloys is important because of the wide applications these materials are found in, in the modern society. Recent years have seen a marked increase in worldwide production and consumption of stainless steel [18]. Stainless steels, a family of iron alloys containing a minimum of 12 wt.% Cr, have been developed to withstand corrosion, wear and high temperature degradation in aggressive

environments [19]. In particular, austenitic stainless steels, which exhibit a face centered cubic (austenite) crystal structure at all temperatures, are widely used for high temperature corrosion applications. The microstructure of austenitic stainless steel deforms and can even exhibit a change in crystal structure when exposed to sufficient mechanical work.

2.2.1 Deformation Mechanisms and Stability of Austenite Stainless Steels

The deformation structures and dislocation evolution of austenitic stainless steel depend critically on the stacking fault energy (SFE) [20]. Chemical composition and temperature are known to be the primary factors controlling SFE and, consequently, determining the deformation mechanism for a given alloy [21, 22]. SFE of the order 25-60 mJ/m² favours mechanical twinning [23, 24]. Phase transformation due to glide of dislocations is the dominant deformation mechanism of alloys with SFE values greater than 60 mJ/m² [25]. In addition, the stability and recovery of the austenitic phase is important for alloys possessing high SFE [26, 27]. Several empirical relations were suggested in the literature to calculate the SFE of austenite steels. Among them is the equation proposed by Rhodes et al. [28]:

$$\text{SFE} = 1.2 + 1.4 (\text{Ni}) + 0.6 (\text{Cr}) + 7.7 (\text{Mn}) - 44.7 (\text{Si}) \quad (1)$$

where the SFE is in (mJ/m²) and the respective elements are in mass percent.

2.2.2 Phase Transformation of Austenite Stainless Steels during Mechanical Alloying and Milling

During mechanical alloying, the austenitic stainless steel is exposed to severe plastic deformation that results in an induced phase transformation. In the literature, there are contradictory works on mechanical milling of austenitic stainless steel, highlighting a discrepancy in the crystal structure obtained after deformation. SS316L was subjected to high strain powder metallurgy (HS-PM) process, which combined mechanical milling and mechanical alloying, followed by heat treatments [29]. The austenitic stainless steel powders showed a strain induced ferrite transformation from face centered cubic (FCC) to body body centered cubic (BCC) during mechanical milling using a planetary ball mill. Ultra fine grains consisting of BCC phase of approximately 15 nm in diameter are observed and have high angle boundaries, as shown by TEM diffraction pattern [29].

On the other hand, several studies showed that the transformation of austenitic stainless steel during mechanical milling yields a martensitic induced phase transformation. A. Szymanska showed in his mechanical milling work of commercial SS316L powders using the Mossbauer technique that the strain induced transformation produces a martensitic crystal structure [30]. It was also reported that the composition of the austenitic stainless steel and temperature at which the stainless steel is deformed influence the amount of austenite to martensite transformation. The phase transformation during mechanical milling of austenitic stainless steel (Fe-20Cr-7.03Ni-1.62Mn-0.4S-0.05C

wt.%) was investigated by Enayati et al. for long milling time [31]. They reported that a nanosized martensite phase develops during the milling process. Moreover, the austenite did not completely transformed into the martensite structure, even after 100 hr of ball milling. In another work, Enayati and Bafandeh [32] used three austenitic stainless steel alloys, namely Fe–18Cr–8Ni, Fe–15Cr–15Ni and Fe–15Cr–25Ni (wt.%), to study the effect of the chemical composition on the phase transformation during mechanical alloying in a planetary ball mill and after subsequent annealing [32]. Two different elements with different weight percentage namely nickel, known as an austenite stabilizing element, and Cr, known as a ferrite stabilizing element, were involved and the respective ratio was changed in the three alloys. Fe–18Cr–8Ni and Fe–15Cr–15Ni alloys showed a single martensite structure after 60 hr and 50 hr of milling, respectively. However, the mechanical alloying behavior of the Fe–15Cr–25Ni composition was found to be quite different. Milling for 10 hr yielded a two-phase structure, an austenitic solid solution co-existing with a martensitic solid solution. The maintain of the austenite phase is associated to the higher content of austenite stabilizing element, Ni. At a certain stage of milling, the fraction of austenitic grains increased until the structure re-became completely austenitic after 50 hr of milling time. In another work, Oleszak et al. [33] studied ball milling of 316L stainless steel powders in a planetary mill, which resulted in the two-phase structure consisting of austenite and martensite [33]. The maximum content of martensite (66%) was observed after relatively short milling times (2 hr). For longer milling times, the martensite fraction was found lower, reaching 46% after 100 h of milling. Huang also studied the mechanical milling of 304 steels, which also resulted in the formation of a strain induced martensite structure [34]. Similarly, longer milling time,

i.e. more than 400 minutes, resulted in a reduction in the magnetization, which was associated to a lowering of the martensite fraction due to the reversion to the austenite phase. Other studies suggested that temperatures as high as 500 °C can be locally reached during milling collisions, reinforcing the possibility of inducing crystal structure reversion during milling, which is amplified during longer milling periods [35, 36].

2.2.3 Phase Transformation of Austenite Stainless Steels during Heat Treatment

It is important to study the annealing behavior of the nanostructured stainless steel during heating as consolidation requires a heating stage. Most research works mainly focus on the thermal stability of the nanograin structure. Oleszak et al. determined from Mössbauer spectroscopy measurements, that the fraction of martensite in the 316L austenitic stainless steel sample after 100 h of milling followed by heating in a DSC up to 720 °C decreases down to 8%, compared to the initial 46% after ball milling [33]. H. Huang showed in his work that a total reversion of the martensite phase to the austenite structure was achieved at 800 °C for a nanostructured 304 stainless steel powder prepared using a Spex mill [34]. Chen et al. studied the phase transformation of the nanostructured surface layer of 304 stainless steel prepared by surface mechanical attrition [37]. The reported XRD showed that the nanostructured surface is composed of a mixture of austenite (14%) and martensite (86%). The content of austenite increased from 14% to 20% during annealing at 500 °C. Enayati et al. performed isothermal annealing of

austenitic stainless steel (Fe–20Cr–7.03Ni–1.62Mn–0.4S–0.05C wt.%) at 700 °C and their results showed partial reversion of the martensite to the austenite structure [31]. The annealed powders still had a strong ferromagnetic behavior after annealing, suggesting that there is still a significant fraction of martensite remaining from the incomplete martensite-to-austenite reversion for the study heat treatment parameters.

2.3 Spark Plasma Sintering

The process parameters for bulk consolidation and coating deposition of nanocrystalline powders should be carefully selected to maintain the extraordinary properties gained from grain refinement. SPS, also called pulsed electric current sintering (PECS), is a relatively new technology, which makes possible to consolidate various kind of powder materials at lower temperatures and in a shorter cycle time than most sintering and hot pressing processes [38-42]. SPS belongs to the pressure-assisted sintering (PAS) technology, where pressure and temperature are applied simultaneously. SPS is receiving significant attention by researchers as it is one of the most advanced materials processing route available these days. Indeed, the number of publications on SPS has increased significantly during the last decade, as seen from Figure 2.3. The increasing number of publications depicts the numerous attempts to consolidate various powder material systems using this new technology [43].

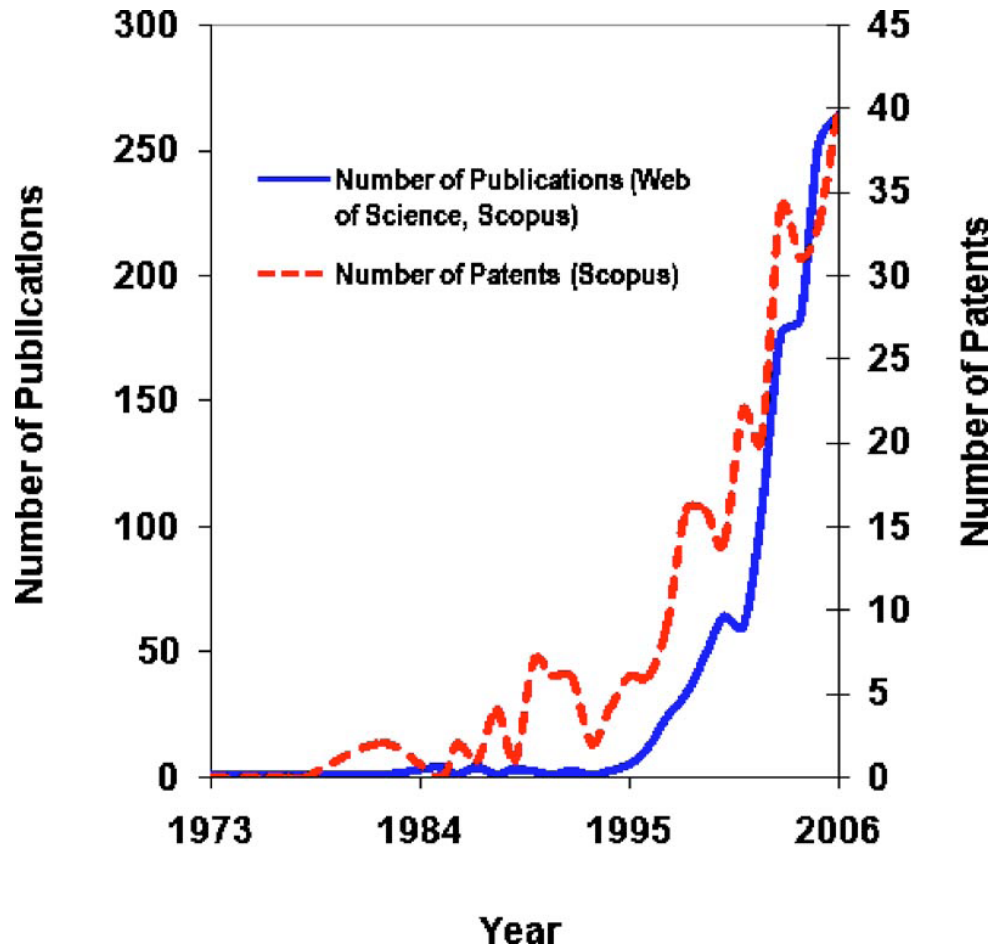


Figure 2.3 Statistic of publications on SPS [43].

2.3.1 Mechanism of Spark Plasma Sintering

The reported phenomena behind the SPS process is a pressure sintering method based on high temperature plasma (spark plasma) generated from an intense electric discharge that can reach 20,000 A in a few milliseconds. The spark plasma generated by the electric

discharge within the gaps between the particles densifies the porous bed in a very short processing time compared with other techniques [39].

According to Tokita [39], SPS occurs through the electrical discharges that would first generate a plasma at the contact points between the particles, resulting in a localized temperature of several to ten thousand degrees, which is amplified by the impact pressure due to the sparks and heating through the Joule effect. This causes evaporation and melting on the surface of the powder particles as well as the formation of necks around the area of contact between the particles, as illustrated in Figure 2.4. These necks gradually progress closing down the porosity during the heat cycle, resulting in sintered compacts reaching a density of over 99%.

In a recent study, neck morphologies at the inter-particle were observed during SPS [44]. The behavior of spherical copper powder with narrow size distribution was directly observed in the compact using an optical microscope (OM) during the course of electric discharges at various current densities (I_p) and pressures (P). Figure 2.5 (a), (b) and (c) shows the neck morphologies created between the copper particles at (a) $I_p = 117 \text{ A mm}^{-2}$, $P = 6.9 \text{ MPa}$, (b) $I_p = 33.3 \text{ A mm}^{-2}$, $P = 10.1 \text{ MPa}$ and (c) $I_p = 116.7 \text{ A mm}^{-2}$, $P = 15.7 \text{ MPa}$, respectively. Figure 2.5 (a) shows the neck formed at the portion where the electrical arc was observed with the OM. The neck was clearly created by melting at the inter-particle contacts. Figure 2.5 (b) and (c) are the micrographs depicting the developed necks when the spark phenomenon was not observed. In this study, the relation between the average neck diameter and current density was measured. Regardless of whether or

not the spark was observed, the neck diameter was found to increase with increasing current density [44].

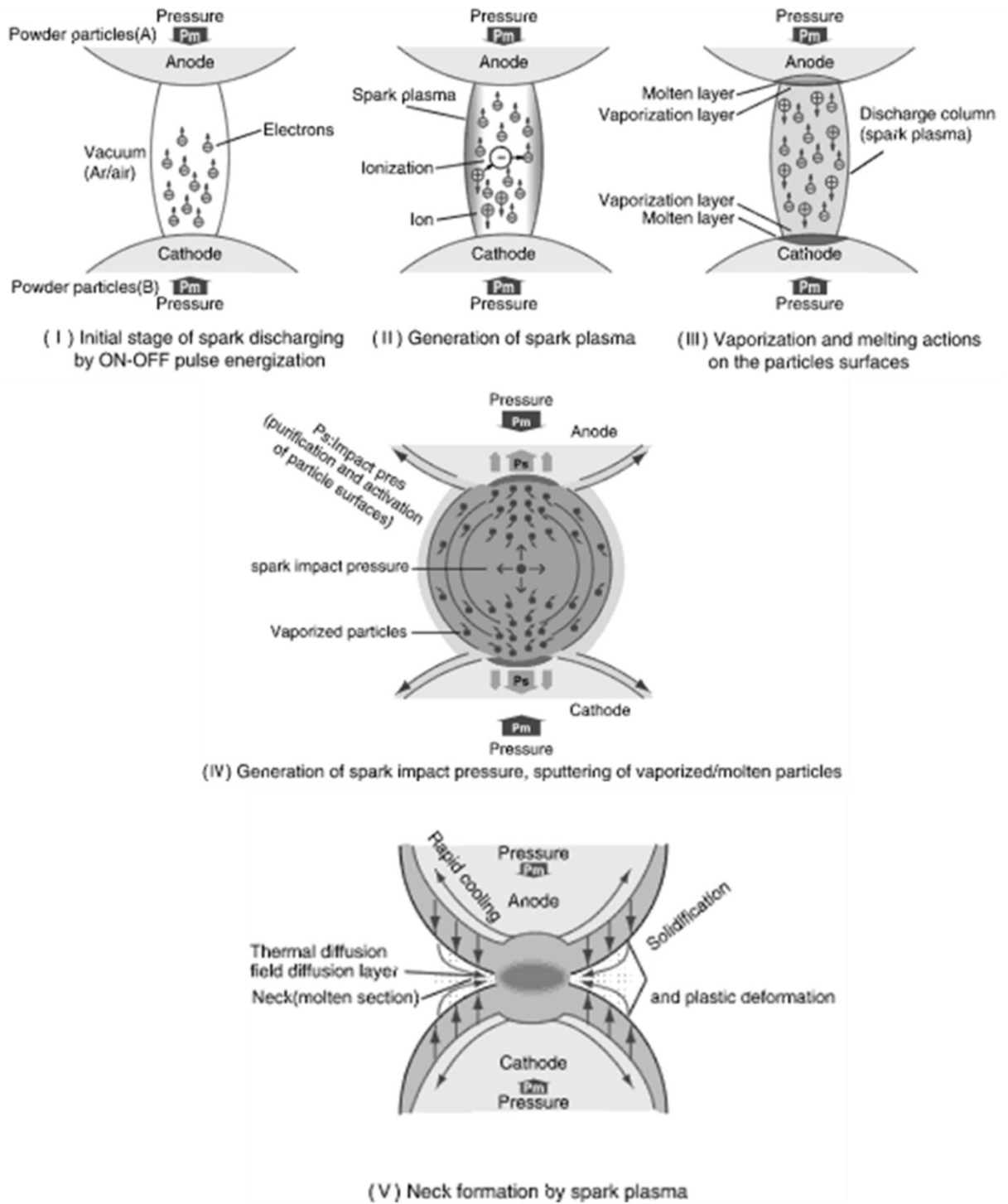


Figure 2.4 Mechanism occurring between particles in contact during an electric pulse generated by the SPS process [39].

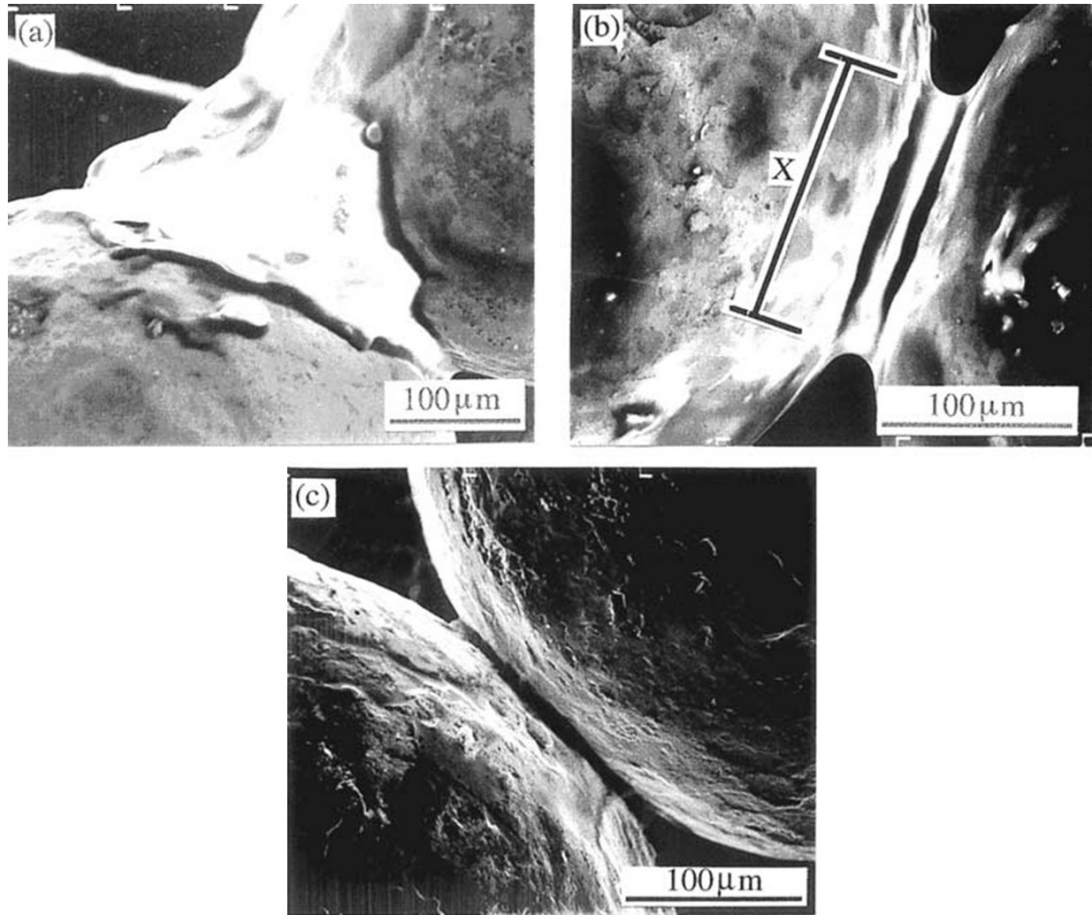


Figure 2.5 The morphologies of neck formation at the inter-particle during SPS (a) electrical arc was observed, (b) and (c) the spark phenomenon was not observed [44].

2.3.2 Advantage of Spark Plasma Sintering

The main advantages of SPS compared to other sintering methods such as hot pressing are the low operating cost, the local high-temperature region at the contact points, the rapid heating, and the shorter sintering time. Moreover, it is also possible to consolidate and assemble different types of materials such as composites and nanomaterials, even to

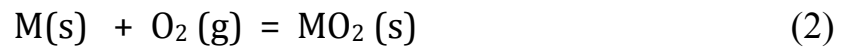
those materials that are very difficult to be sintered by other conventional processes [45-47]. This sintering method is considered to be very fast due to the electric current that flows directly throughout the sintered material, and a very high efficiency of self heating inside the powder. Hence, the main difference compared with conventional sintering techniques is that the sample is heated from the inside rather than from the outside. As a consequence, the significantly reduced sintering time means that dense bulk materials can be produced and that coarsening due to grain growth remains almost totally inhibited [45-47].

Nanocrystalline 430L stainless steel was consolidated using SPS [41]. The results indicated that the nanostructured 430L stainless steel was sintered to nearly full density within shorter time when a sintering temperature over 900 °C was used. The SPS samples exhibited enhanced mechanical properties than the conventional 430L stainless steel. The optimum Vickers hardness and tensile strength obtained were 501 HV and 713 MPa, respectively.

2.4 Oxidation

Oxidation is corrosion which forms oxide corrosion products, reducing the useful thickness of the metal component, and often occurs upon exposure of metals to temperatures above 400°C in gases containing more than 1% (vol) O₂ [48, 49]. An

oxidation reaction between a metal (M) and the oxygen gas (O₂) to form metal oxide MO₂, can be written as:



Although equation (2) chemically appears very simple, there are varieties of factors on which the oxidation behavior of a metal depends and the reaction mechanism involved may often be quite complex.

An oxidation reaction begins with adsorption of oxygen molecules from the gaseous atmosphere, which then nucleate the oxide product, extending to the formation of a thin and continuous oxide layer, followed by its growth to a thicker scale [48-50].

The first two steps are affected by many factors such as surface orientation, crystal defects at the surface, surface penetration and impurities in both the metal and the gas [49]. The oxide film acts as a protective barrier when the film cover the whole surface of the metal, and the only way for the reaction to proceed is through the diffusion of the reactive through this oxide film.

2.5 Thermodynamic Consideration at High Temperature

The most important aspect for the oxide formation and the type of scale developing is the thermodynamic stability of the oxide. Formation of oxide scale according to equation (1), needs a driving force which depends on the Gibbs free energy of formation of the oxide, ΔG . The Gibbs free energy is a function of the dissociation pressure of the oxide, also known as equilibrium oxygen pressure. Thermodynamically, the oxide scale will form at the surface of the metal when the oxygen activity in the environment surrounding the metal is greater than the oxygen partial pressure in equilibrium with the metal [48]. The driving force, ΔG , for the oxidation reaction can be written as:

$$\Delta G = \Delta G^\circ + RT \ln \frac{a_{MO_2}}{a_M \cdot P_{(O_2)}} \quad (3)$$

Where ΔG° is the standard free energy change of the reaction, a_{MO_2} , a_M are the activities of the formed oxide and the metal, $P_{(O_2)}$ is the partial pressure of the oxygen gas, R is the gas constant and T is the temperature. Reaction (2) is under the following conditions:

$\Delta G < 0$	Reaction expected
$\Delta G = 0$	System at equilibrium
$\Delta G > 0$	Thermodynamically impossible reaction

For a system that is at equilibrium, the standard free energy of reaction (2) becomes:

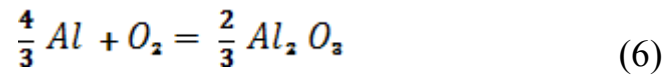
$$\Delta G^\circ = -RT \ln \frac{a_{MO_2}}{a_M \cdot P_{(O_2)}} \quad (4)$$

Generally, the activity of the solids in reaction (2) is assumed to be equal to 1 as they are pure compounds. Therefore, equation (4) can be written as:

$$P_{O_2} = \frac{\exp(\Delta G^\circ)}{RT} \quad (5)$$

The partial pressure of oxygen in equilibrium with the oxide product can be determined from the standard free energy of formation using equation 5. For many oxidation reactions, the standard free energy of formation of oxides as a function of temperature is plotted on Ellingham/Richard diagrams, as presented in Figure 2.6. This diagram is used to know if any metal can form an oxide scale at the oxygen partial pressure and the temperature of the exposed environment. The Ellingham/Richard diagrams are plotted from experimentally found ΔG° and T for oxidation.

The standard free energies are based on the formation of oxide per 1 mole of oxygen, such as the following reaction:



The most stable oxide in the Ellingham/Richard diagram has the largest negative value of the standard free energy of oxide formation and is represented by the lowest line in the diagram [48]. This diagram is very important for the engineering of alloys exposed to high temperature oxidation, where a less stable oxide developing on the base alloy can be replaced through the alloying with elements possessing a more stable oxide. For example, it is clear from Figure 2.6 that oxides of iron, nickel and cobalt which are the main compounds of the engineering alloys, are significantly less stable than the oxides of some elements like Al, Cr or Si. When one of these elements is alloyed to iron, nickel or cobalt with the necessary concentration, the base alloy becomes protected due to formation of a better protective oxide surface [48].

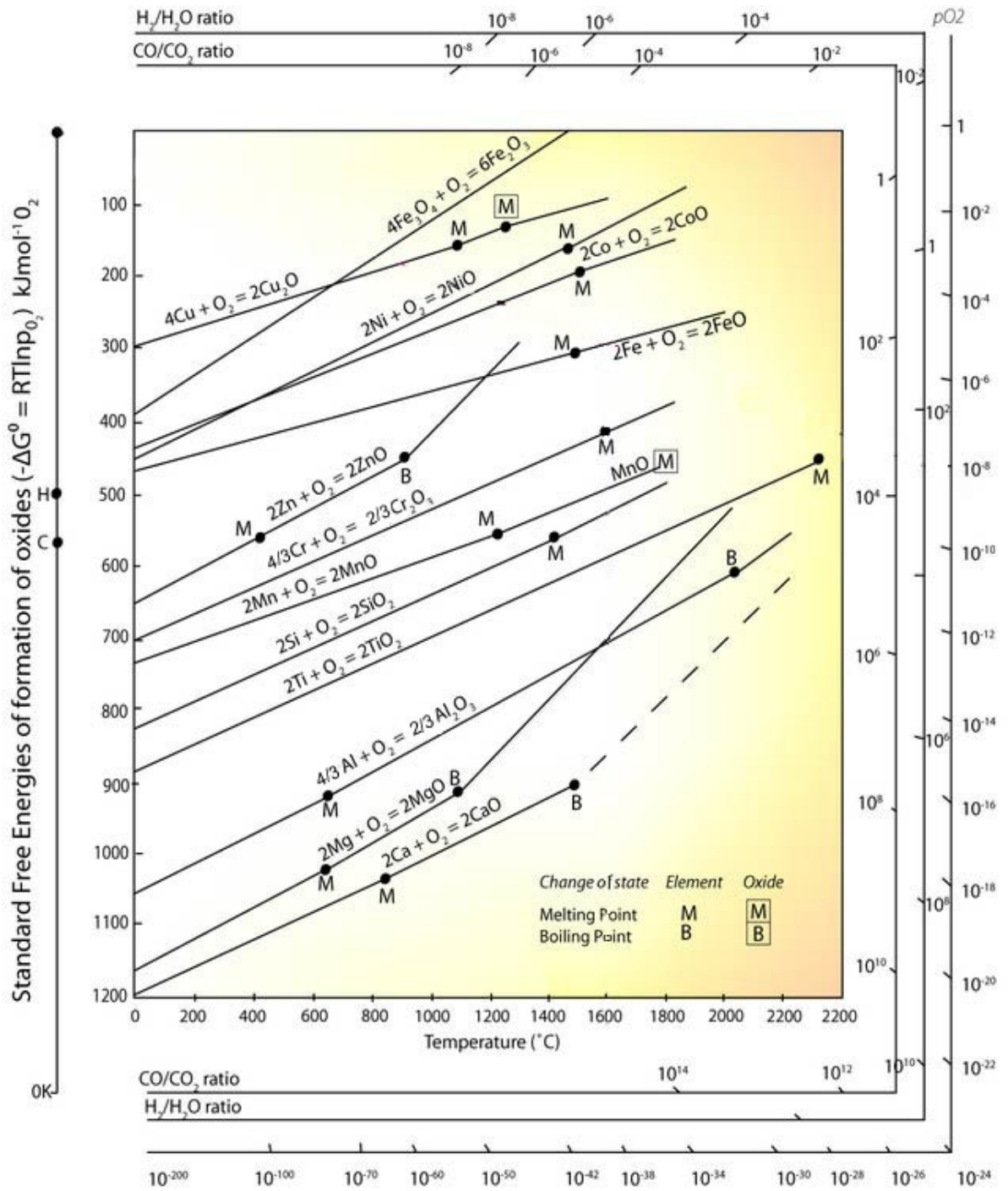


Figure 2.6 Ellingham/Richard diagrams [48].

The Ellingham/Richard diagram is very important to know the most stable oxide surfaces developing during oxidation and whether the oxide formation is possible under specific

environmental conditions, such as a particular temperature and partial pressure of oxygen. However, one of the limitations of the Ellingham/Richard diagram is that the diagram does not take into account the oxidation kinetic. There is no relation between thermodynamics of oxidation and the kinetic of oxidation, although the free energy change is the driving force for the oxidation reaction. In addition, Ellingham/Richard diagram do not indicate the minimum concentration of the solute element required to form the protective oxide surface. Therefore, the thermodynamic of high temperature metal oxide systems is not sufficient to interpret the oxidation reaction time and also give the information regarding if the solute element concentration is sufficient to form the protective oxide surface. In order to have a better understanding of the oxidation of metals, a combination of thermodynamics and kinetics of the oxidation reaction is key to interpret the mechanism of high temperature oxidation at specific conditions of gas environment and temperature.

2.6 Oxidation Kinetic

Figure 2.7 [51] shows the oxidation kinetic rate constants of several oxides from which it can be seen that the highest oxidation rates are obtained for the systems whose oxides have the lowest oxide stability in the Ellingham/Richard diagrams. Clearly, in the development of oxidation resistant alloys, it is important to engineer a composition that develops one of the most thermodynamically stable oxides (Figure 2.6), which also has one of the slow growing oxidation kinetic rate (Figure 2.7). Measurement of kinetic of

oxidation is very important to estimate the design life of alloys and to obtain valuable information about oxidation behavior prior to the characterization of the oxide surface.

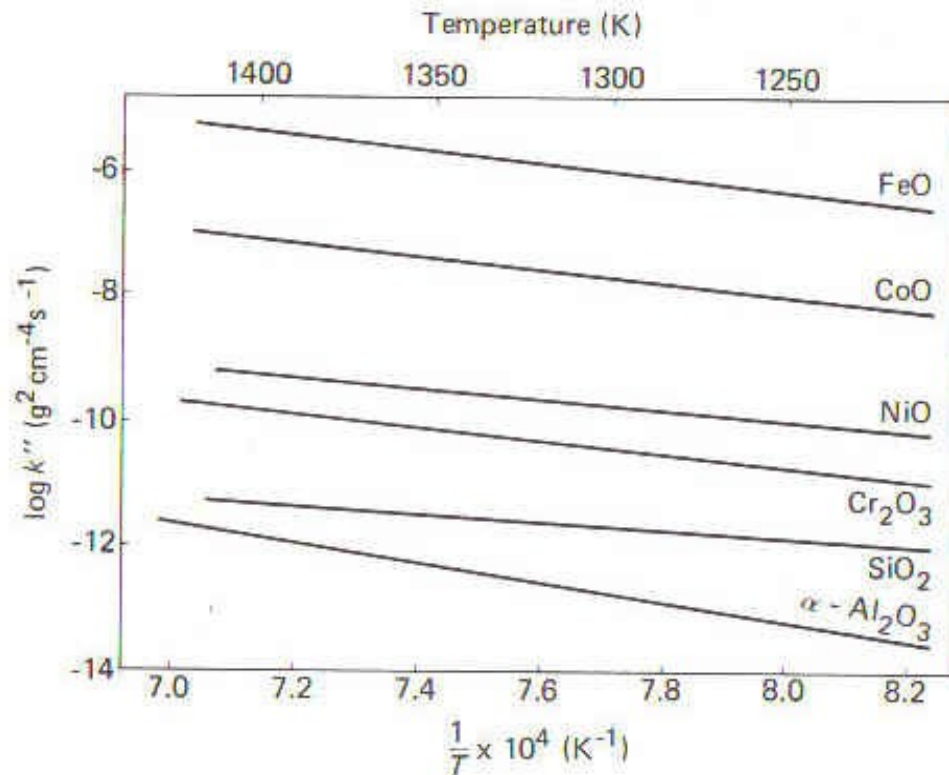


Figure 2.7 Oxidation kinetic rate constants for the growth of several oxides [51].

The rate of oxidation of a metal according to reaction (2) may be measured by the extent of reaction in the form of

- a. The amount of the metal consumed
- b. The amount of oxygen consumed
- c. The amount of the oxide formed

In practice, the amount of metal consumed may be measured by the mass loss of the sample or the residual metal thickness during or after oxidation. In both cases, the sample must be removed from the furnace which interrupts the oxidation process [50]. The amount of oxygen consumed can be measured by volumetric and manometric methods, and the use of solid state oxygen sensors to determine the equilibrium oxygen pressure for the metal oxide system. The amount of oxide formed can be measured by different methods. Among them is the thermogravimetric method, which is the most widely used method to gather kinetic data during high temperature exposure of metals and alloys to oxidative environments. This test method involves measuring the sample weight as a function of time. The test apparatus continuously monitors the sample weight during testing with a recording balance. The apparatus arrangement allows the inlet test gas to be preheated to the test temperature in a small tube prior to the reaction with the test sample in the reaction chamber. Preheating the inlet test gas is desirable as the test gas is often composed of a mixture of several gaseous components and as the preheating allows the gas mixture to reach thermodynamic equilibrium prior to reaching the reaction zone. The major advantage of the gravimetric apparatus possessing an automatic recording balance is the continuous gathering of data corresponding to the reaction kinetic. The disadvantage is that only one sample can be tested each time, so generating comparative data for a number of specimens is a lengthy process.

It was found experimentally that several reaction kinetic laws can be identified using the above mentioned technique [48]. There are many factors affecting the reaction rate and determining the rate equation law for a metal oxide system, such as the type of metal,

environmental gas pressure, temperature and the surface preparation and pretreatment of the metal. The principle oxidation rate laws are

- a. Linear reaction rate
- b. Parabolic reaction rate
- c. Logarithmic reaction rate

2.6.1 Linear Oxidation Rates

Linear reaction is a fast oxidation rate and it remains constant with time. Linear oxidation is independent on the amount of gas or metal previously consumed in the reaction, so usually the metal surface is not yet cover by a continuous and protective scale for this regime of oxidation. Oxidation following the linear law is usually found to follow cracks in the oxidation scale or spalls, leading to direct contact of the environmental gas with the bare metal [48,49]. A representative oxidation behavior curve following the linear oxidation law is shown in Figure 2.8 and the weight gain or thickening is directly proportional to the time according to equation (7):

$$X = kt \tag{7}$$

where X is the scale thickness (or weight gain) and k is the linear constant rate of oxidation. The appropriate linear rate constant would have the units of mass gain per surface area and time.

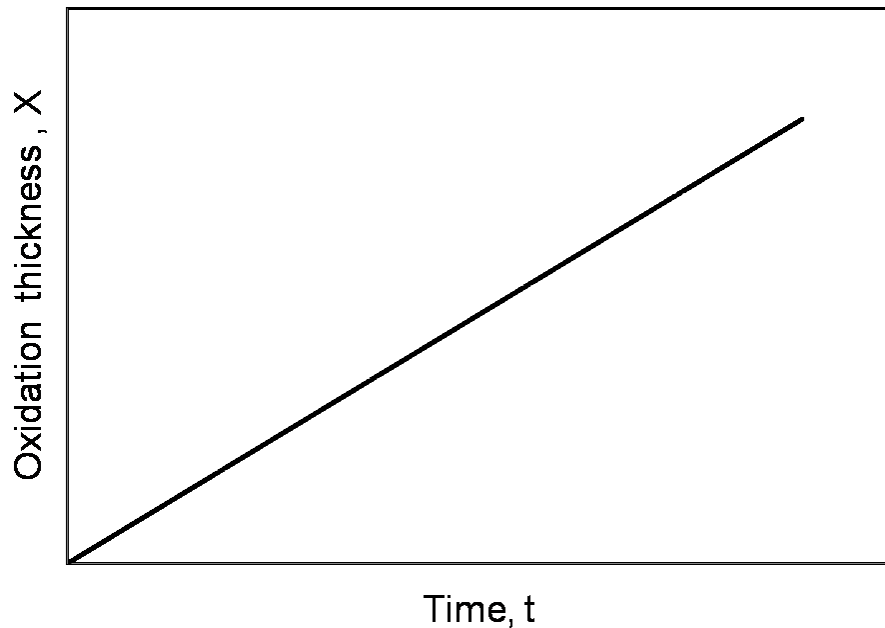


Figure 2.8 A representative oxidation kinetic following the linear behavior.

2.6.2 Parabolic Oxidation Reaction Rates

The parabolic oxidation reaction rate is very important as most metals and engineering alloys follow parabolic kinetics at high temperature and the behavior is depicted in Figure 2.9. The oxide growth process is usually governed by the diffusion of one or more reactants or electrons through the initially formed oxide scale. In parabolic reaction, the oxide scale growth occurs with a continuing reduction in the oxidation rate. Therefore the

rate of the reaction is inversely proportional to thickness of the oxide scale [48]. This reaction rate is expressed by the following equations:

$$\frac{dX}{dt} = \frac{K_p}{X} \quad (8)$$

Integration and noting that $X = 0$ at $t = 0$

$$X^2 = 2K_p t \quad (9)$$

where X is the weight gain and K_p is the parabolic rate constant, which is a function of the diffusion coefficient of the reactant.

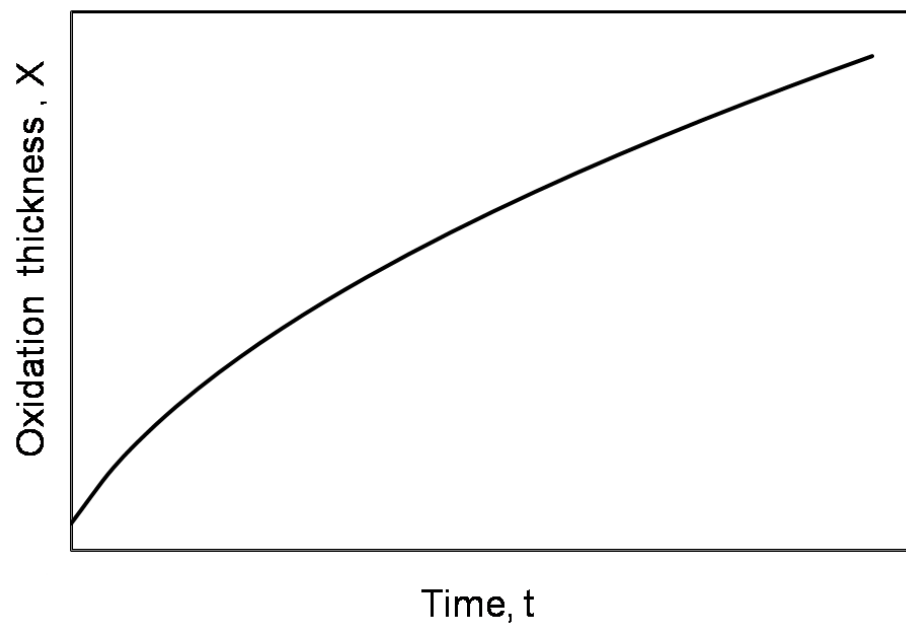


Figure 2.9 A representative oxidation kinetic following the parabolic behavior.

2.6.3 Logarithmic Reaction Rates

The oxidation follows either logarithmic or inverse logarithmic kinetic oxidation when a very thin oxide layer forms on the metal surface at temperatures below about 400 °C [48-51]. This type of oxidation rate is shown in Figure 2.10, which indicate rapid initial reaction rate and is slowing down with time. Equations (10) and (11) express this mechanism, where the

Direct logarithmic law is:

$$X = K \log t + A \quad (10)$$

and inverse logarithmic law is:

$$\frac{1}{X} = K' \log t + B \quad (11)$$

where X is either the weight change during oxidation, the thickness of the oxide formed, the amount of oxygen consumed per unit surface area of the metal or the amount of the metal transferred to oxide, t is the oxidation time, K, K' are the constant rates for the logarithmic and inverse logarithmic processes, A and B are constants.

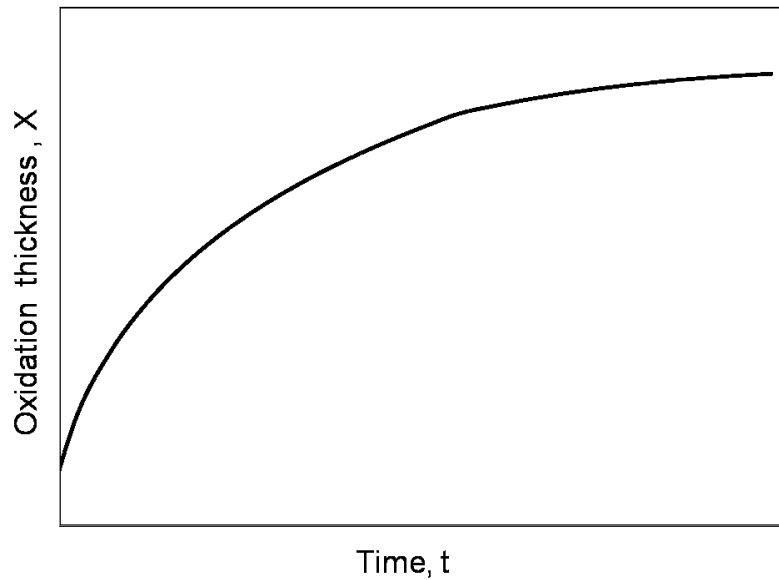


Figure 2.10 A representative oxidation kinetic following the logarithmic behavior.

2.6.4 Combination of Simple Rate Equations

When oxidation of metals or alloys is conducted experimentally, it has been observed that the oxidation behavior follows a combination of the above mentioned mechanisms [48,49]. Many metals at low temperature follow a combination of logarithmic and parabolic laws. A combination of parabolic and linear oxidation is often observed at elevated temperatures. One of the rates can be dominant for the initial oxidation stage but changes to another oxidation mechanism after some times. A combination of oxidation mechanism might be occurring as a result of the change in the nature of the oxide scale or when the oxide scale partially cracks at the scale/metal interface.

2.7 Oxidation of Austenitic Stainless Steel

Austenitic stainless steel was thermodynamically developed to promote the formation of chromium oxide (Cr_2O_3) at high temperature in the presence of oxygen, which is considered to act as a protective layer. Martensitic and ferritic stainless steel can form Cr_2O_3 scale at high temperature. However, austenitic stainless steel are more suitable for high temperature applications because of their inherent high strength and good ductility [48]. In general, austenitic stainless steel requires a minimum of ~18 wt.% Cr to form a protective chromia-based layer (Cr_2O_3 , Cr-rich mixed oxide) and are used in many high temperature applications up to 900 to 950 °C. Above this temperature, the chromia layer starts decomposing into volatile CrO_3 and the oxidation resistance of the austenitic stainless steel is no longer retained [48].

For the austenitic stainless steel compositions, the thermodynamic and kinetic parameters of the oxidative environment (oxidizing species, oxygen partial pressure, temperature and time), affect the uniformity of the Cr_2O_3 oxide surface scale developing and can either form two layers or a single mixed oxide. Several studies were performed to investigate the chemical composition of the thin oxide layer formed at the surface of stainless steel at different temperatures and oxygen partial pressures [52-58]. At a temperature above 400 °C and oxygen pressure lower than 10^{-3} Pa, a uniform Cr_2O_3 oxide layer is the predominant oxide scale. Air oxidation at atmospheric pressure for most temperatures

show that a two-oxide scale is formed, the outer layer is iron oxide, Fe_2O_3 , forming before the inner iron-chromium oxide, $(\text{Cr}_x\text{Fe}_{1-x})_2\text{O}_3$. If the $(\text{Cr}_x\text{Fe}_{1-x})_2\text{O}_3$ oxide layer is Cr-rich, then this scale system becomes very good against high temperature reaction. If Cr cannot diffuse quickly enough to the surface to enrich the oxide with Cr, then the $(\text{Cr}_x\text{Fe}_{1-x})_2\text{O}_3$ layer becomes Fe-rich, which is non-protective oxide layer.

Grain refinement, which facilitates Cr diffusion, shall improve oxidation resistance of austenitic stainless steel. The oxidation behavior of the austenitic stainless steel 347, with different grain sizes was studied to quantify the role of grain size and grain-boundaries on the oxide scale formation [59]. The oxidation kinetics of samples with a grain size of 4 μm obeyed a parabolic rate law. On the other hand, at a grain size of 65 μm , the weight gain is enhanced and the oxidation kinetic is more complex, exhibiting a stepwise parabolic oxidation, as shown in Figure 2.11. SEM examinations indicated that the scale formed on the specimens possessing the smaller grain size was predominantly Cr_2O_3 , with some FeCr_2O_4 at localized sites. For the specimens with the larger grain size, the scale is mainly composed of iron oxide. The results of this study showed that the protective Cr_2O_3 formation is promoted by a higher density of fast diffusion paths (grain boundaries), which was the case for the fine-grained materials. Oxidation of nanocrystalline 304 austenitic stainless steel coatings possessing an average grain size of ~ 12 nm was compared to coatings with coarse-grained (~ 20 μm) at temperatures ranging between 700 and 900 $^\circ\text{C}$ in flowing air with H_2O vapor content varying between 0–40%. Catastrophic oxidation of the coarse-grained sample was observed due to the formation of the non-protective $(\text{Cr}_x\text{Fe}_{1-x})_2\text{O}_3$, Fe-rich oxide combined with the water-vapor-promoted

evaporation of the chromia-based oxide scale. In contrast, substantial improvement in the oxidation resistance for the nanocrystalline 304 stainless steel was obtained, where abundant grain boundaries greatly enhanced the Cr diffusion to guarantee the stable growth of $(Cr_xFe_{1-x})_2O_3$, Cr-rich oxide scale. This enhanced diffusion for the nanocrystalline 304 coatings is highly sufficient to balance the consumption of Cr by vaporization and by oxidation [52].

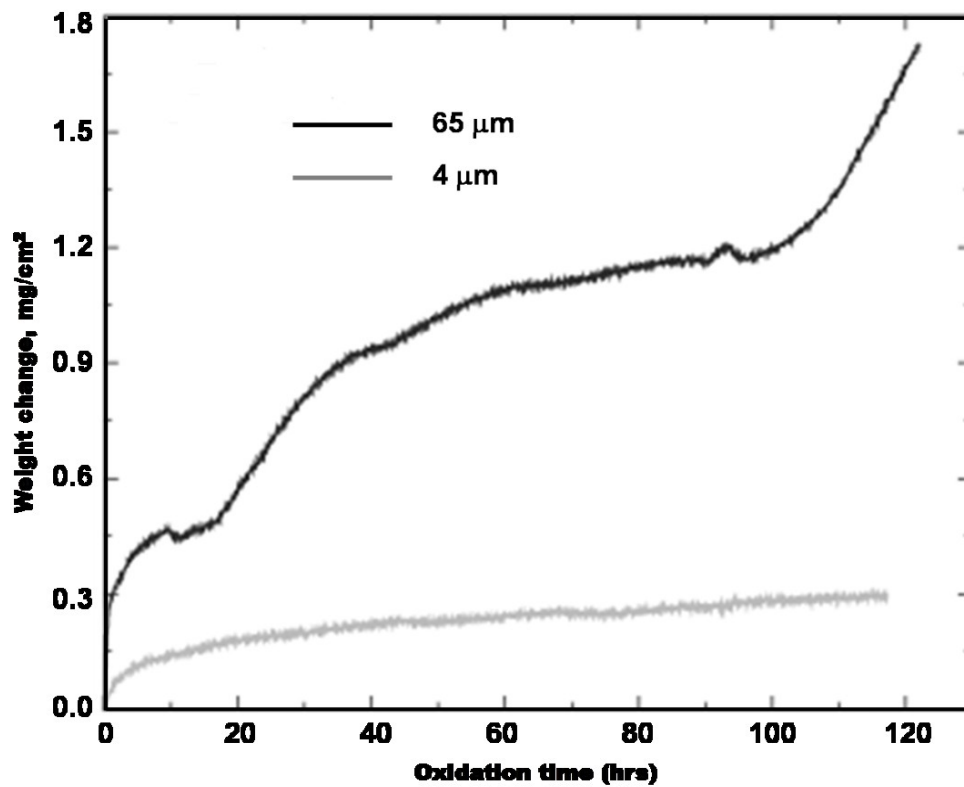


Figure 2.11 Oxidation kinetics of austenitic stainless steel 347 with different grain sizes exposed at 750 °C [59].

At elevated temperatures and in severe environments, Cr_2O_3 is not the ultimate oxide scale to maximize the oxidation resistance for austenitic stainless steel. Aluminum oxide (Al_2O_3) becomes the required scale for improved corrosion resistance. Alloying Al with

austenitic stainless steel promotes the formation of the Al_2O_3 scale in lieu of the Cr_2O_3 scale.

2.8 Aluminum Oxide at High Temperature

Thermodynamically, aluminum oxide is one of the most stable oxide layers as illustrated in Figure 2.6, and one with the lowest oxide kinetic growth rate as depicted in Figure 2.7. Aluminum oxide forms at high temperature according to equation 6. Brief review of the properties, behavior, kinetic and performance of aluminum oxide scale in engineering alloys is presented below.

2.8.1 Properties and Behaviors of Aluminum Oxide in Alloys

Aluminum oxide scales generally provide better oxidation resistance and yield lower oxidation rates than scales forming from other elements. A major of investigators believe that the aluminum oxide scale nucleation and growth is dictated by solid-state diffusion, and particularly grain boundary diffusion [49]. Most investigators conclude that the transport of the reacting atoms or ions predominantly involves inward oxygen transport along grain boundaries. An increase in the grain boundaries concentration for alloys should provide a significant increase in the number of possible nucleation sites for aluminum oxide. However, the wrinkling and convolutions of aluminum oxide scales

similar to that for oxide scales suggest that some outward diffusion of Al also takes place [49]. The outward flux of Al during the oxidation of four similar Fe-Cr-Al-base alloys was studied in air over a temperature range of 1000-1200 °C. Outward diffusion of Al through the oxide was observed to occur during oxidation of all four alloys, and was believed to significantly contribute to the oxide thickening rate at all temperatures investigated. The oxide morphology and the rate of oxide thickening, as well as the ratio of Al outward diffusion to oxygen inward diffusion, were different and based on the type and form of the added reactive element to the alloy [60].

2.8.2 Oxidation Performance of Al-containing Alloys

Fe-Cr-Al ferritic alloys have interesting oxidation behavior because Al competes with Cr in some composition ranges to give the protective scale. It is well known that it is easier to establish and maintain Al₂O₃ scales on Fe-Cr-Al alloys than on Fe-Al alloys [1]. This may be partly because Cr tends to stabilize α -Al₂O₃ formation. A more general criterion is, however, that Cr reduces the entry of oxygen into the alloy, thereby promoting a complete external layer of Al₂O₃ scale, rather than its precipitation as internal oxide [1]. This is because Cr₂O₃ and Al₂O₃ predominate over iron oxides in the initial nucleation of the scale and that Cr₂O₃ supplies oxygen to the alloy slower than iron oxides. Consequently, more opportunity is given to the Al to diffuse towards the surface and supply the Al oxide layer immediately beneath the thin, initially nucleated scale [61]. F-1 ferritic alloy (Fe-15Cr-4Al) was compared with different alloys, mostly austenitic

stainless steel, using cyclic oxidation in air at 1200 °C (400 cycles, 30 min in the furnace and 30 min out of the furnace). All the alloys tested except F-1 alloy suffered severe oxidation attack as shown in Figure 2.12. This illustrates the superior oxidation resistance of Al oxide [1]. The oxidation and corrosion properties of alloys based on compositions of Fe-40Cr and Fe-35Cr-5Al were studied using gravimetric technique at 1200 °C. The study showed that a high resistance to breakaway oxidation was inherent at high Cr levels. Alloying with Al furthermore proved to be effective in increasing the oxidation resistance by up to an order of magnitude [61].

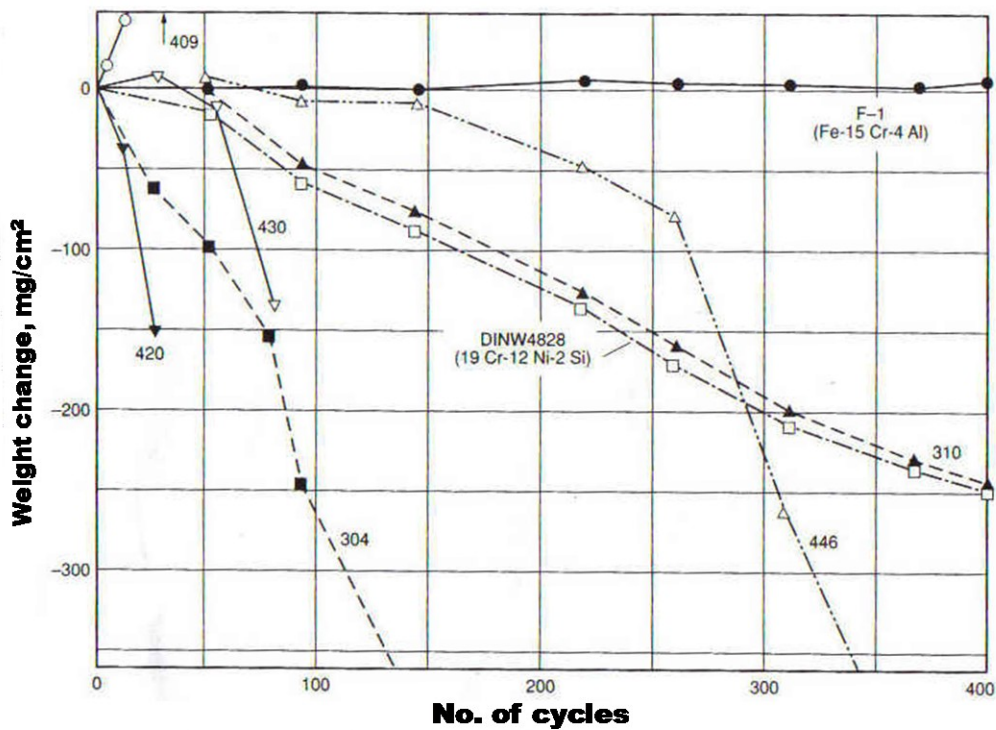


Figure 2.12 Cyclic oxidation for several ferritic and stainless steel in air at 1200 °C [1].

The behavior of Al_2O_3 layers on ferritic steels (Fe-Al) and austenitic steels (Fe-Ni-Al) with small additions of titanium, zirconium, niobium and vanadium was studied by measuring radiocarbon penetration in thermal cycling and creep experiments. The Al_2O_3 layers on the ferritic steels adhered well and were dense, which provided high resistance for carbon uptake. In the creep testing of the austenitic stainless steel, cracking of the Al_2O_3 layer and subsequent intergranular oxidation and uptake carbon were observed [63]. Belen et al. [64] studied the oxidation kinetics and morphological development during reaction of two cast-austenitic stainless steel at 1000 °C in pure dry oxygen. Both steels contained approximately 25 wt.% Cr and 35 wt. % Ni and, in addition, the steel contained 3.3 wt% Al. In the Al-containing steel, the rate of oxidation was significantly lower than in the Al-free stainless steel. This effect was attributed to oxygen flux consumption in forming large quantities of Al_2O_3 precipitates [64].

Since Cr is a strategically critical metal, it is important to consider ways to reduce the use of Cr in austenitic stainless steel. Significant alloying development was done to replace partially Cr with Al in austenitic stainless steel. These alloys contain only 10% Cr as compared with the 18-20% found normally in 300 series. The high Al, low Cr stainless steel forms a thin, adherent Al oxide film during high temperature oxidation, which is nonspalling and extraordinarily protective for the base metal. The oxidation behavior of such alloy (Fe-24%Ni-10Cr-5%Al) showed superior resistance in the temperature range of 800-1100 °C and moderate oxidation resistance up to 1300 °C. The excellent oxidation resistance is attributed to the formation of continuous Al_2O_3 oxide film [65].

Twelve typical high-temperature nickel-, cobalt- and iron- based alloys containing Al were tested using 1 hr cyclic exposures at different temperatures [66]. The alloys were also tested in both a dynamic burner rig and in a static air furnace for times up to 100 hr. The alloys studied fall into major classes with the followings characteristics:

1. Cr_2O_3 -chromite spinel control: Ni-, Fe-, or Co-based alloys with $>16\%$ Cr and $\sim 3\%$ Al or less. These alloys, particularly in cyclic high velocity tests, need as much Cr as possible to promote Cr_2O_3 scales and thus delay chromite spinel formation due to Cr depletion. Chromite spinel formation leads to severe spalling when cooled. The Co spinel of the type CoCr_2O_4 spalls more severely than the comparable Ni spinel. Spalling appears to be inhibited by Si, La, and Al. Example of Cr_2O_3 -chromite spinel formers is IN-601 (Ni-14.1% Fe-23%Cr-0.1%C-1.35%Al).
2. $\alpha\text{-Al}_2\text{O}_3$ –aluminate spinel control: 4 to 6% Al and greater than about 5% Cr are required to stabilize Al_2O_3 with Cr_2O_3 in Ni-, Fe-, or probably Co-based alloys. Both $\alpha\text{-Al}_2\text{O}_3$ and aluminate spinel are highly protective. In the Ni-base system, the Cr and Al contents, and particularly the Cr to Al ratio, appear critical. These alloys normally fail by NiO formation when the Al levels drops below about 3% with the Cr level too low to form Cr_2O_3 or chromite spinel (critical level under the 16 to 20%). In the dynamic tests, it appears that enhanced Cr depletion due to high gas velocity lowers the Cr to Al ratio, favoring Al_2O_3 over Cr_2O_3 formation. Examples of $\alpha\text{-Al}_2\text{O}_3$ –aluminate spinel forms are IN-100 (Ni-23%Co-10%Cr-3%Mo-0.18%C-5%Ti-5.5%Al) and GE-1541 (Fe-15%Cr-4%Al) [66].

In general, for all based alloys, Al_2O_3 is a highly protective scale to environmental attacks. The formation of Al_2O_3 should be continuous, compact and adherent to the metal to provide maximum corrosion protection. A comparative study of the effect of adding small additions of silicon or Al (1 wt. %) on the oxidation of the based alloy showed that Al is the most effective addition in this respect, due to formation of a higher population density of oxide nuclei in the early stage. However, in the 1% Al alloy, the precipitates penetrated inward, to considerable depths and as continuous platelets, making the development of a complete protective layer difficult. In practice, the higher the Al concentration is necessary for the closely spaced precipitates to coalesce to form the forming layer [67].

2.8.3 Difficulties in Forming Protective Aluminum Oxide

High temperature alloys depend on the development of adherent, non-volatile, non-porous, crack-free scales containing low defect concentrations to enhance oxidation resistance. At very high temperatures, alloys capable of developing an external Al_2O_3 -rich scales have greater potential for oxidation resistance than those developing other oxides like chromium oxide. The concentration of Al in the alloy should be above the critical concentration necessary to establish a complete pore-free surface layer of Al_2O_3 .

The critical concentration of Al above which Al_2O_3 is formed is given by [61]:

$$N_{Al} = \frac{v}{Z_{Al} M_0} \times \left(\frac{\pi k_p}{D} \right)^{\frac{1}{2}} \quad (12)$$

Where v is the molar volume of the alloy; Z_{Al} is the valence of the Al atom; M_0 is the atomic weight of oxygen; D is the diffusion coefficient of Al in the alloy; and k_p is the rate constant for oxidation.

The above equation gives arbitrary figures. In practice, the situation is more complex and different depending on the alloy composition and oxidizing conditions. The rate constant of oxidation depends on the oxygen pressure and the exposed temperature. Also, it has been shown that the diffusion coefficient is a function of alloy composition and temperature, and diffusion becomes a complex phenomenon for alloys having many components. In environment containing oxygen, the alloy components have a different affinity for oxygen and do not diffuse at the same rate in the oxide or the alloy. Consequently, the oxide scales and alloy compositions change in a complex way with time [61]. Oxidation of Fe-15Cu-5Al alloys at 700 °C is not able to form a continuous protective Al_2O_3 layer. That is to say, 5% of Al is below the critical Al content to form the external Al_2O_3 scale on Fe-15Cu-5Al at 700 °C. At 800 °C, the situation is the opposite, the alloy forms a protective external Al_2O_3 scale. The lower temperature may slow down the diffusion rate of Al in the alloy toward the alloy/scale interface. Thus, it is

deduced that 5% Al is above but near the critical Al content needed to form the external Al_2O_3 scale at 800 °C [68]. Similar results were obtained for stainless steel. The effect of adding up to 2 wt.% of Al and Si on the oxidation of austenitic stainless steel with a baseline composition of Fe-16Cr-16Ni-2Mn-1Mo has been studied at 800 °C. Alloys that contain Al showed poor oxidation and weight gains approximately two times greater than the baseline compositional alloy [69]. It is concluded that 2 wt.% of Al is below the critical concentration to form the desired external protective Al_2O_3 layer on Fe-16Cr-16Ni-2Mn-1Mo-2Si at 800 °C.

The alloy composition can also affect the critical concentration of Al for an alloy required to form the external Al_2O_3 scale. At the same concentration of Al, trace amount of some elements could play an important role in the transformation from internal oxidation to the development of the external protective Al_2O_3 scale. Al concentration of 2.4 wt% and trace amounts of B, C, Nb, P, Ti, and V elements were added to Fe-14Cr-20Ni-2.5Mo-2Mn austenitic stainless steel alloy to make HTUPS 2 alloy [70]. The same Al concentration and similar amount of B, C, Nb, P were added to make HTUPS 4 but Ti, and V were not added. Oxidation of HTUPS 2 for 72 hr at 800 °C in air resulted in the formation of internal Al-rich oxide and external oxide consisting of the non-protective mixed Fe and Cr oxide phases as shown in Figure 2.13 (a). It was concluded that 2.4 wt.% of Al was not sufficient to form the continuous external Al_2O_3 scale for this alloy. On the other hand, oxidation of HTUPS 4 under the same conditions resulted in the formation of an external and continuous Al-rich oxide scale, as shown in Figure 2.13 (b). For the same Al concentration, the transformation from continuous external Al-rich oxide scale (HTUPS

4) to poor external scale combined with internal oxidation (HTUPS 2) was associated with the addition of trace amounts of Ti, and V to the HTUPS 2 alloy. The critical concentration of Al needed to form the external scale can be described by a flux criteria based on a competition between inward oxygen permeation and outward Al diffusion. Alloying additions that increase oxygen permeability or decrease Al diffusivity would raise the amount of Al needed for the development of the protective alumina scale formation. Given the high thermodynamic stability of Ti and V with oxygen, additions of Ti and V may be expected to promote an increased tendency for internal oxidation because of increased oxygen permeability [70].

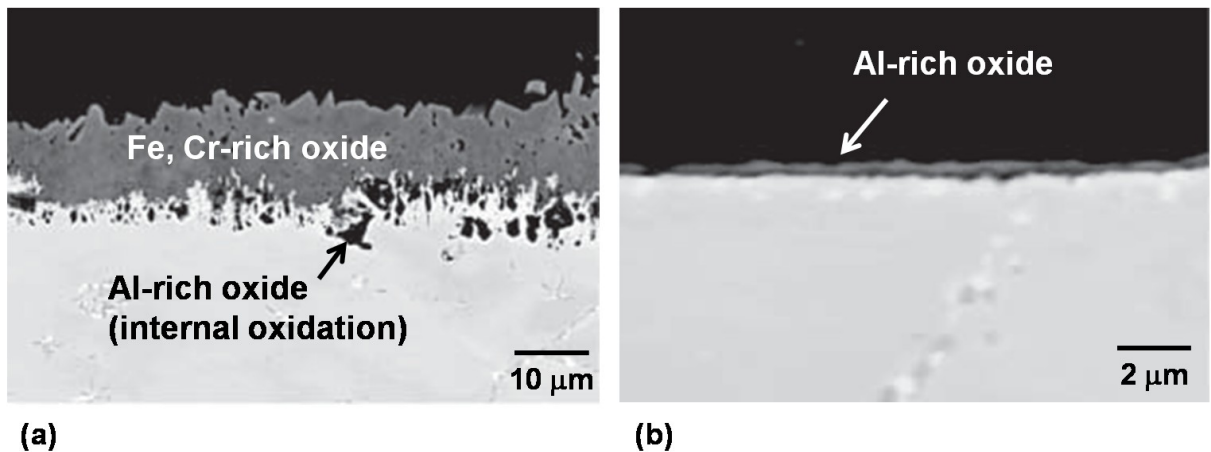


Figure 2.13 Backscatter electron images after 72 hr of oxidation at 800°C in air. (a) HTUPS 2, (b) HTUPS 4 [71].

In addition, Al_2O_3 scales formed on some high temperature alloys, such as those based on Ni-Al, Ni-Cr-Al and Co-Cr-Al chemistries, tend to spall, particularly during thermal cycling. Additions of elements like yttrium help in preventing spalling of the oxide scales [71].

2.8.4 Aluminum and Aluminum Oxide in Nanostructured Materials

Nanostructured materials often possess special properties that materials with identical compositions but ordinary grain size do not have. One of the most important advantages of nanocrystalline materials is the ability to promote selective oxidation. Nanostructured materials provide two significant contributions to the formation of an external oxide scale. The first is to provide more nucleation sites of oxide due to an increase in the concentration of grain boundaries on the alloy surface. The second is to increase the diffusivity of solute in the alloy through grain boundary diffusion [72,73]

Engineering alloys rely on the formation of protective oxide films such as Al_2O_3 , to resist high-temperature and corrosive environments. Unfortunately, for conventional alloys, large concentration of Al is needed to reach the critical concentration and to form a complete Al_2O_3 scale. In the Ni-20Cr-Al alloy system, for instance, >6 wt.% Al is required to form a complete Al_2O_3 scale. High Al contents, however, often degrade the mechanical properties of the alloys. If the Al content is lower than 6 wt.%, complex oxides consisting of Cr_2O_3 , NiCr_2O_4 and internal oxide of Al_2O_3 may form, resulting in high reaction rates and poor oxidation resistance [5]. With nanostructured alloys, the Al content that is required to form a complete protective oxide scale can be substantially reduced. Experimental results indicated that when the grain size of Ni-20Cr-Al was in the level of ~60 nm, alloys containing ~2 wt.% Al could form a complete $\alpha\text{-Al}_2\text{O}_3$ scale at 1000 °C in air, as shown in Figure 2.14. This concentration is only 1/3 of the required Al

contents in the Ni-20Cr –Al alloy with conventional grain size. Due to formation of the highly protective α -Al₂O₃, the oxidation rate of the nanocrystalline coatings is much lower than that of the coatings with the same composition but with larger grain size. The detailed study showed that the composition and the microstructure of the oxide scales are function of the coating grain size. The relationship between the oxide products, coating grain size and Al content, indicate that the selective oxidation of Al is greatly promoted by the nanocrystalline structure. Nanocrystallization decreases the critical Al content required in an alloy to form the external α -Al₂O₃ scale, in effect changing the scale composition from a chromate to an alumina, with a corresponding improvement in the oxidation resistance. The promoting effect of nanocrystalline grains on selective oxidation is attributed to short-circuit outward diffusion of Al through the grain boundaries [5].

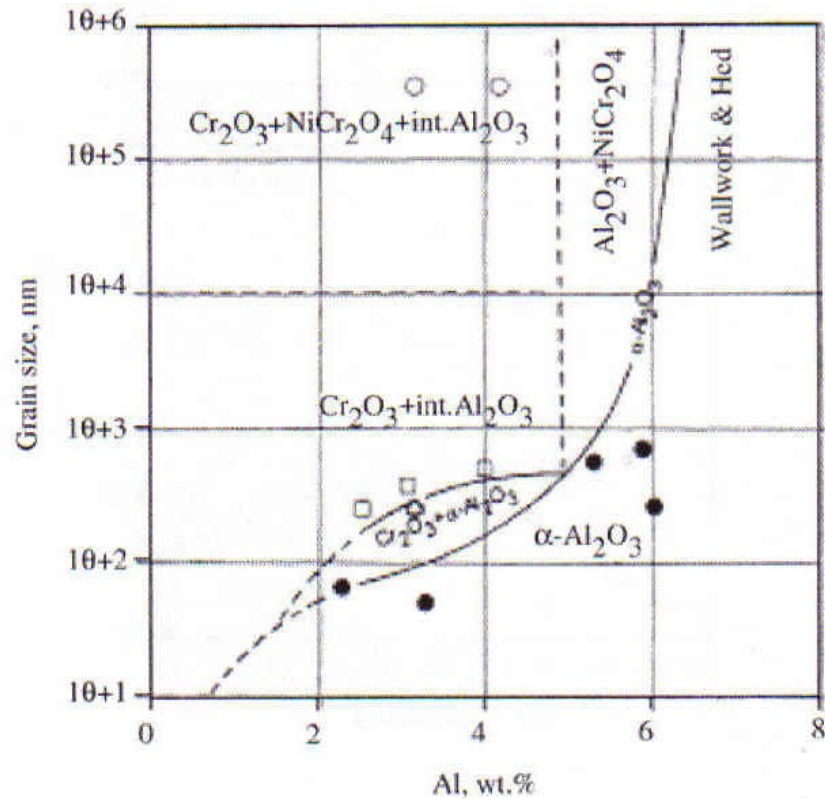


Figure 2.14 A diagram showing the relationship of grain size, Al content, and oxidation products for Ni-20Cr-xAl at 1000 °C and air [5].

As can be seen from the above results, the critical solute concentration in nanocrystalline alloys required to form a continuous external oxide scale can be reduced due to the increase in solute diffusion coefficient, D . Wang [74] derived a relationship between the critical solute concentration (N) and grain diameter (d) for nanocrystalline alloys based on Wagner's equation. For the nanocrystalline alloys, Wang substituted the solute diffusion coefficient of Wagner's equation by the effective diffusion coefficient (D_{eff}) which is a combination of grain boundary diffusion coefficient (D_{gb}) and bulk diffusion coefficient, (D_b).

Wang's equation for critical solute concentration (N) in nanocrystalline alloys required to form the continuous external oxide scale is as follow:

$$N = K\sqrt{d} \quad (13)$$

where K is a constant. The critical solute concentration is directly proportional to the square root of the grain diameter. It should be noted that Wang's theory has two hypotheses, firstly, the grain size does not affect the oxygen permeability and secondly, the grain boundary diffusion predominates in the alloy due to the nanostructure.

On the other hand, some researchers found that for long oxidation of nanostructured Al-containing coatings, a pure external Al_2O_3 did not form. A commercially available gas-atomized Co-32Ni-21Cr-8Al-0.5Y powder was cryomilled to produce powder with nanocrystalline grains. The cryomilled powders and conventional gas-atomized powders were thermally sprayed using the HVOF process to prepare two coatings with fine-grain (15 nm) and coarse-grain (1 μm) microstructures, respectively. The influence of the grain size on the oxidation behavior was investigated by comparing the morphology and composition of the oxide scales formed on the two coatings during isothermal oxidation in air at 1000 °C for 1, 24, and 330 hr. The results indicated that the nanostructured coatings promoted the formation of a pure Al_2O_3 layer on the coatings by increasing the Al diffusion rate toward the surface, which simultaneously accelerated the Al depletion by increasing the Al diffusion toward the surface, resulting in the formation of non-alumina oxides after long-term oxidation [75]. Chen and Lou [76] investigated the

oxidation behaviour of Ni–8Cr–3.5Al alloy with nanograin and coarse grain microstructures at 1000 °C in air. Complex, layered-oxide scales composed of a Cr₂O₃ outer layer, a mixed spinel NiAl₂O₄ and NiCr₂O₄ intermediate layer, and an Al₂O₃ inner layer formed on the nanocrystalline Ni–8Cr–3.5Al coating after 200 hr of oxidation, whereas Cr₂O₃, with a NiCr₂O₄ external layer and an internal Al₂O₃ layer formed on the conventional alloy.

In addition to oxidation selectivity, nanostructured coatings containing Al offer a very adherent and continuous oxide scale. Comparison of cyclic oxidation study of Ni-20Cr3.5Al was conducted for three different average grain sizes, an as-cast alloy (average grain size ~0.4 mm), a submicro-crystalline coating (~0.5 μm) and a nanocrystalline coating (~50 nm). Both the nano and submicro-crystalline coatings showed good scale spalling resistance when compared to as cast alloy [5]. Therefore, there is additional positive effect of nanocrystallization on scale adhesion. The scale adhesion is dependent upon two factors: (1) thermal stresses in the oxide scales and (2) bonding between the oxide scale and the substrate. Both factors can be affected by nanocrystallization [74]. Based on the diffusion creep theory, which is a function of solute diffusion coefficients, theoretically, the thermal stresses in the scale forming on the nanocrystalline coatings should be lower than those formed on coarse-grain alloys, due to enhanced compliance of the oxide scale and the substrate. The bonding force of the oxide scale is directly proportional to the ratio of grain boundaries per unit area, assuming that the oxide scale is anchored to the substrate only by the pegs formed along grain boundaries. Therefore, since the volume fraction of grain boundaries of the nanocrystalline coatings is several

orders of magnitude larger than that of the normal grain-size alloys, the bonding strength of the scale formed on the nanocrystalline coatings is much greater than that on the normal grain-size alloy [74]. These two mechanisms may account for the excellent adhesion of the scale formed on the nanocrystalline coatings.

3. METHODOLOGY

The methodology followed in this study was design to better understand the effects of alloying various concentrations of Al with stainless steel on the phase transformations during cryomilling and annealing, grain growth and oxidation behavior of the nanocrystalline alloys. The flow chart of the experimental methodology is shown in Figure 3.1 and details about the respective steps are given in the in following sections.

3.1 Raw Materials

316L austenitic stainless steel powders (17%Cr, 13.5%Ni, 2.2%Mo, 0.14%Mn, 0.81%Si, 0.02%C, balance Fe) from North American Hoganas and Al powders from Atlantic Equipment Engineers were used as the starting powders. The detailed chemical composition of the raw materials used for this study to produce the synthetic powders is given in Table 3.1. The design criteria of various concentrations of Al will be discussed in detail in the results and discussion chapters.

Table 3.1 Chemical compositions of the powders used in this study

Alloy	Chemical Composition	Comments
A	316L stainless steel	As received
B	316L stainless steel	Cryomilled
C	Alloy + 2 % Al	Cryomilled
D	Alloy + 6 % Al	Cryomilled

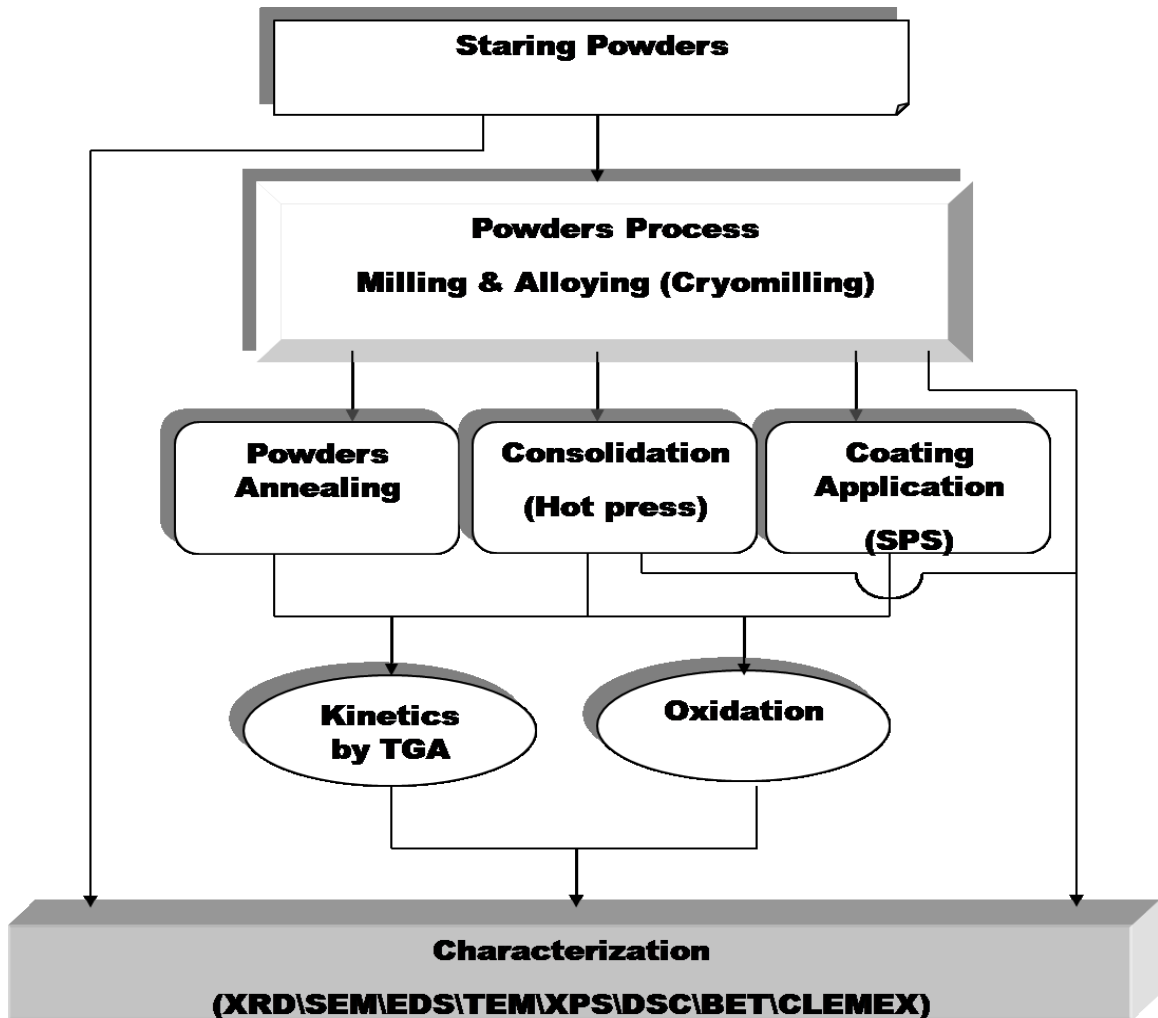
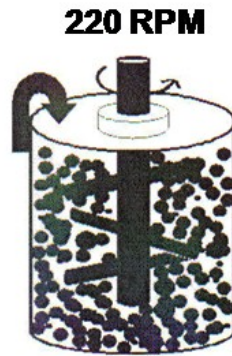


Figure 3.1 Flow diagram showing the experimental methodology.

3.2 Mechanical Alloying and Nano-Grain Structuring

The cryomilling process was done in a Union Process 1-HD attritor simultaneously to alloy the powders and to refine the grains to nanometer scale. Figure 3.2 presents a schematic of the apparatus. 440-C stainless steel balls are used as grinding media and the apparatus includes a thermocouple (K-type) to monitor the temperature in the attritor and to ensure that a constant level of liquid nitrogen is maintained. Evaporated nitrogen from the milling vessel is compensated by continuous feeding of liquid nitrogen to ensure complete immersion of the powders. The shaft rotation was kept constant at 220 RPM and a powder to ball weight ratio of 1:20 was used. 120 grams of powders were charged for each batch and mixed with 2 to 5 mg stearic acid which used in the process as controlling agent to balance between fracture and wilding process during cryomilling. The milling time was 32 hr in order to obtain complete alloying of the powder. Every 8 hr, a sample was taken from the attritor for characterization and verification of complete alloying.



(a)



(b)

Figure 3.2 (a) Schematic design of a typical cryomilling attritor mill (b) Photograph of a mill in use

3.3 Powders Consolidation (Hot Press)

Cryomilled powders were consolidated using a hot press. Approximately 4 g of milled powders were placed in a cleaned die. The powders were initially cold pressed using a pressure of 36-40 kPa. Then the die was placed in a hot furnace which was evacuated using a mechanical pump to minimize oxidation during consolidation. The powder was compacted under a pressure of 76-103 kPa while the furnace temperature was set at 450 °C. The consolidation pressure was maintained for two hr. Figure 3.3 shows a hot pressed compact.



Figure 3.3 The consolidated powders prior the oxidation test

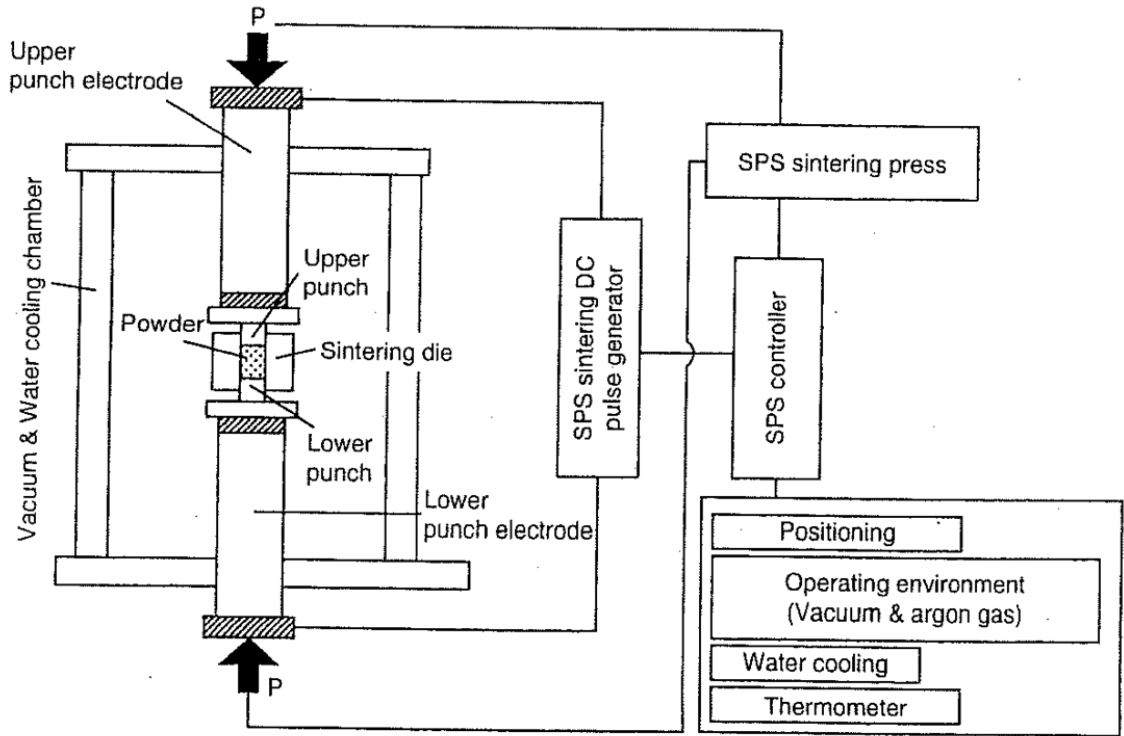
3.4 Spark Plasma Sintering

Dr. Sinter SPS press (model 515-S, Figure 3.4) was used to consolidate the cryomilled powders. The nanostructured powders were sintered on conventional stainless steel substrate, mimicking a coating. Figure 3.5 (a) shows the basic configuration of the SPS system. The system consist of a SPS sintering machine with vertical pressurizing mechanism, a vacuum/air/argon atmosphere mechanism, a DC-pulse sintering power

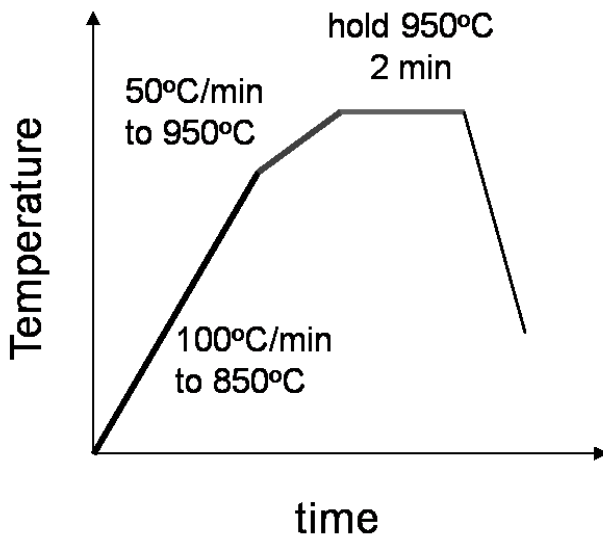
generator, a cooling water control unit, a temperature measuring unit, a position measuring unit, an applied pressure display unit and various interlock safety units. The powders were sintered in a vacuum environment at 950 °C in a graphite mold. The heating rate was 100 °C/min up to 850 °C, then 50 °C/min up to the sintering temperature, a holding time of 2 min was used as illustrated in Figure 3.5 (b).



Figure 3.4 Spark Plasma Sintering (SPS) system.



(a)



(b)

Figure 3.5 (a) SPS configuration system (b) heating rate and sintering time and temperature.

3.5 Measurement of Surface Area Using BET Technique

The surface area of the powders were determined by the Brunauer–Emmett–Teller (BET) technique using a Micromeritics Tristar 300 instrument, illustrated in Figure 3.5. The determination of the surface areas of powders was used to calculate the kinetic oxidation rate of the powders. Approximately 0.5 g of each sample was prepared for the BET test by degassing to remove moistures and contaminations prior to analysis. A degassing period of two hr was used and was done by passing a gas through the test tubes heated to 250 °C. After degassing, the powder samples were installed in the instrument and the BET test was run. The instrument was calibrated before each run using standard reference material (carbon black) of known surface area.



Figure 3.5 Micromeritics Tristar 300 BET instrument.

3.6 High Temperature Preparation and Evaluations

3.6.1 Powder Annealing

The three different compositions of milled powders (316LSS, 316LSS-2 wt.% and 316LSS-6 wt% Al) were annealed at temperatures of 500 °C, 800 °C and 1000 °C, respectively, for 1 hour. The annealing apparatus is shown in Figure 3.6. The powder sample was introduced in the furnace tube at room temperature and it was purged with argon several times before and during evacuation. When the target vacuum was reached (20-60 m Torr), the tube furnace was heated to the target temperature. Upon completion of soaking period, the furnace temperature was shut down and the sample was cooled inside the furnace under vacuum environment to room temperature.

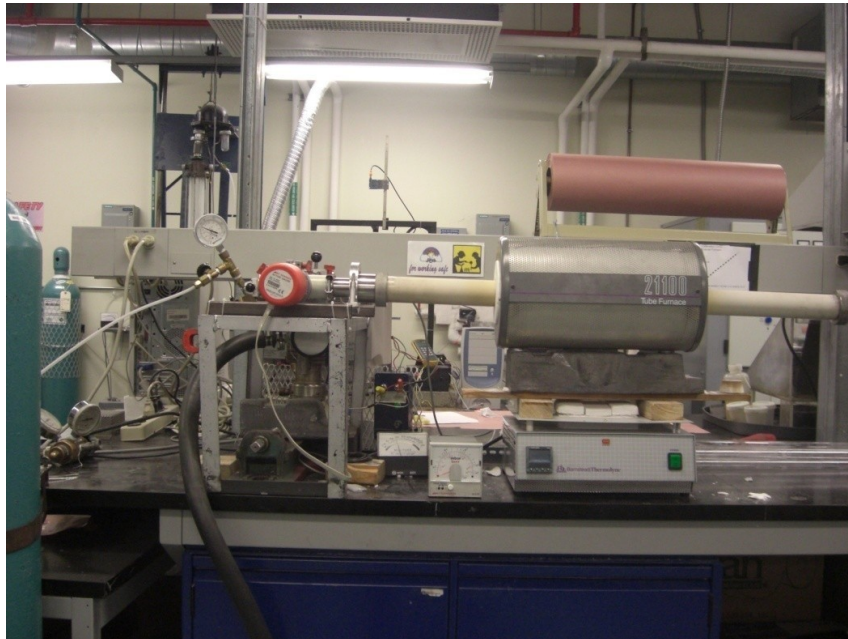


Figure 3.6 Annealed furnace integrated with vacuum system.

3.6.2 High Temperature Oxidation

High temperature oxidation tests were conducted in air at three different temperatures: 500 °C, 800 °C, and 1000 °C, respectively. Isothermal oxidation for 48, 200, 500 hr and cyclic oxidation (10 cycles, 50 hr per cycle) were used at all temperatures. The proposed temperatures cover different zones in the furnaces and boilers used in the oil industry. A furnace from Lindberg/Blue M model BF51732C was used for this test. The furnace was heated to the desired temperature, then the powder samples contained in Al₂O₃ crucibles were introduced in the furnace. The oxidized samples from this test were used to study the surface morphology and the oxide scale developed at the surface of the powders.

3.6.3 TGA Experiments

Oxidation kinetics were measured using a gravimetric method, which is widely used to study oxidation and other forms of high-temperature corrosion. The actual setup for the thermogravimetric analysis is shown in Figure 3.7. The tests of the samples were carried out in a vertical mullite tube furnace. A thermogravimetric balance (Cahn D-100, Cerritos, CA) was located on the upper part, well outside of the hot zone, to protect the electronic devices. The temperature in the furnace was measured with a B-type thermocouple, having an accuracy of $\pm 1\%$, controlled by a Gultan West 2050 temperature controller. Six SiC GLOBAR heating elements, arranged in a circular manner, were used as the heating source.

The samples were placed in the alumina crucible hanged in the middle of the hot zone. A pre-oxidized Ni-Cr wire gripped to the thermogravimetric balance was used to hold the crucible in the tube furnace. The length of the wire was measured carefully to ensure that the crucible was placed in the hot zone, near the thermocouple. The placement of the crucible was also examined to ensure that the crucible was not touching the mullite tube, and that it was suspended freely for accurate weight change data acquisition.

The furnaces chamber was evacuated to 300 m Torr using a mechanical pump, and flushed with argon. After repeating the evacuation procedure twice, argon gas was introduced into the system from the lower part of the furnace and allowed to flow out at the top. When a continuous flow of argon was obtained, the temperature controller was set to the testing temperatures (500 °C, 800 °C and 1000 °C) and the furnace was heated at a rate of 10 °C/minute in order to protect the mullite tube. When the furnace reached the test temperature, dry air was introduced into the system and data acquisition (weight change) begun. Argon and dry air flow were controlled using a flow meter.

The weight change data acquisition through the microbalance was gathered using Thermo Cahn Microscan acquisition software, and the data was converted into a Microsoft Excel spreadsheet program in order to plot the weight change versus time graph. The measurements were preformed for a period of 48 hr, in order to have a better understanding of the oxidation kinetic of the samples.

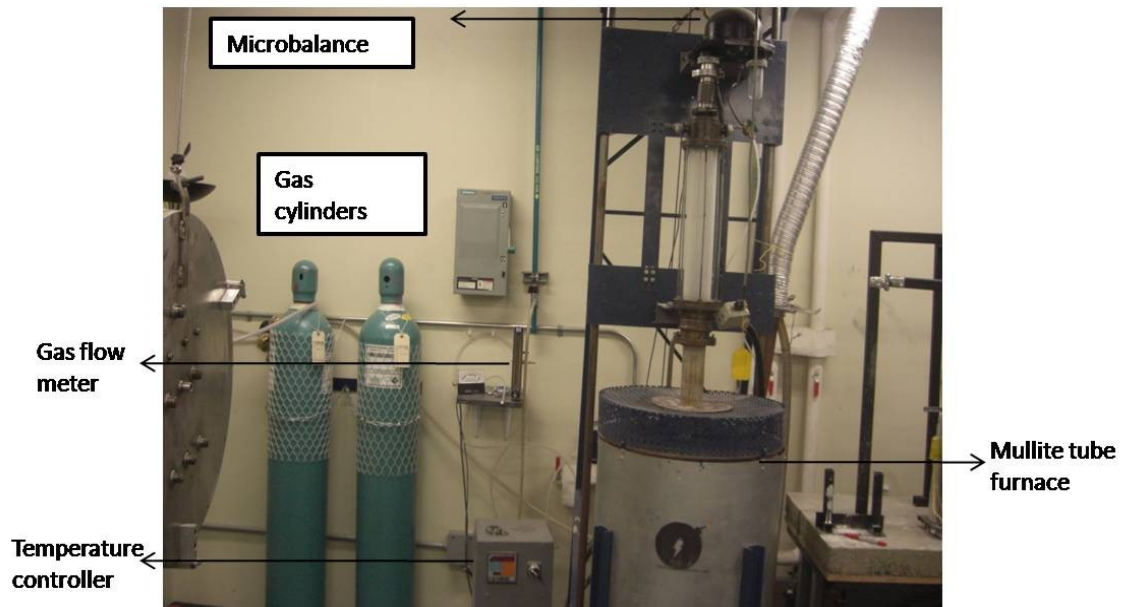


Figure 3.7 Actual setup of the thermogravimetric analysis in the McGill Lab facility.

3.7 Sample Characterization and Analysis

3.7.1 X-Ray Diffraction (XRD)

Powders were characterized by means of X-Ray Diffraction (XRD) using an American Instrument, diffractometer shown in Figure 3.8. The diffractometer (CuK_α was the radiation source) was operated at 40 kV and 20 mA. Very low scan rate ($0.01^\circ 2\theta/\text{sec}$) were used to allow for calculation of XRD peaks broadening and fine phase deposition. The scanned angle range was 35 to 100. Mechanical alloying, phase transformation, phase identification and lattice parameters calculations were characterized by XRD. The

average grain size measurement was estimated from broadening of XRD peaks using Scherer formula.



Figure 3.8 X-Ray diffraction (XRD) from American Instruments

3.7.2 Scanning Electron Microscope (SEM)

Both oxide surface morphologies and polished cross-sections of the oxidized samples were examined using the JEOL JSM-840A scanning electron microscopy (SEM) and the Hitachi S-4700 field-emission gun SEM (Figure 3.9 and 3.10). The microscopes were operated at incident beam energy of 2 and 15 kV, respectively. Low incident energy was mainly use to characterize the thin oxide morphologies without interfering with the bulk

of the samples. Qualitative analyses and line scan of the oxide layer were performed using energy dispersive spectroscopy (EDS) coupled with the SEMs and connected to INCA software for element analysis. Samples used for SEM analysis were cold mounted for cross-sectional analysis. Conductive carbon Bakelite was used to prevent charging around the sample edges (surfaces). Samples were ground from 240 to 600 grit abrasive SiC grinding papers, and then polished using 9, 3 and 1 micron diamond powder slurries, respectively.

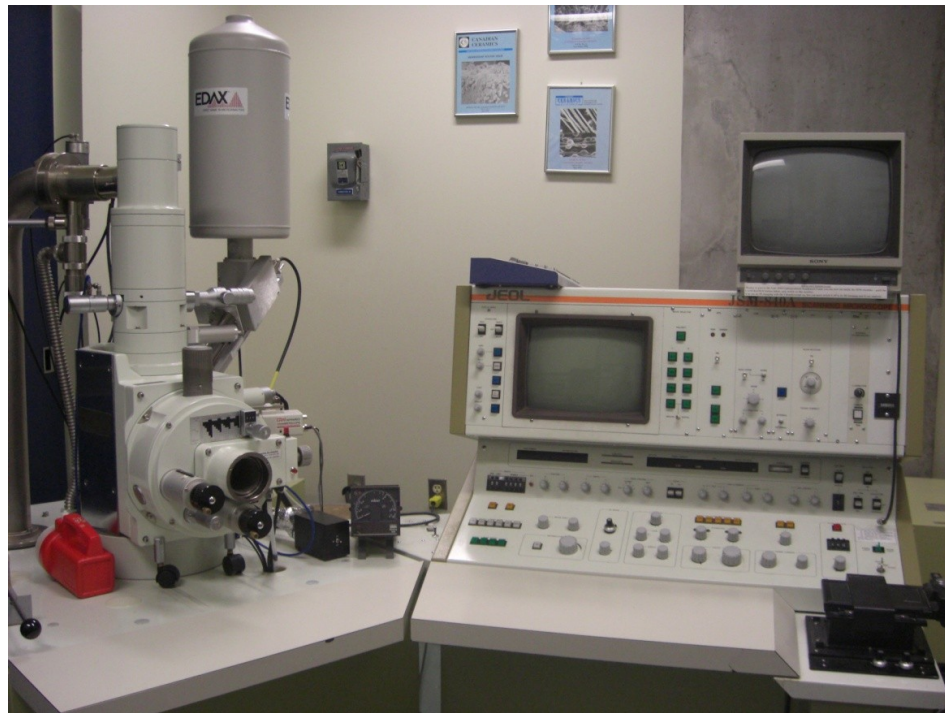


Figure 3.9 JEOL JSM-840A Scanning Electron Microscopy.



Figure 3.10 Hitachi S-4700 field-emission gun Scanning Electron Microscopy.

3.7.3 Transmission Electron Microscope (TEM)

The JEOL JEM-2011 transmission electron microscopy (TEM) shown in Figure 3.11, operated at 200 kV was used to examine the nanostructure of the powders. Micrographs from TEM were mainly used for grain size determination. A TEM diffraction pattern was used to verify phase structure and identify precipitation of phases that cannot be detected by XRD or SEM. The average grain size measurement was carried out using CLEMEX image analysis software on TEM dark and bright field micrographs. Powder samples were dispersed in alcohol and sprayed into carbon grids before examination.



Figure 3.11 JEOL JEM-2011 Transmission Electron Microscopy

3.7.4 X-Ray Photoelectron Spectrometer (XPS)

Oxide morphologies of powder samples were examined using a PHI-5700 X-ray Photoelectron Spectrometer (Figure 3.12). XPS is a powerful technique to analyze

chemical information of samples surfaces within the nanometer range. Approximately 30 mg of each sample were lightly pressed into a stainless steel sample holder using a stainless steel spatula. The samples were first analyzed using the broad, low-energy resolution spectral acquisition mode (survey) for surface elemental composition. They were then examined using the high-energy resolution spectral acquisition (multiplex) to determine chemical information about specific elements.



Figure 3.12 PHI-5700 X-ray Photoelectron Spectrometer

3.7.5 Differential Scanning Calorimetry (DSC)

The milled powder samples (approximately 10 to 15 mg in each case) were subjected to differential scanning calorimetry using SETSYS Evolution instrument from SETARAM

Scientific & Industrial Equipment under dynamic argon atmosphere as illustrated in Figure 3.13. The powder sample contained in Al_2O_3 crucibles, were heated up from room temperature to 1000 °C at heating rates of 20, 30 and 40 K/min.

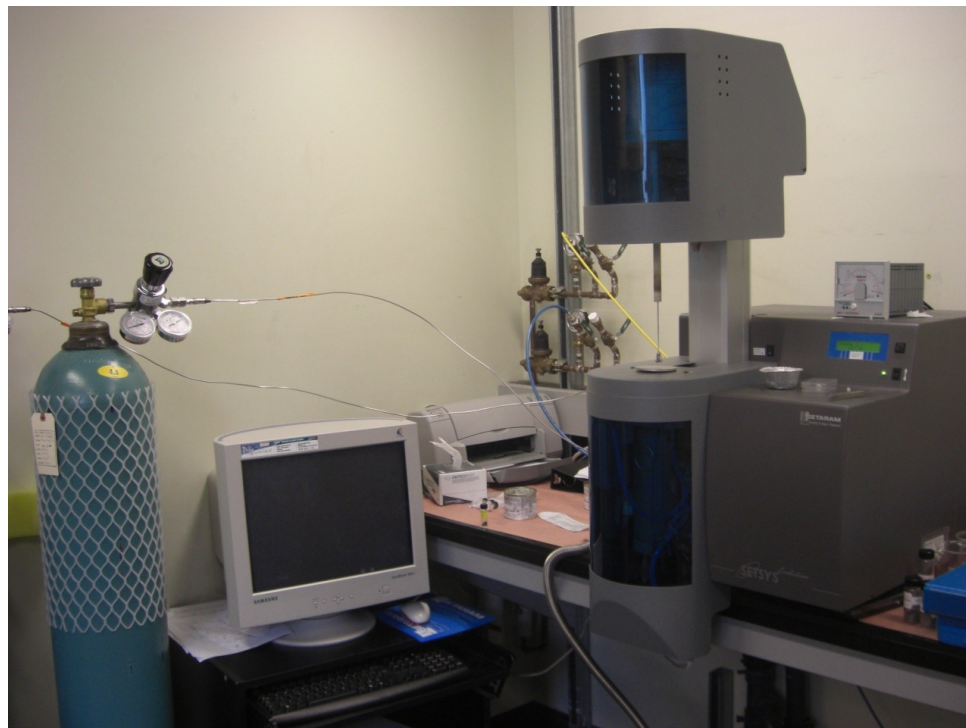


Figure 3.13 DSC SETSYS Evolution instrument from SETARAM

4. CRYSTAL STRUCTURE, TRANSFORMATION AND THERMAL STABILITY OF NANOSTRUCTURED 316LSS ALLOYED WITH 2 AND 6 wt% ALUMINUM

4.1 Introduction

Grain refinement to a nanocrystalline size is an effective method for improving the mechanical properties of materials [16], and can be obtained by high strain powder metallurgy processes, which combine mechanical milling, mechanical alloying and heat treatments [29]. Decreasing the crystallite structure of austenitic stainless steels to the nano regime through mechanical milling is usually accompanied by a strain induced phase transformation. A few contradictory works on mechanical milling of stainless steel were found in the literature, with most discrepancy surrounding the crystal structure obtained after deformation. Work done by H. Fujiwara on SS316L austenitic stainless steel powder showed a strain induced ferrite transformation from face centered cubic (FCC) to body BCC during mechanical milling using a planetary ball milling [29]. The crystal structure of the nano ferrite grain was identified through TEM and XRD and showed an average grain size of 15 nm with high angle boundaries [29]. On the other hand, A. Szymanska showed in the analysis of his ball milling work of commercial AISI 316L powders using Mossbauer technique that the FCC structure transforms to BCT martensite. Their analyses indicated that 50% of the austenite was transformed to martensite after 100 hr of milling [30]. In a similar austenitic system, using Mossbauer technique, H. Huang reported that mechanical milling (Spex mill) of 304 stainless steel

resulted in the formation of strain induced martensite [34]. They also showed that longer milling time, i.e. more than 400 minutes resulted in a reduction in the magnetization which was associated to the reversion of martensite to austenite during the repeated collision events and the larger volume of grain boundary developed during milling [34]. To determine the martensite-to-austenite reversion temperature, the powders were annealed for 30 minutes at various temperatures. Reverse transformation was detected using magnetization of ~ 140 emu/g. The reversion transformation started at around 500 °C and was found to be complete at around 800 °C [34]. Previous studies [35-36] suggested that temperatures as high as 500 °C can be locally reached during Spex milling collisions, reinforcing the possibility of inducing crystal structure reversion during milling. Maggy and Lavernia investigated the behavior and morphology of HVOF 316SS cryomilling coating [12] but no work focused on the strain induced transformation of stainless steel during cryomilling and heat treatment was found.

The present study shows the effect of different Al concentrations on the nanostructure formation and strain induced phase transformations of 316L austenitic stainless steel powders prepared by cryogenic mechanical milling. As opposed to the previous work, no crystal structure reversion is expected during the milling since it is carried out in a liquid nitrogen environment. Three alloys were studied: nanostructured 316LSS (nSS0Al), 316LSS containing 2 wt.% Al (nSS2Al) and 6 wt.% Al (nSS6Al). More specifically, the influence of the Al concentration on the reversion temperature was studied. In addition, the subsequent relation between the Al concentration and thermal stability of the different systems was investigated.

4.2 Experimental

Grade 316L austenitic stainless steel powder (17 % Cr, 13.5 % Ni, 2.2 % Mo, 0.14 % Mn, 0.81 % Si, 0.02 % C, balance Fe) supplied by North American Hoganas was used as the starting material. In addition, two Al-containing alloys, namely 2 and 6 wt.% Al were produced through the addition of elemental Al powder (Atlantic Equipment Engineers) prior to the milling. A Union Process attritor (HD-01) was used to cryomill the pre-alloyed and blended powders to the nanometer scale. 440-C stainless steel balls are used as grinding media and the apparatus includes a thermocouple (K-type) to monitor the temperature in the attritor and to ensure that a constant level of liquid nitrogen is maintained. The rotation speed was kept constant at 220 RPM and the powders were milled for 32 hr. A powder to ball weight ratio of 1:20 was used.

The three different milled powders were heat treated under an argon atmosphere at temperatures of 500 °C, 620 °C, 800 °C and 1000 °C for 1 hour. The as milled and heat treated powders were characterized by means of X-Ray Diffraction (XRD) in a Philips PW 1710 diffractometer using CuK_α radiation at 40 kV and 20 mA. A scan rate of 0.01° 2θ /sec was used to allow for calculation of crystal lattice parameter, grain size through peak broadening and identification of nano phases. The scanned angle range was 35 to $100^\circ 2\theta$. To determine crystal lattice parameters, powder samples were mixed with silicon standard powders before performing the XRD. Xlat software was used to calculate the lattice parameters of the powders.

Quantitative analysis of the volume fraction of crystal structures after heat treatment was measured using XRD patterns based on relative peak intensity ratio, as described by Cullity [77]. An intensity ratio calibration curve was produced using different mixtures of known composition so that the level of crystal structure reversion at the different annealing temperatures was accurately inferred. Differential Scanning Calorimetry (DSC) traces of the milled powders were acquired in a NETZSCH STA 449 C Jupiter DSC under argon atmosphere. The samples were heated from room temperature to 1000 °C at rates of 20, 40 and 45 °C/min. A JEOL JSM-840A scanning electron microscope (SEM) operated at 15 kV was used to study the morphology of the milled powders. A JEOL JEM-2011 transmission electron microscope (TEM) operated at 200 kV was used to examine the nanostructure of the powders and verify the crystal structure using indexed selected area diffraction patterns. The average grain size measurement was carried out using CLEMEX image analysis software on TEM dark field micrographs.

4.3 Results and Discussion

4.3.1 Phase Transformation and grain refinement during Mechanical Alloying

During mechanical alloying, the various powder systems are subjected to severe mechanical deformation and are repeatedly deformed. In the present nSS0Al systems, the

crystal structure of the 316LSS powder exhibited strain induced phase transformation of the austenite (FCC) phase and the volume fraction of FCC crystals is seen to decrease with milling time. Figure 4.1 shows that after 32 hr of milling the FCC structure for the pre-alloyed stainless steel powder has completely disappeared as depicted by the disappearance of the austenite peak from the starting powders. In addition, similar strain induced transformation was observed for the two Al-containing alloys. TEM examinations of the electron diffraction pattern of nSS6Al cryomilled powder shown in Figure 4.2 and analysis of the d-spacing presented in Table 4.1 indicate that the strain induced phase transformation occurring during cryomilling yields a BCC crystal structure. A similar phase transformation from FCC to BCC for 316LSS was reported for ball milled samples [29]. During cryomilling the powders are subjected to high strain deformation and the BCC structure occurs because it is loosely packed and therefore can accommodate the crystal strain more easily than the closed packed FCC structure. The nano-ferrite grain structure formed during the milling process was referred to as a strain-induced-ferrite transformation [29]. Reversion of the BCC to FCC phase transformation was not detected by XRD (Figure 4.1) nor TEM diffraction pattern (Figure 4.2) during milling up to 32 hr and is not expected even with longer time as the process takes place at a cryogenic temperature where the heat of collision is not enough to drive the reverse transformation.

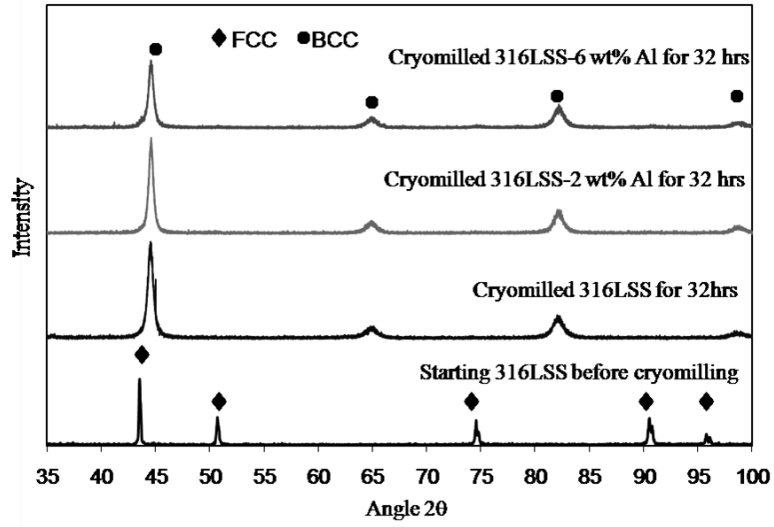


Figure 4.1 X-ray diffraction patterns of as-milled powders.

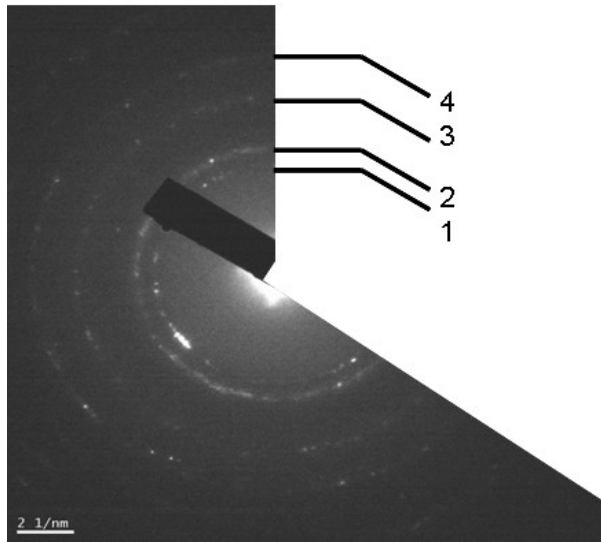


Figure 4.2 TEM electron diffraction pattern of cryomilled nSS6Al after 32 hr of milling, details of the rings are shown in Table 1.

Table 4.1 Interplanar spacing determined from the TEM diffraction pattern of Figure 4.2.

Ring	d-spacing (nm)	α -BCC
1	0.117	{211}
2	0.102	{220}
3	0.076	{321}
4	0.058	{422}

For the Al-containing stainless steel mixtures, signs of alloying were observed after 8 hr while complete alloying was obtained after 32 hr of milling. This was indicated by the disappearance of the Al peaks in the X-ray diffraction spectra, as shown in Figure 4.3 for nSS6Al. Similar solutionizing was observed for the blend containing 2wt.% Al. The average grain sizes calculated using the Scherrer relationship from the respective diffraction patterns (Figure 4.1) after 32 hr of milling are 13 nm for nSS0Al, 21 nm for nSS2Al and 25 nm for nSS6Al. As depicted, an increase in Al content results in an increase of the average grain size. TEM analyses of the three powder systems reveals that the grain structure was indeed in the nano-scale after the completion of milling. A representative TEM dark field micrograph of the as-milled nSS6Al powders and the corresponding grain size distribution are presented in Figure 4.4 (a) and (b), respectively. After examination of over 1100 individual grains, the measured average grain size of the as-milled powders was determined to be 6.7 nm. The grain size distribution is narrow with most of the grains smaller than 10 nm. Both the XRD and the TEM results reveal successful mechanical alloying and grain refinement of the mixtures by cryomilling.

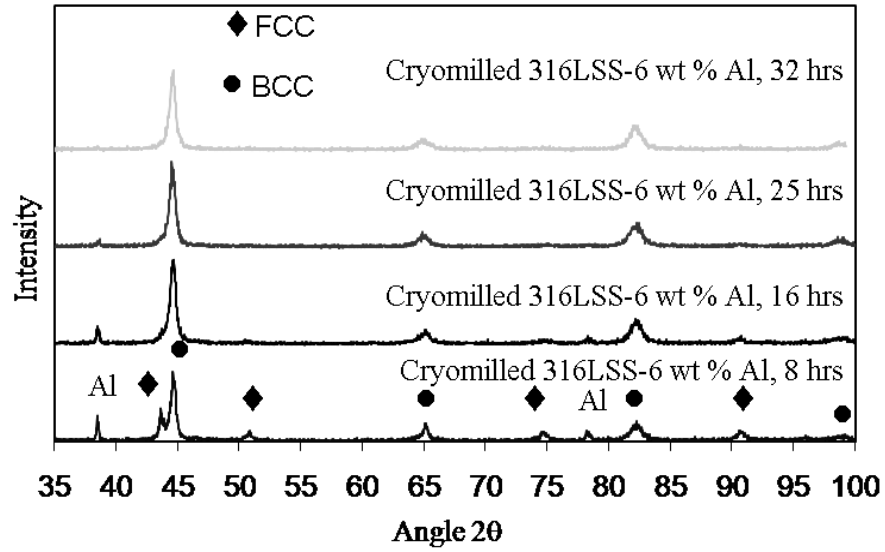


Figure 4.3 XRD spectra of cryomilled nSS6Al for different milling time.

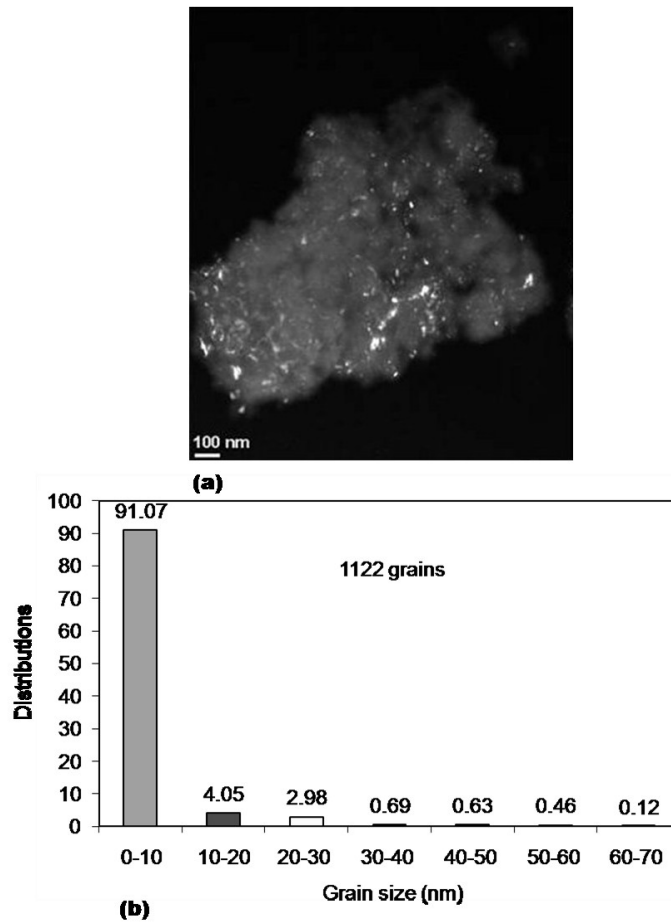
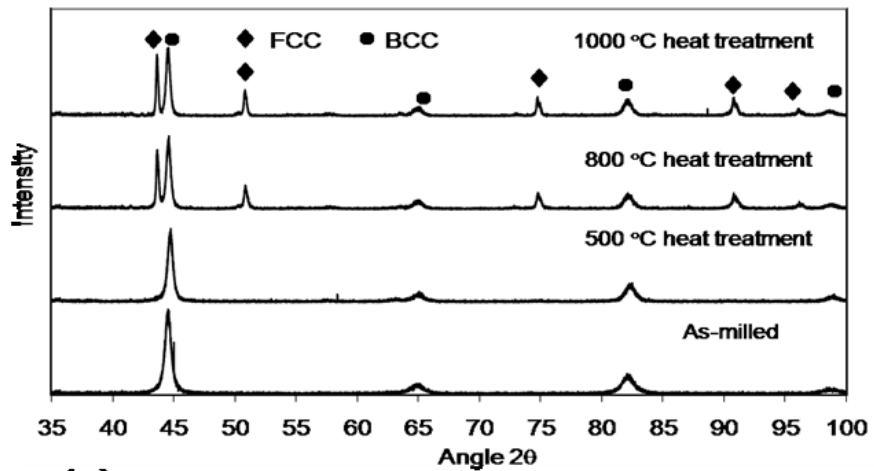


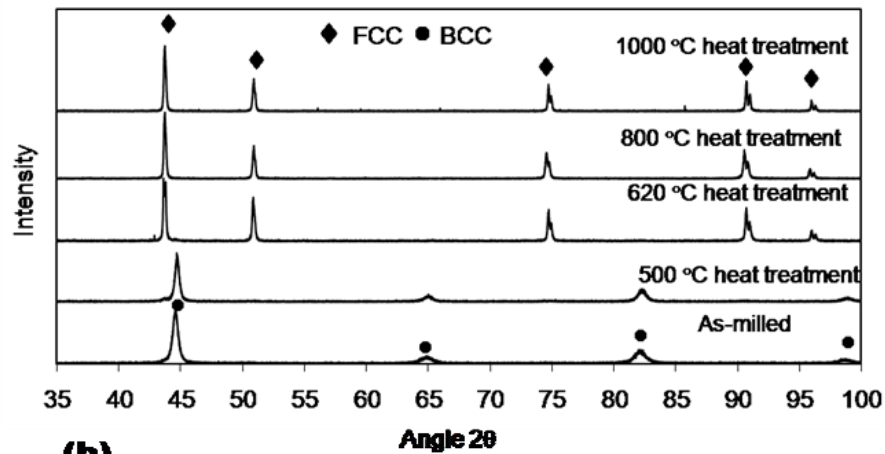
Figure 4.4 (a) Dark field TEM micrograph of nSS6Al nanostructured particle after milling for 32 hr and (b) grain size distribution measured from the TEM micrographs.

4.3.2 Phase Transformation during Heat Treatment

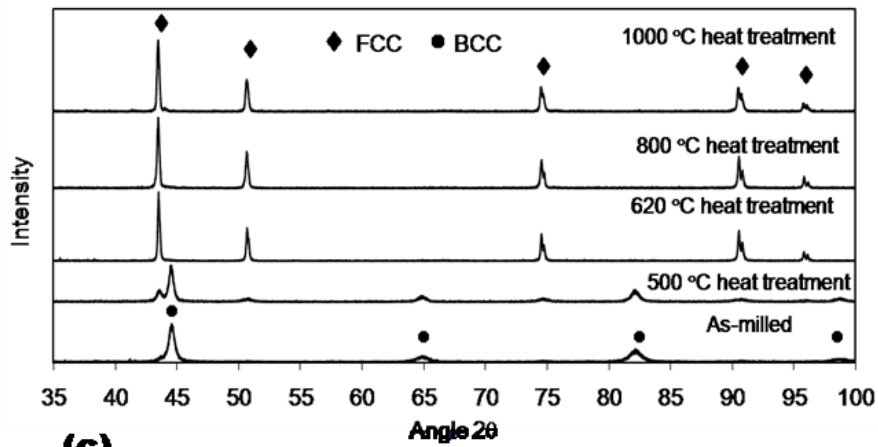
The milled powders were annealed at temperatures of 500 °C, 620 °C, 800 °C and 1000 °C to examine phase and grain size stability at high temperature. Models of thermodynamic, kinetic and magnetic transition reveal that phase transformation and phase stability of austenitic stainless steel are very sensitive to changes in chemical composition and microstructure [78-80]. Indeed, the Al concentration was found to have a strong influence on the reversion of the strain induced transformation during annealing. XRD patterns of nSS0Al, nSS2Al and nSS6Al acquired after a 1 hour hold at different annealing temperatures are presented in Figure 4.5 (a), (b) and (c) , respectively. For the reference system (nSS0Al), the BCC phase was stable at 500 °C, while a fraction of the BCC structure transferred back to FCC at 800 °C and 1000 °C. H. Huang showed in his work total recovery of FCC was achieved at 800 °C for 304 stainless steel powder milled using Sepx mill [34]. The incomplete recovery of the FCC phase in nSS0Al during annealing up to 1000 °C could be due the high density of dislocations caused by cryomilling where no partial recovery occurs during processing. The Spex mill process used by H. Huang allows partial recovery of dislocation during the milling process as the local temperature induced by high energy collisions can be 500 °C [35-36]. Additionally, 316LSS, unlike 304, has 2.2 wt.% molybdenum which is a BCC stabilizing element [81]. The BCC structure has completely reverted to FCC at 620 °C for both Al-containing alloys. Table 4.2 summarizes the quantitative weight percent of FCC reverse transformation after the different annealing treatments for all three systems.



(a)



(b)



(c)

Figure 4.5 XRD patterns of samples annealed at different temperatures (a) nSS0Al (b) nSS2Al (c) nSS6Al.

Table 4.2 FCC weight fraction measured by quantitative XRD after the different annealing treatments for the three alloys.

Annealed temp.	nSS0Al	nSS2Al	nSS6Al
500 °C	0	4	9
620 C	N/A	100	100
800 °C	27	100	100
1000 °C	29	100	100

DSC has been widely used to study the kinetics of phase transformations, precipitations and grain growth in various systems. Details of the thermodynamic values (heat of transformation) and kinetics of phase transformations (start and end temperatures) for the three systems were studied using DSC. The DSC trace for the reference alloy (nSS0Al) measured at 20 K/min showed that the phase transformation started at 605 °C. However, the incomplete nature of the endothermic peak indicate incomplete reversion transformation up to temperature of 1000 °C, which is in agreement with the results obtained by XRD (see Figure 4.5 (a)). Figure 4.6 shows the DSC trace for nSS2Al acquired at a scan rate of 20 K/min. As depicted, the endothermic peak, corresponding to the BCC to FCC transformation is complete, with start and end temperatures of 422 and 605 °C, respectively. The DSC trace for nSS6Al followed similar behavior to the nSS2Al traces, with complete transformation occurring below 600 °C. The DSC results of start and end transformation temperature for the two Al-containing systems are in good agreement with the XRD analysis presented in Figure 4.5 (b) and (c), respectively. Three DSC curves acquired at different scan rates were produced for the Al-containing systems to calculate the alteration in the start and end, and the enthalpies of BCC-to-FCC transformation and the results are presented in Table 4.3 and 4.4, respectively. The

results show an increase in transformation temperature with increasing heating rate (scan rate). This is strong evidence of a diffusion-controlled mechanism for the BCC to FCC phase transformation [82]. In addition, the start and end transformation temperatures for the nSS6Al system are always lower than for the nSS2Al system for the same scan rate, indicating that the Al concentration plays an important role in the crystal structure stability. The calculated transformation enthalpies for the nSS2Al system are approximately similar and within the same order of magnitude to the latent heat of the BCC $\alpha \rightarrow$ FCC γ in pure iron, which is 16 J/g [83]. In addition, the austenite enthalpy of transformation in nSS6Al is slightly lower than for the nSS2Al system, reinforcing the fact that increased Al promotes FCC crystal structure formation upon annealing.

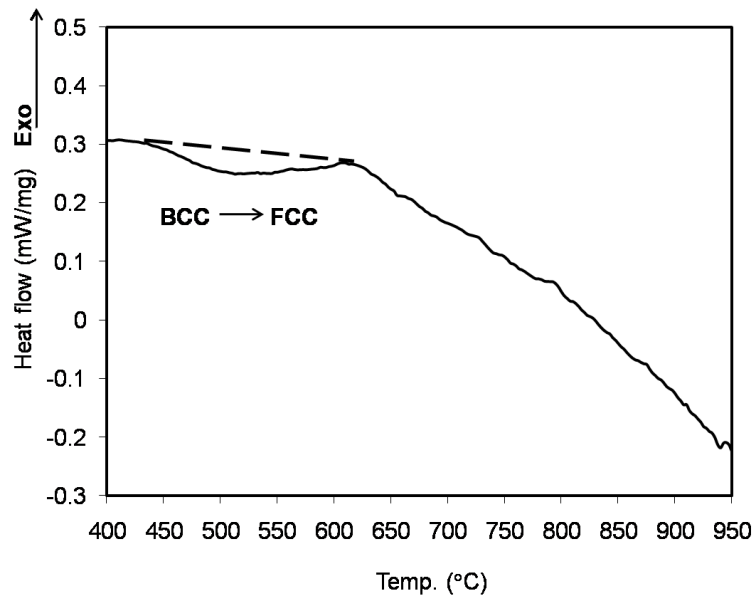


Figure 4.6 DSC trace of nSS2Al heated at 20°C/min

Table 4.3 DSC parameters for nSS2Al austenite transformation.

Heating rate (K/min)	Start temp. (°C)	Peak temp.(°C)	End temp. (°C)	Enthalpy (J/g)
20	422	512	605	-10.5
40	480	538	616	-12.2
45	488	545	618	-7.9

Table 4.4 DSC parameters for nSS6Al austenite transformation.

Heating rate (K/min)	Start temp. (°C)	Peak temp.(°C)	End temp. (°C)	Enthalpy (J/g)
20	415	508	565	-11.4
40	466	522	588	-7.2
45	473	526	594	-6.9

As illustrated, Al enhances the transformation of BCC to FCC during annealing and the drastic effect of adding Al to the stainless steel structure can be observed from a clear cell structure (grain) that is developed for nSS6Al but the cell structure is not clearly developed for nSS0Al. The nSS6Al system shows the crystallography of the grain structure with the interior of the grain with low densities of dislocations. Consideration of this result indicates that dislocations are relatively free to glide across the crystal structure and thus indicate a high Stacking Fault Energy (SFE) for this material. M, Murayama, obtained similar result for 316 austenitic stainless steel free of N [84]. In the study, it was found that nitrogen free stainless steel shows grains almost void of dislocations and was believed that the SFE of this material is high. The glide of perfect dislocations is the dominant deformation mechanism of alloys with SFE values greater than 60 mJ/m^2 [25]. The addition of Al increases the SFE and therefore stabilizes austenite recovery. The stability of austenite is strongly correlated to SFE [26,27].

Schramm and Reed [85] suggest a simple equation to determine the SFE for commercial austenitic stainless steels as follows:

$$\text{SFE} = - 53 + 6.2 (\text{Ni}) + 0.7 (\text{Cr}) + 3.2 (\text{Mn}) + 9.3 (\text{Mo}) \quad (14)$$

Here the SFE is in (mJ/m^2) and the elements are in mass percent. The SFE of 316LSS calculated with Equation 14 is $63 \text{ mJ}/\text{m}^2$. However, at high temperatures the SFE of materials can vary as Latanision found that the SFE of 304L stainless steel increased from $16.4 \text{ mJ}/\text{m}^2$ at $25 \text{ }^\circ\text{C}$ to $30.4 \text{ mJ}/\text{m}^2$ at $325 \text{ }^\circ\text{C}$ [20]. Al has a SFE of $200 \text{ mJ}/\text{m}^2$ [86] and alloying Al with stainless steel should contribute and increase the overall SFE of the stainless steel alloy. It was found that the addition of 12 wt.% of Al to high manganese TWIP steels increases the SFE significantly from $15\text{-}20 \text{ mJ}/\text{m}^2$ to $110 \text{ mJ}/\text{m}^2$ and stabilizes the austenite against the strain-induced transformation [87]. Chemical composition and temperature are the primary factors controlling SFE and, consequently, determining the deformation mechanism for an alloy [21,22]. This could explain the high starting phase transformation temperature ($605 \text{ }^\circ\text{C}$) and slow recovery of austenite for nSS0Al compared to the other alloys due to the absence of the extra driving force which is provided by the presence of Al. On the other hand, fast and full recovery of austenite for nSS2Al and nSS6Al is a result of a combination of annealing temperature and Al addition.

The evolution of the lattice parameters upon annealing was determined by XRD and is summarized in Table 4.5. For the nSS0Al pre-alloyed powder, the lattice parameter in

the as-milled condition was measured to be similar to that of α -Fe (2.8664 Å [88]), which supports the result that strain induced transformation of stainless steel during cryomilling yields a BCC structure. In addition, as shown in Table 4.5, the various heat treatments seemed to have no influence on the lattice parameter of the BCC phase as it remains identical, considering the standard deviation on the measurements. Regarding the FCC phase formed during the heat treatment for the plain nSS0Al system, the lattice parameters are slightly lower than the parameter of the starting material (3.5959 ± 0.0008 Å). For the system containing 6wt.% Al, the BCC phase lattice parameter in the as milled condition is larger than the plain nSS0Al system and is attributed to the presence of Al in the structure. Since the radius of the Al atom at 1.43 Å is bigger than that of the Fe atom at 1.24 Å, the 316LSS BCC crystal volume is expected to increase with Al dissolution in the 316LSS matrix. Upon annealing and beginning of the BCC to FCC phase transformation, the lattice parameter of the remaining BCC phase should decrease to the reference value for the BCC structure and would be associated with a rejection of Al towards the stabilized FCC phase, which reaches the reference value after the heat treatment at 1000 °C. The lattice parameter measurements of the FCC phase strengthen the conclusion that the dissolution of Al into 316LSS stabilizes FCC phase recovery.

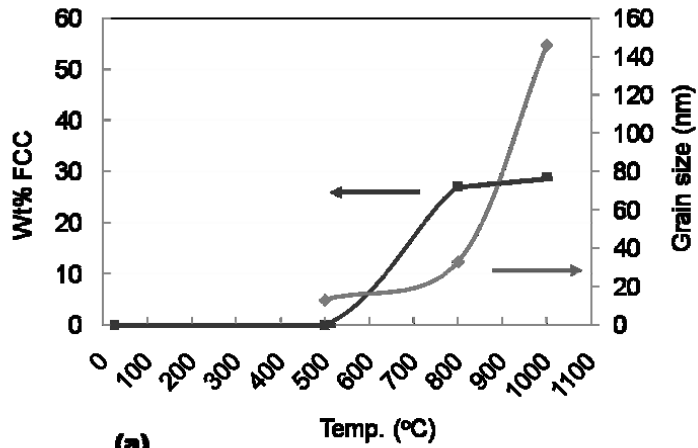
Table 4.5 Lattice parameters (Å) of BCC and FCC phases for 3 nSS0Al and nSS6Al.

Temp.	nSS0Al		nSS6Al	
	BCC	FCC	BCC	FCC
As-milled	2.8651 ± 0.0029		2.8706 ± 0.0025	
500 °C	2.8685 ± 0.0016		2.8659 ± 0.0014	3.5919 ± 0.0007
800 °C	2.8701 ± 0.0016	3.5892 ± 0.0005		3.5929 ± 0.0004
1000 °C	2.8702 ± 0.0022	3.5906 ± 0.0009		3.5951 ± 0.0003

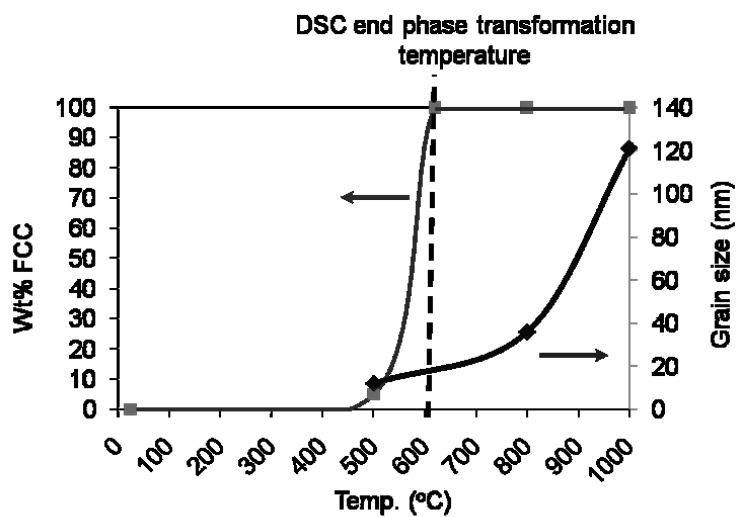
4.3.3 Grain Growth during Heat Treatment

To study the effect of phase transformation on grain growth behavior, the average grain size (measured from TEM micrographs) and the corresponding FCC recovery as a function of various annealing temperatures for 1 hour holding time is plotted in Figures 4.7 (a), (b) and (c) for nSS0Al, nSS2Al and nSS6Al, respectively. The grain growth event for nSS2Al and nSS6Al is occurring after the completion of phase transformation, illustrating that the two thermally activated phenomenon are independent. For the nSS0Al system, there is no clear indication that the phenomena are independent as the austenite recovery was not achieved. Materials with high stacking fault energy may first exhibit full recovery rather than recrystallization, which tends to be the phenomenon observed in the present case.

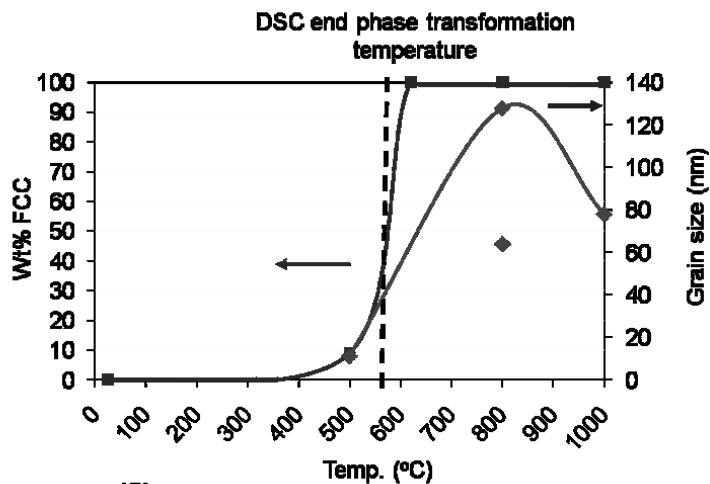
As depicted in Figure 4.7, grain growth occurred during the tested heat treatment schedules. This kinetic process was quantified in terms of activation energy and calculated from the thermal analysis of the DSC curves. Figure 4.8 illustrates the DSC trace of nSS6Al grain growth at 20 K/min scan rate and the exothermic grain growth peak parameters for the nSS6Al are summarized in Table 4.6.



(a)



(b)



(c)

Figure 4.7 FCC wt.% and average grain size as a function of annealing temperature for (a) nSS0Al (b) nSS2Al (c) nSS6Al.

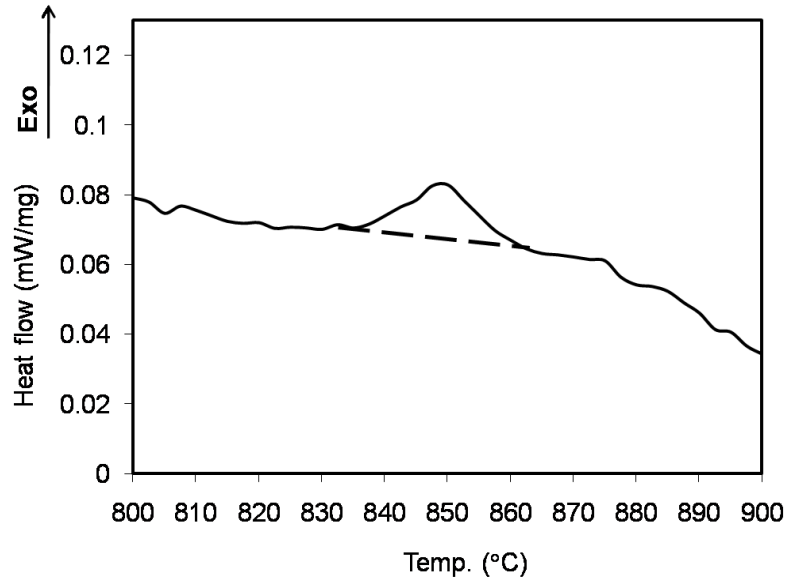


Figure 4.8 DSC trace of nSS6Al exothermic peak heated at 20°C/min.

Table 4.6 DSC parameters for nSS6Al shows grain growth.

Heating rate (K/min)	Start temp. (°C)	Peak temp.(°C)	End temp. (°C)
20	838	849	861
40	846	872	887
45	850	876	893

The phase transformation and grain growth activation energy for this system was estimated, based on the DSC curves using a modified Kissinger method [89,90], as shown in equation 15:

$$\ln \frac{T^2}{\phi} = \frac{E}{RT} + \ln \frac{E}{RK} + \ln \beta \quad (15)$$

where T is the characteristic temperature for a given process, ϕ the heating rate, E the activation energy, R the gas constant and K and β are constants. The activation energy, E

is obtained from the slope of a linear plot of $\ln(T^2/\phi)$ versus $1/RT$ peak temperatures at the three different heating rates. Figure 4.9 (a) and (b) illustrate the Arrhenius relation and the calculated activation energy, E , are 90 kJ/mol and 126 kJ/mol, for reverse transformation and grain growth of the nSS6Al system, respectively.

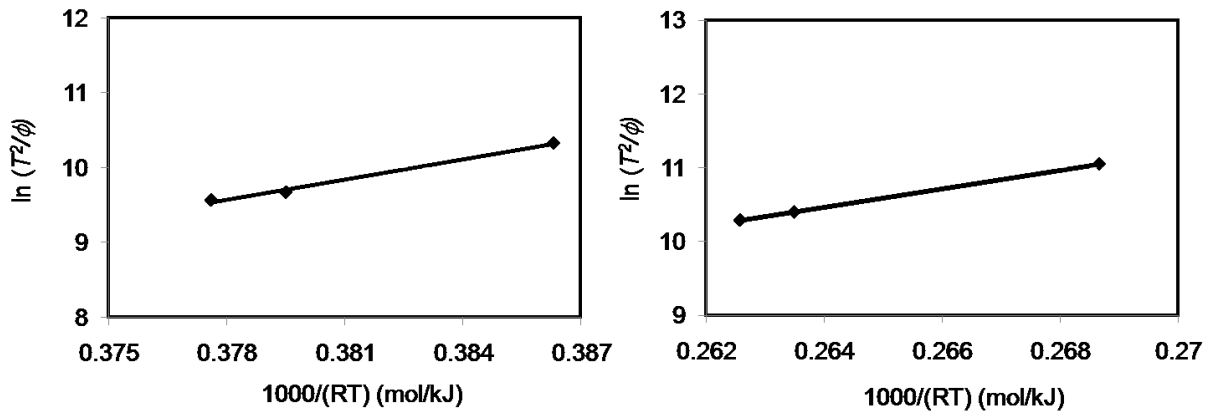


Figure 4.9 Arrhenius type of plot to determine the activation energy of nSS6Al, (a) phase transformation (b) grain growth.

The activation energy of phase transformation is lower than the grain growth which is an indication of the two phenomena are independent and that phase transformation happens before grain growth. The rearrangement of the dislocations in the early stage should provide the activation energy necessary to initiate the BCC to FCC transformation.

4.3.4 Influence of Precipitations and Heat Treatment Duration on the Grain Growth Behavior

During grain growth of cryomilled materials, two phenomenon are in competition, regular grain growth and a pinning effect provided by nano-precipitates which retards the grain growth phenomenon. To study the possible formation of pinning phases and their influence on grain growth, heat treatments without hold were performed for the nSS6Al at the same temperature and the results are shown in Figure 4.7 (c). At 800 °C the average grain size was 64 nm while it doubled (128 nm) for samples held at 800 °C for one hour. Figure 4.10 shows two TEM micrographs comparing the microstructure for these two samples. At a certain annealing temperature, grain growth for cryomilled powders shows a rapid increase in grain size for time intervals up to 1 hour followed by slow grain coarsening for time intervals beyond 1 hour holding time [91]. For example, the original average grain size of as cryomilled Inconel 625 was around 15 nm followed by grain growth to around 145 nm when the sample was heated at 700 °C for 1 hour and around 155 nm for 4 hour annealing at the same temperature [91].

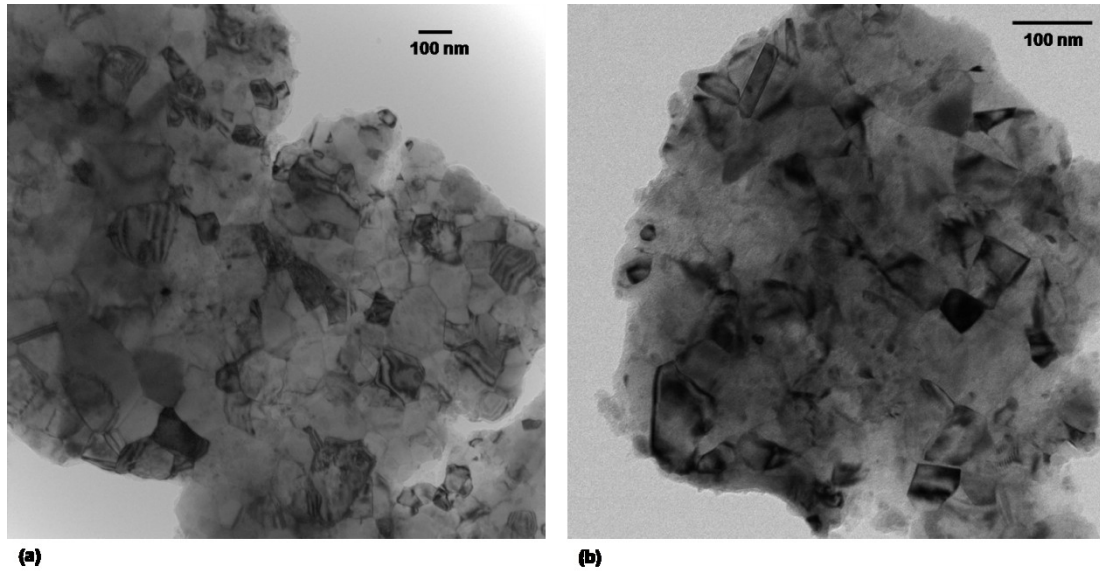


Figure 4.10 (a) TEM micrograph of nSS6Al heat treated at 800 °C for 1 hour . (b) TEM of nSS6Al heat treated at 800 °C for no holding time.

Oxygen and nitrogen uptake during cryomilling greatly influence how new particles form during the synthesis of Al-alloyed stainless steel. Cryomilling of Inconel 625, Al and its alloys in liquid nitrogen has been reported to result in the in-situ formation oxy- nitride particles which impede grain growth at high temperature [17, 91]. In particular, they reported a similar uncharacteristic grain growth behavior, where larger grain size was obtained after a soaking at lower temperature. It was found that the grain size of the cryomilled Inconel 625 heat treated at 900 °C (140 nm) is lower than that of cryomilled Inconel 625 heat treated at 800 °C (240 nm). It is suggested that NbC and Ni₃Nb formed during cryomilling and precipitated at the grain boundaries when the sample was heat treated at 900 °C, these particles are likely to be responsible for the large degree of thermal stability that observed at 900 °C [91]. TEM analysis was used to verify if this phenomenon is occurring in the samples used for this study. Figure 4.11 is the TEM

selected area diffraction pattern of nSS6Al powder annealed at 500 °C. The selected area diffraction shows numerous ring patterns, which are indexed to the phases presented in Table 4.7. The diffraction pattern indicates the phase transformation from BCC to FCC, which was previously observed by XRD and DSC however, the point of interest is the possible formation of secondary phases. These phases could have occurred during the cryomilling itself, or could have formed through thermal diffusion during the heat treatment. The interplanar spacing could be associated to the following phases, which are all thermodynamically stable oxides or nitrides: γ -Al₂O₃ ($\Delta H_f = -1611$ kJ/mol), Cr₂O₃ ($\Delta H_f = -1330$ kJ/mol), magnetite iron oxide, Fe₃O₄ ($\Delta H_f = -1121$ kJ/mol) and Al nitride, AlN ($\Delta H_f = -1118$ kJ/mol). These possible particles detected by TEM were not observed by XRD due to the small volume fractions.

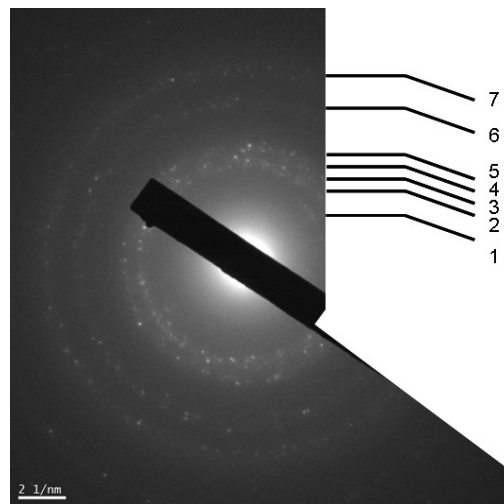


Figure 4.11 TEM electron diffraction pattern of nSS6Al heat treated at 500 °C, details of the rings are shown in Table 6.

Table 4.7 Interplanar spacing determined by TEM diffraction pattern of Figure 4.11.

Ring	d-spacing (nm)	α -BCC	γ -FCC	γ -Al ₂ O ₃	Cr ₂ O ₃	AlN	Fe ₃ O ₄
1	0.140	{200}		{440}		{103}	{442}
2	0.117	{211}			{128}		{551}
3	0.108		{311}		{315}		
4	0.102	{220}	{222}	{731}		{210}	
5	0.098			{800}			
6	0.079		{420}				
7	0.058	{422}					

The results of the present study suggest that the particles formed during cryomilling or in-situ during the thermal treatment and are believed to have insignificant effect on grain size stability during annealing at various temperatures. The grain size stability for the three alloys was below 800 °C where the energy supplied by temperatures might be too low to activate significant grain growth. Similar results were found for austenitic stainless steel 304 for which the grain refinement was done by multiple and multi-axial compressions [92] where no particles were expected to form during grain refinement. Upon annealing the 304 stainless steel at a temperature up to 700 °C, the average grain size did not change remarkably but for temperatures higher than 700 °C, a rapid grain coarsening took place [92]. For this system the grain growth was around 3 times greater than the original size when the alloy was heated to 700 °C and around 20 times greater when the alloy was heated to 900 °C [92]. The nSS0Al and nSS2Al systems showed 3 to 4 times greater grain size than the starting grain size when the two alloys heated to 800 °C and around 12 to 15 times greater grain size when they were heated to 1000 °C. At 800 °C, only the system containing 6 wt.% Al exhibited significant grain coarsening, suggesting that the addition of Al reduces thermal stability of grains. The rather

unremarkable effects of these particles on grain growth retardation in the three alloyed powders could be due to the small volume fractions of these particles such that the pinning effect is far less than the energy provided by the temperature above around 800 °C.

Figure 4.12 illustrates a close up of the region near the (111) reflection of a XRD pattern acquired with slow scan conditions for the system containing 6 wt.% Al heat treated at 1000 °C for one hour. A broad, low intensity peak can be observed and could be associated with an α -Al₂O₃ reflection of the (111) plane. The presence of this phase could arise from the transformation of the γ -Al₂O₃ precipitates to the more stable phase α -Al₂O₃ ($\Delta H_f = -1676$ kJ/mol) during the heat treatment. However, a secondary phenomenon, such as growth of the precipitates to a size and volume fraction detectable through XRD might be occurring but no analysis could be performed to discriminate these events. Generally the phase transition of γ -Al₂O₃ to α -Al₂O₃ occur at temperatures above 1000 to 1250 °C [93-95], however, previous work by Stociek has shown that mechanical milling can lead to transformation into α -Al₂O₃ at temperatures as low as 1000 °C [95]. The lower grain size for the system containing 6 wt.% Al when directly heat treated at 1000 °C could be associated with the improved efficiency of the α -Al₂O₃ to reduce grain boundary mobility and thus retard grain growth. When compared with the sample heat treated at 800 °C, the phase transition as well as the possible evolution (phase transformation and possible growth) can be responsible for the improved grain stability.

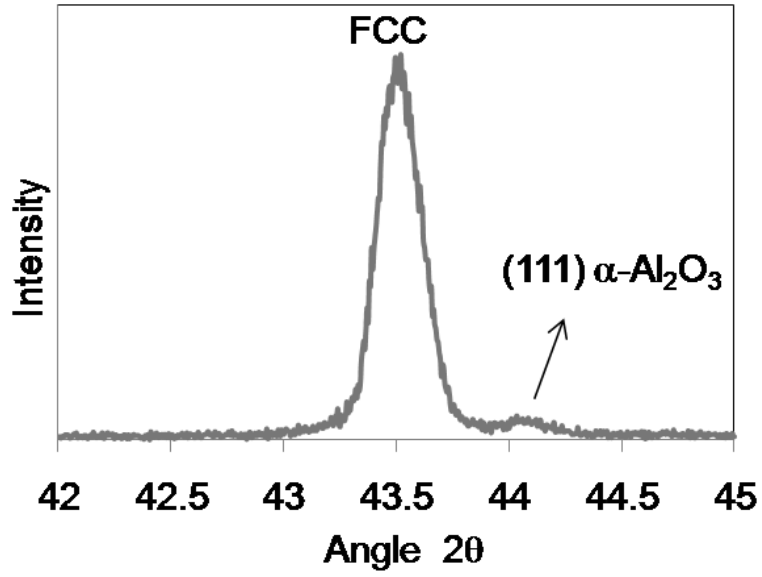


Figure 4.12 XRD spectra of nSS6Al annealed at 1000 °C.

4.4 Conclusions

Cryomilling and annealing behavior of milled nSS0Al, nSS2Al and nSS6Al powders were studied at various annealing temperatures. The main results can be summarized as follows:

1. Cryomilling of the three alloys results in a strain induced BCC transformation and the evolution of nanocrystalline grain structure. Mechanical alloying of Al at 2 and 6 wt.% percentage containing in 316LSS was successfully achieved after 32 hr of cryomilling.
2. The degree of the FCC recovery from the induced BCC structure during annealing at various temperatures differs for all three alloys. Complete recovery of the FCC

phase was achieved between 565 and 594 °C for nSS6Al and 605 to 618 °C for nSS2Al, depending on the heating rate. Heat treatment up to 1000 °C for the nSS0Al results in incomplete recovery of FCC.

3. Al enhances the transformation of BCC to FCC during annealing and the weight fraction transformed to FCC increases as the concentration of Al increases. The addition of Al increases in the overall SFE of the alloy, which results in faster austenite recovery.
4. Annealing at different temperatures is accompanied by grain growth. The results indicate that the phase transformation and grain growth are independent phenomenon. Complete phase transformation in nSS2Al and nSS6Al was achieved before the major grain growth. In nSS0Al the main grain growth took place at annealing temperature with incomplete austenite recovery.
5. Particles formed during cryomilling and their precipitation is believed to have insignificant effect on pinning grain boundaries and retarding grain growth during annealing. The activation energy of phase recovery and grain growth for nSS6Al was calculated and was found to be 90 kJ/mol and 126 kJ/mol, respectively.

5. MICROSTRUCTURE AND TRANSFORMATION OF AL-CONTAINING NANOSTRUCTURED 316L STAINLESS STEELS DURING SPARK PLASMA SINTERING

5.1 Introduction

Austenitic stainless steels provide excellent resistance to corrosion and oxidation and are applied widely throughout various industries. Improvements in the chemical composition and modification of the grain size can provide enhanced resistance to corrosion and oxidation. Almathami et al. [96] have shown an improvement in the oxidation resistance for SS316L powders when a combination of grain refinement and alloying with 6 wt% Al is employed [96]. For the tested temperatures of 500, 800 and 1000 °C, the nanocrystalline nSS6Al powders showed lower weight gain and better oxidation properties than conventional 316LSS powders. At 500 °C and 800 °C the weight gain of the nanostructured powders was almost half that of the micron-sized powders while the weight gain was seven times lower for the nanocrystalline SS6Al powder tested at 1000 °C [96]. Due to the smaller grain size and increased number of diffusion paths, the formation of the protective α -Al₂O₃ scale at elevated temperatures in nano-grained Al-containing alloys occurs at lower Al concentrations than for steels with micron-sized grains [5, 74, 96].

Mechanical milling is the process of choice for the fabrication of alloyed powders [97] due to the variability of the processing parameters. The severe deformation that occurs during mechanical milling of austenitic stainless steel causes a strain induced phase transformation, the exact nature of which is currently under debate within the scientific community as contradictory results regarding the resulting crystal structure have been advanced by different researchers [29,30]. Work done by Fujiwara et al. [29] on 316L stainless steel powder showed, by the usage of TEM and XRD techniques, that the strain induced transformation changes the crystal structure from face centered cubic (FCC) to body centered cubic (BCC) during mechanical milling (Fujiwara et al., 2001). In contrast, Szymanska et al. [30] showed that for the same alloy, using the Mossbauer technique, the transformation of the initial FCC structure yields a BCT martensite structure in the milled powder. Almathami et al. [98] have demonstrated that mechanical milling indeed produces a BCC structure and that the presence of Al promotes reversion to the FCC crystal structure during conventional heat treatments [98]. The thermally sensitive BCC crystal structure thus requires a rapid processing route to maintain the BCC structure upon consolidation which is desirable for the improved oxidation resistance of the nanostructured alloy. This is illustrated by Baustista et al. who found that for conventional stainless steel systems, a BCC 434L steel was more resistant to high temperature oxidation than a FCC 316L steel, where both alloys had similar Cr content [99]. The study showed that the BCC steel tended to develop a superior Cr_2O_3 scale while the FCC stainless steel tended to form a less protective $(\text{Fe,Cr})_2\text{O}_3$ oxide.

SPS process has recently received significant attention due to the rapid consolidation time (minutes), which reduces grain growth or undesirable reactions, and the ability to sinter challenging materials like nanostructured powders, [38-40]. In one study of nanocrystalline ferritic 430L stainless steel prepared by high-energy ball milling (HEBM) and SPS [41] the consolidated powders showed higher strength and hardness than conventional 430L stainless steel. Unfortunately, no work relating the sintering of either nanostructured austenitic stainless steel powders or stainless steel powders containing Al was found in the literature.

The present study explores the consolidation behavior of Al-containing 316L stainless steel produced by cryomilling using SPS. Three alloys were studied: nSS0Al and 316L stainless steel containing 2 and 6 wt% Al. In particular, the evolution of the microstructure, including the reversion of the strain induced phase transformation, and mechanical properties were studied and compared to powders subjected to conventional heat treatment processes.

5.2 Experimental

Austenitic stainless steel powder of grade 316L (17 wt% Cr, 13.5 wt% Ni, 2.2 wt% Mo, 0.14 wt% Mn, 0.81 wt% Si, 0.02 wt% C, balance Fe) supplied by North American Hoganas was used as the starting material. The powder was alloyed with elemental Al powder supplied by Atlantic Equipment Engineers to achieve 316L stainless steel alloys

with 2 and 6 wt% Al. The following acronyms: SS0Al, SS2Al and SS6Al are used herein to identify the stainless steel alloys containing 0, 2 and 6 wt% Al, respectively. Figure 5.1 presents a micrograph of the mixture of the starting powders: stainless steel 316L (-100 mesh; irregular particles) and Al (-325 mesh spherical particles). The cryomilling process was performed in a Union Process HD-01 attritor to concurrently alloy the powders and to refine the grain size to the nanometer scale. The level of liquid nitrogen was monitored by thermocouples to guarantee complete immersion of the powders at all times. The rotation speed was kept constant at 220 RPM and the powders were milled for 32 hr. A powder-to-ball weight ratio of 1:20 was used. The particle size distributions of the cryomilled powders were determined by laser scattering particle size distribution technique using an Horiba LA-920 instrument.



Figure 5.1 SEM image of stainless steel 316L and Al mixed powders, before cryomilling.

The three compositions of milled powders were consolidated using a Dr. Sinter SPS press (model 515-S) in a vacuum environment at 950 °C in a graphite mold. The sintered sample configuration represented a clad surface, i.e. the nanostructured powders were sintered onto conventional stainless steel substrates, mimicking a coating. The heating rate was 95 °C/min up to the sintering temperature and a holding time of 2 minutes was used. To study phase stability the cryomilled powders were also heat treated in a tubular furnace under vacuum at 800 °C and 1000 °C using heating a rate of 10 °C/min and holding times of 2 minutes and 1 hour.

The milled, heat treated powders and SPS samples were characterized by means of X-Ray Diffraction (XRD) in a Philips PW 1710 diffractometer using CuK_α radiation at 40 kV and 20 mA. A scan rate of $0.01^\circ 2\theta/\text{sec}$ was used to allow for calculation of grain size through peak broadening and phases identification. The scanned angle was 40° to $100^\circ 2\theta$. Quantitative analysis of the phases (FCC and BCC) was conducted using XRD patterns based on relative peak intensity for that phase as a function of phase concentration in the alloy [77]. A calibration curve of BCC to FCC intensity ratio was produced using different mixtures of known composition so that the weight fraction of BCC and FCC phases at the different annealing temperatures could be accurately inferred. An optical microscope and a JEOL JSM-840A scanning electron microscope (SEM) operated at 20 kV were used to study the morphology of the milled powders and SPS samples. SPS coatings porosity and average grain size measurements were carried out using CLEMEX image analysis software. Hardness of the consolidated samples was

measured using a microhardness tester from Sun-Tec Corporation (CM-100 AT) with a 300 g load. The reported values are an average of 10 indents.

5.3 Results and Discussion

5.3.1 Cryomilling and Microstructure Evolution of the SPS Consolidated Coatings

Cryomilling caused severe plastic deformation of the starting powders which lead to strain induced phase transformation of the FCC crystal structure. Lattice parameters and selected diffraction patterns of the cryomilled powder acquired via TEM indicate that the strain induced phase transformation yields a BCC crystal structure (Almathami et al., 2010), supporting the results obtained by Fujiwara et al. [29]. The evolution of the crystal structure during milling evaluated by XRD for SS0Al and nSS6Al is presented in Figure 5.2 (a) and (b), respectively. Figure 5.3 shows the corresponding BCC weight percentage as a function of milling time. As indicated in Figure 5.3, the nSS6Al system shows higher wt.% of BCC crystal than the nSS0Al system in the first 6 hr of milling. After 6 hr of milling, the BCC transformation kinetics are slowed down in the nSS6Al system compared to nSS0Al, for which complete phase transformation of FCC to BCC was achieved after 16 hr of milling. For the nSS6Al system, complete transformation was obtained after 25 hr. Prior to milling, the nSS6Al system is a blend of particles with substantial variation in particles size and morphology. During the early stage of

deformation, mechanical mixing of the powder may favor the formation of agglomerates due to the high plasticity of the Al particles. On the other hand, the nSS0Al system has uniform powder morphology and narrow particles size distribution, which may reduce the deformation energy absorbed by the particles. After 6 hr of milling, the particle size distribution and morphology is believed to be similar, which explains the similar kinetics for strain induced phase transformation found in both powders.

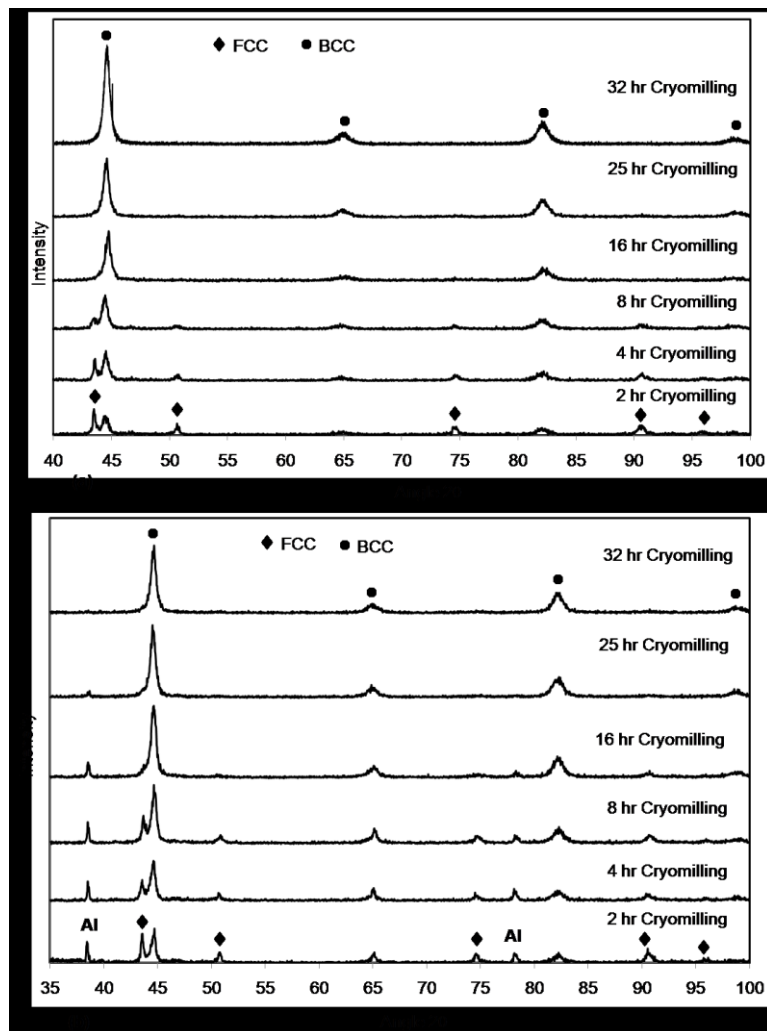


Figure 5.2 XRD patterns of powders at different cryomilling times (a) nSS0Al and (b) nSS6Al.

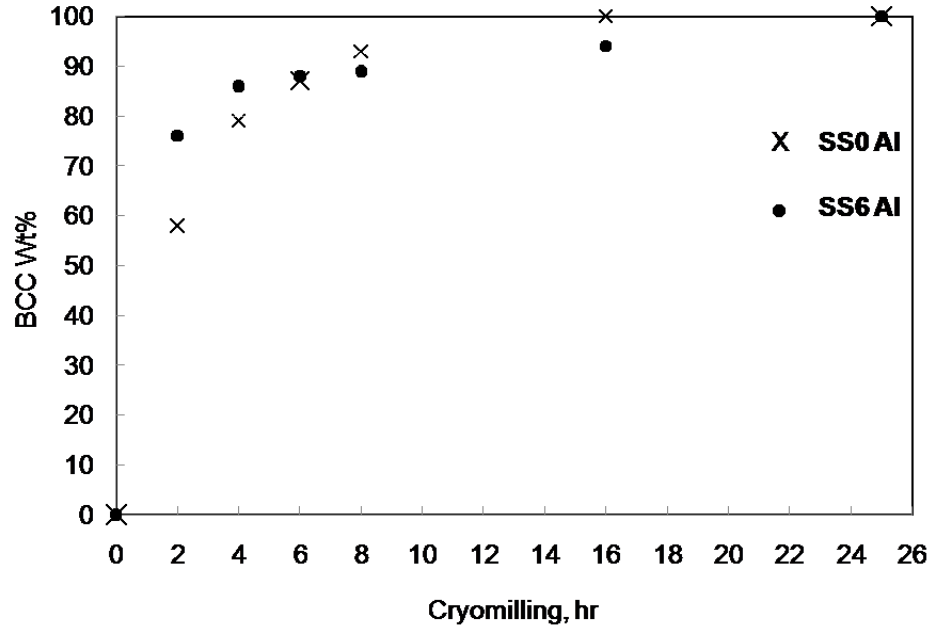


Figure 5.3 BCC wt.% as a function of milling time for nSS0Al and nSS6Al.

Complete alloying was obtained after 25 hr of milling for the two Al-containing stainless steel mixtures. This was indicated by disappearance of the Al peaks in the X-ray diffraction spectra. The average grain sizes calculated using the Scherer relationship from the respective diffraction patterns after 32 hr of milling are 13 nm for nSS0Al, 21 nm for nSS2Al and 25 nm for nSS6Al. The average grain size of SS6Al cryomilled powders was verified by TEM and was found to be 6.7 nm [96].

Figure 5.4 shows the powders particles size distribution of nSS0Al, nSS2Al, and nSS6Al after milling for 32 hr. The average cryomilled particle size increases as the alloyed Al concentration is increased. Several studies found that processing aluminum-alumina dispersion-strengthened alloys required the addition of an organic compound to reduce excessive cold welding of the Al powder particles (bigger particles size) by modifying the

partially exposed metallic surfaces [11, 100, 101]. Al possesses an FCC structure and is a soft material that would be more likely to cold weld than fracturing during milling, which could explain the presence of larger agglomerates in the work presented herein.

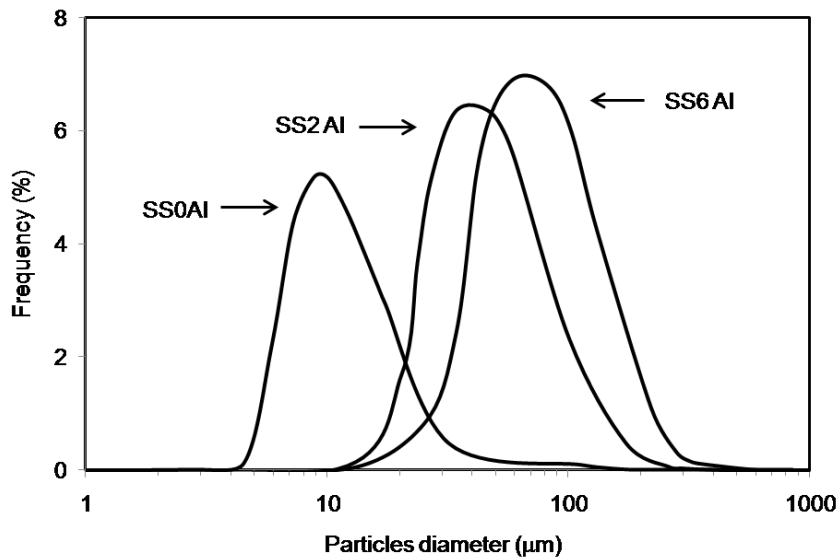


Figure 5.4 Particles size distribution of cryomilled powders.

Cross-sections of nSS0Al, nSS2Al, and nSS6Al SPS consolidated coatings on SS316L substrates are shown in Figure 5.5 (a), (b) and (c), respectively. The three SPS coatings have different cross-sectional morphology, which is explained by the difference in particles size and morphology resulting from the cryomilling process. The nSS0Al coating is formed from smaller cryomilled particles with some larger particles scattered throughout the structure, while the nSS2Al and nSS6Al show lamellar morphology. Porosity levels of 0.79 %, 1.17 % and 2.52 % for the nSS0Al, nSS2Al, and nSS6Al consolidated coatings respectively, was measured using image analysis. The higher

porosity of nSS6Al coating is caused the higher aspect ratio of the flakes resulting from cryomilling.

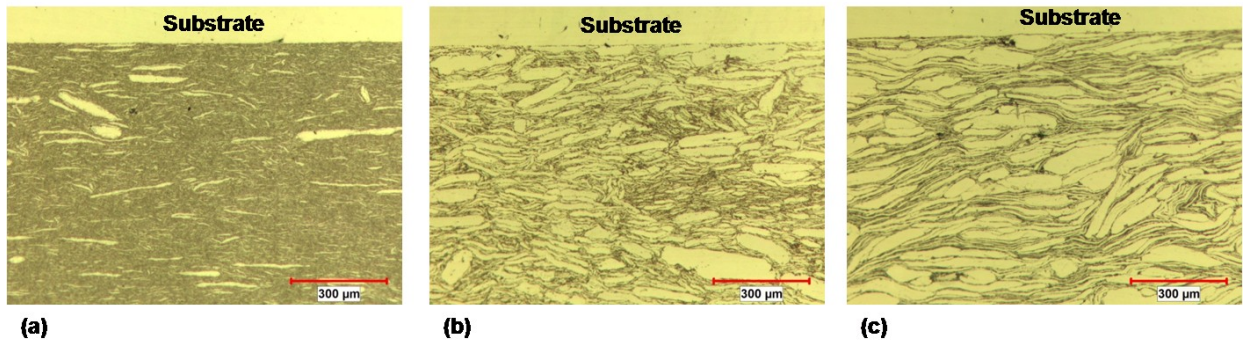


Figure 5.5 Optical cross-sections of (a) nSS0Al, (b) nSS2Al, (c) nSS6Al depicting SPS coating morphology.

5.3.2 Phase Transformation and Grain Growth During SPS and Comparison to Heat Treatment

The SPS process is known to cause rapid consolidation of metastable powders, thus minimizing undesired reactions. The level of crystal structure reversion and grain growth occurring during SPS was compared to the behavior exhibited by milled powders annealed at temperatures of 800 °C and 1000 °C for two minutes and one hour. Figure 5.6 (a), (b) and (c) present the XRD patterns for the nSS0Al, nSS2Al and nSS6Al systems, respectively. Each Figure is composed of a series of spectra acquired from the starting materials, annealing heat treatments and the coatings. Also, Table 5.1 summarizes the corresponding FCC weight percentage calculated for the various heat treatments imposed on the nanostructured powders. In the nSS0Al system, the complete BCC crystal structure

was maintained through spark-plasma sintering, while the metastable BCC crystal structure partially reverted back to FCC in the conventional heat treatments. The powder heat treated at 800 °C possessed a microstructure composed of 26% FCC while the heat treatment at 1000 °C caused 29% of the crystal structure to revert to FCC. Soak time at these heat treatment temperatures seems to have no influence on the amount of microstructure reversion. For both Al-containing alloys, the BCC structure was completely transformed back to FCC after both heat treatments. On the other hand, samples consolidated by SPS retained some BCC grains. The nSS2Al contained 7% while the nSS6Al system contained 32% FCC, reverted from BCC.

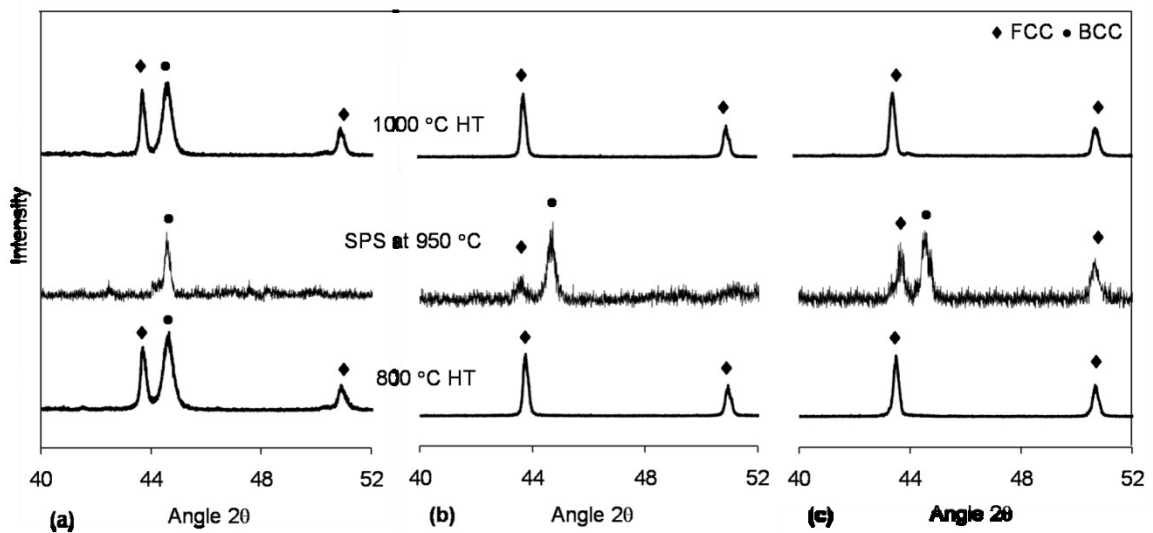


Figure 5.6 XRD patterns of SPS coatings compared to heat treated samples (a) nSS0Al, (b) nSS2Al, (c) nSS6Al.

Table 5.1 FCC wt.% measured by quantitative XRD for SPS coatings and heat treated samples

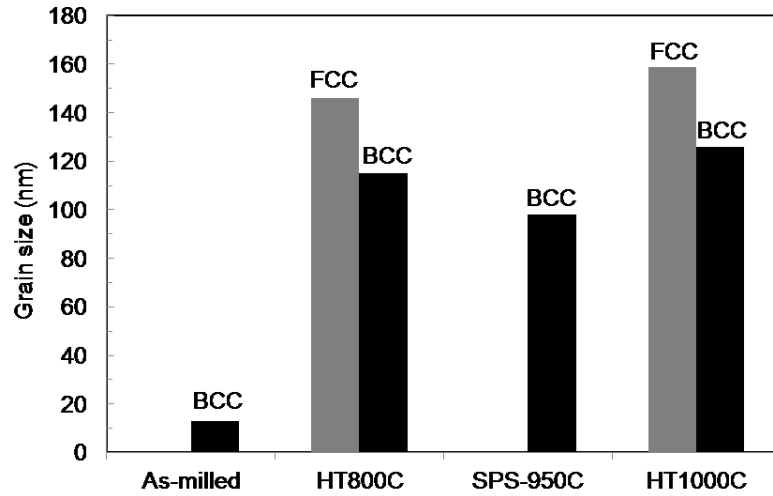
Process	nSS0Al	nSS2Al	nSS6Al
HT 800 °C, 2 min	26	100	100
HT 800 °C, 1 hour	27	100	100
HT 1000 °C, 2min	29	100	100
HT 1000 °C, 1 hour	29	100	100
SPS, 950 °C, 2 min	0	7	32

The analysis of the XRD spectrum results suggests that the SPS process has a limited effect on the FCC transformation when compared to the two tested conventional heat treatments. The thermal load imposed by the SPS process, was not sufficient to provide the activation energy necessary to initiate the crystal structure reversion. Rohatgi [25] suggested that phase transformation resulting from the glide of dislocations across the crystal structure for grains nearly void of dislocations, is the dominant transformation mechanism for alloys possessing Stacking Fault Energy (SFE) values greater than 60 mJ/m². In addition, several studies have shown that the recovery of the FCC structure from BCC structure is strongly correlated with high SFE values [26,27]. Moreover, the SFE is also influenced by the composition of the alloy and the temperature [21]. Schramm and Reed [85] suggested a simple equation to determine the SFE for commercial austenitic stainless steels, and the SFE calculated for the starting 316LSS used in this study is 63 mJ/m², suggesting that the BCC-to-FCC phase transformation mechanism occurs through the displacement of the dislocations across the BCC grains. Unfortunately, no literature data was found on the distribution of dislocations in nanostructured strain induced 316L system. For the nanostructured BCC 430L SS system consolidated by SPS at 900 °C, Hong-wei et al. have demonstrated that a sintering time

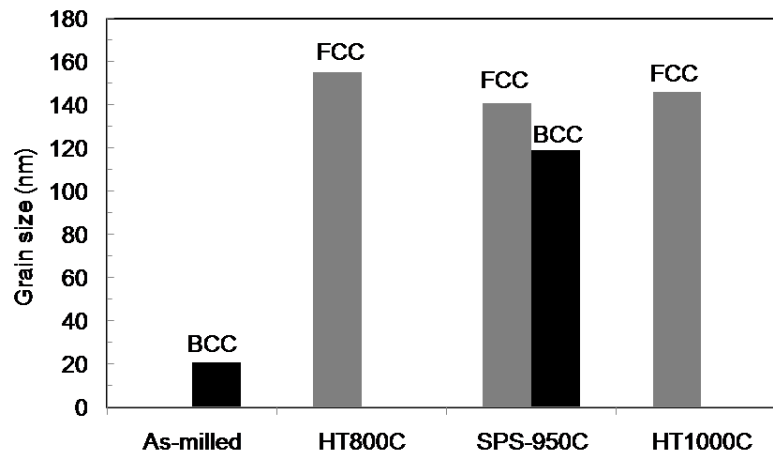
of minimum 10 minutes was required to observe a change in dislocation density [41]. The results from the work by Hong-wei et al. would possibly explain the retention of the BCC structure after the SPS consolidation observed in this work, and could also be associated with the reduced mobility of the dislocation in nanostructured BCC crystals. In addition, as illustrated from the XRD patterns presented in Figure 5.6 and the summary presented in Table 5.1, the Al concentration was found to have a strong influence on the reversion of the strain induced transformation for both the SPS process and the conventional heat treatments. The SFE of Al is 200 mJ/m^2 [86] and alloying Al with the stainless steel should contribute to an increase of the overall SFE for the Al-containing alloys (nSS2Al and nSS6Al). In another steel system, an increase of SFE was observed for TWIP steels, where the addition of 12 wt% of Al increased the SFE from $15\text{-}20 \text{ mJ/m}^2$ to 110 mJ/m^2 and stabilized the austenite structure against the strain-induced transformation [87]. Similar increase of the SFE for the Al-containing stainless steel studied in the present work should be expected, which should further facilitate the BCC→FCC phase transformation.

Figure 5.7 presents the average grain size measured by XRD for the SPS consolidated coatings and powder samples subjected to heat treatments at $800 \text{ }^\circ\text{C}$ and $1000 \text{ }^\circ\text{C}$. The results in Figure 5.7 (a), (b) and (c) correspond to the SS0Al, nSS2Al and nSS6Al systems, respectively. For the nSS0Al system, both the conventional heat treatments and the SPS consolidation induced grain growth. The crystal structure and grain size of the feedstock was BCC and 13nm , respectively. Both heat treatments caused grain growth combined with crystal structure reversion, where the grain size for the heat treatment

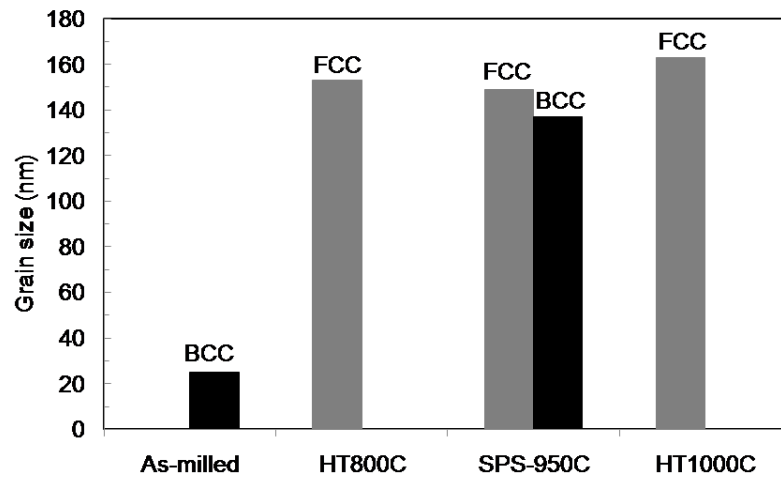
performed at 800 °C was 115nm and 146nm for the BCC and FCC crystal structure, respectively. Similarly, a calculated grain size value of 126nm for the BCC crystals and 159nm for the FCC crystals was obtained for the powders heat treated at 1000°C. Interestingly, the SPS consolidation for the nSS0Al induced grain growth (98nm), but did not cause crystal structure transformation. For the nSS2Al system, the grain size for the original feedstock was 21nm. Grain growth combined with the complete crystal structure transformation occurred (see Figure 5.6) for the two heat treatments, where at 800°C, the FCC structure had a grain size of 155nm while the samples heat treated at 1000°C exhibited a grain size of 146nm. For the SPS consolidated sample, the crystal structure transformation was incomplete (see Figure 5.6). The grain size for the BCC structure was 119nm and 141nm for the FCC structure. Similarly for the nSS6Al, complete crystal structure transformation occurred for the heat treated samples, while only a partial transformation was observed for the SPS sample. The feedstock had a starting grain size of 25nm with a BCC structure. For the two heat treatments, the microstructure was composed solely of FCC crystals and had a grain sizes of 153nm (heat treatment at 800°C) and 163nm (heat treatment at 1000°C). For the SPS sample, the BCC crystals had a grain size of 137nm while the FCC crystals had a grain size of 149nm. These results indicate that the SPS process imposed a lower thermal load on the samples than the two heat treatments, resulting in smaller grain size and incomplete phase transformation during the consolidation.



(a)



(b)



(c)

Figure 5.7 Average grain size of SPS consolidated powders compared to heat treated powders (a) nSS0Al, (b) nSS2Al, (c) nSS6Al.

The results obtained from the comparison of the grain size evolution as a function of the heat treatment imposed for the three systems suggests the following sequence of events. During milling, a strain induced transformation is occurring, in which the equilibrium FCC crystal structure transforms into the metastable BCC structure. In addition, the grain size is reduced to the vicinity of 10nm. During heating, two phenomenons are competing, grain growth of the nanostructure and the crystal structure reversion, which is driven by the SFE. From the nSS0Al results (lowest SFE of the three systems studied), it is suggested that the first event occurring is the growth of the BCC crystals up to approximately 100-110nm, followed by the crystal structure transformation towards the equilibrium FCC structure, which is then followed by further grain growth. To validate this hypothesis, a heat treatment of the nSS0Al powders was performed at 500°C and the results shows a grain size of 53nm with a fully BCC structure, suggesting that the grain growth of the BCC crystals have not reached the critical grain size associated with the BCC to FCC transformation. As previously described, the presence of Al in the alloy causes an increase of the SFE, which is believed to facilitate the crystal structure reversion. Thus, it is believed that the grain size at which the BCC to FCC transformation begins will be smaller than the Al-free system. Similarly, the heat treatment performed at 500°C for the nSS2Al resulted in a grain size of 87nm for the BCC crystals which are mixed with 4% of FCC crystals in the structure. The grain size to initiate the reversion of the strain induced transformation should be further reduced for the nSS6Al system as the SFE should be the highest for the three systems studied.

5.3.3 Effect of Process, Phase Microstructure and Consolidation Process on the Hardness

Figure 5.8 shows the Vickers hardness of SPS coatings specimens made out of nSS0Al, nSS2Al and nSS6Al systems as a function of grain size and FCC weight percentage measured by XRD. The hardness is increased as the grain size and the weight fraction of FCC decreases. The highest values of hardness is 476 VH for complete BCC and 98nm grain size (nSS0Al) while the lowest value of the hardness is 302 VH for 32 wt% FCC and 137nm grain size (nSS6Al). The hardness values in the samples are simultaneously influenced by two factors: (1) the grain size and (2) the fraction of the structure possessing the FCC structure, which is dictated by the Al content. Hardness follows the Hall-Petch relation where the hardness increases linearly as the square root of the grain size decreases. In all three cases, the grain size is higher than the critical grain size to sustain dislocations, validating the Hall-Petch behavior. However, the increase in hardness is significant for such a small difference in average grain size. As presented in Figure 5.7, for the systems containing Al, the samples possess a composite microstructure, containing BCC and FCC grains. Thus, the large softening is attributed to the fraction of FCC grains, which is associated to the Al content. The porosity could also play a role, but is not significant enough to explain these results. The inverse relation between the volume fraction of FCC and the hardness of nanostructured 316L SS, fabricated by cryogenic rolling and heat treatment has been reported by Ucok et al. [102]. However, it is worth

mentioning that the grain size range associated with the various concentrations of FCC phase was higher than in the present study.

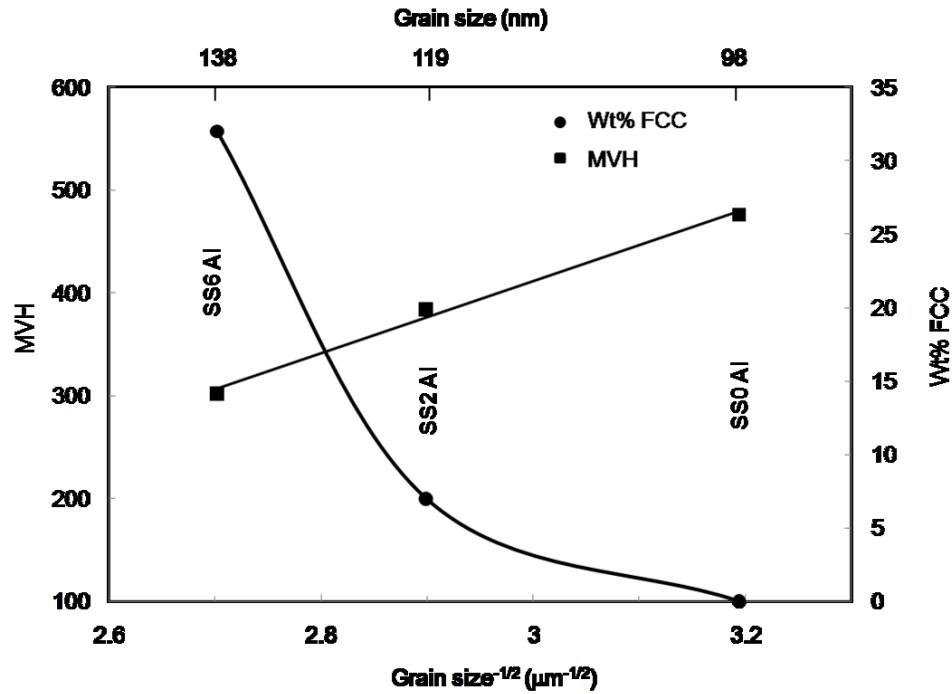


Figure 5.8 Microhardness of SPS for the three alloys as a function of FCC wt% and grain size.

5.4 Conclusions

The behavior of cryomilled nSS0Al, nSS2Al and nSS6Al powders was studied during the fabrication of coatings using SPS and was compared with the same milled powders annealed at various temperatures. The main results can be summarized as follows:

1. Mechanical alloying of Al for concentration of 2 and 6wt.% in 316LSS was successfully achieved after 32 hr of cryomilling. For the same milling time, the milled nSS0Al powders had a smaller, equiaxed morphology. The aspect ratio of the particles increased with increasing Al concentration.
2. The strain induced phase transformation from FCC to BCC during cryomilling is influenced by the Al concentration. The Al-containing stainless steel seems to have faster strain induced transformation in the early stage of milling, while the rate of transformation became similar thereafter for all systems.
3. Dense SPS coatings have been successfully produced with the three starting feedstock powders. The coating morphology is entirely dependant on the morphology of the starting feedstock, where the Al-containing coating had a lamellar microstructure.
4. The SPS process was found to have a small influence on the BCC to FCC phase reversion when compared to the level of transformation induced during the heat treatment trials. The thermal load imposed by the SPS process was insufficient to provide the energy necessary to recover the FCC structure for the nSS0Al.
5. Al enhances the reversion transformation from BCC to FCC for both SPS and heat treatment trials. The weight fraction of transformed FCC increases with the concentration of Al.
6. The combination of the metastable BCC structures and fine grain size contribute to increase in the hardness of the SPS coatings. The ratio of BCC/FCC structure is believed to be the primary factor driving the hardness.

6. THERMAL STABILITY AND OXIDATION BEHAVIOR OF AL-CONTAINING NANOCRYSTALLINE POWDERS PRODUCED BY CRYOMILLING

6.1 Introduction

Oxidation is the most important high temperature corrosion reaction in furnaces and boilers. The oxides of iron, nickel, and cobalt, which are the alloy bases for most of the engineering alloys, have significantly lower thermodynamic stability compared to the oxides of some of the solutes such as Al, Cr and Mg. Traditionally, ferritic steels containing Cr (e.g., 5%Cr-0.5Mo, 7%Cr-0.5Mo and 9Cr-1Mo) are used in the construction of tube bundles for boilers and furnaces due to their considerably reduced cost and high thermal conductivity [2]. The effect of the observed corrosion rates on the service life of tube bundles have been estimated for 9% Cr steel by Quadackers et al. [3]. Based on the data determined by Quadackers et al., the effects of oxidation on the service life of tube bundles cannot be neglected when examining wall thickness composed of 9% Cr below about 6 mm.

Aluminum oxide scales generally provide better oxidation resistance and yield lower oxidation rates than other oxides such as chromium oxide scale. Stainless steels (specifically the three-hundred series of Stainless Steel) are used widely for high temperature corrosion applications in furnaces and boilers. Significant developments have

been made in an effort to partially replace Cr with Al in austenitic 300 series stainless steels in order to change the formation of oxide scale from chromium oxide scale to Al oxide scale during oxidation [65]. The oxidation behavior of these alloys shows superior oxidation resistance in the temperature range between 800-1100 °C and was demonstrated to be moderately resistant to oxidation up to 1300 °C. The excellent oxidation resistance is attributed to the formation of a continuous aluminum oxide film, Al₂O₃ [65].

The formation of aluminum oxide should be continuous, compact and adherent to provide the maximum corrosion protection. The concentration of Al as a solute in the alloy should be above the critical concentration necessary to establish a complete pore-free surface layer of aluminum oxide. In practice, the higher Al concentration is necessary for the closely spaced precipitates to coalesce to form the healing layer [61, 103].

Nanostructured materials have been found to possess a high resistance for high temperature oxidation. Nanostructured coatings also promote the selective formation of protective oxidation scales due to the high density of grain boundaries, which provide fast diffusion paths [5]. In addition, scale adhesion and spallation resistance are improved by stress release and the micro pegging effect [5]. In nanostructured alloys, the Al content required to form a complete protective oxide scale can be substantially reduced. Work performed by Gao and Zhengwei showed that for nanocrystalline Ni-20Cr-Al containing ~2 wt. % of Al a complete α -Al₂O₃ scale could be developed at 1000 °C in air. This concentration is only 1/3 of the required Al content in the Ni-20Cr-Al alloy with normal grain size [5].

The present study was conducted to explore the oxidation behavior of nanocrystalline nSS6Al. The material was produced by cryomilling, a process in which powders are mechanically milled in slurry composed of milling balls and a cryogenic liquid [16]. The resulting powders were investigated as potential coating feedstock for the tube bundles of boilers and furnaces used in industrial applications.

6.2 Experimental

SS316L powders (16%Cr, 17.7%Ni, 2.2%Mo, 0.13%Mn, 0.75%Si, 0.01%C, balance Fe) from North American Hoganas were blended with 6 wt% elemental Al powder from Atlantic Equipment Engineers. The cryomilling process (Union Process attritor) was used to alloy the powders and to refine the grains to nanometer scale. The apparatus included a thermocouple that was used to monitor the temperature in the attritor and to ensure a constant level of liquid nitrogen. Evaporated liquid nitrogen from the milling vessel was compensated by continuously feeding liquid nitrogen into the mill to guarantee complete immersion of the powders. The rotation speed was kept constant at 220 RPM and the powders were milled for 32 hr. A powder to ball weight ratio of 1:20 was used. The surface area of the powders after milling was measured using the BET technique.

High temperature oxidation tests of the cryomilled powders were conducted at three different temperatures: 500 °C, 800 °C, and 1000 °C, respectively, for 48 hr. The

proposed temperatures cover different zones in the furnaces and boilers. Oxidation kinetics were measured using a gravimetric balance from Thermo Cahn. The apparatus continuously monitors the specimen's weight during testing with a recording microbalance. The powders were then put in a ceramic crucible, suspended from the microbalance by a preoxidized wire, and placed in a vertical tube furnace. The tube furnace was purged with argon, evacuated and preheated at heating rate of 10 °C per minute. Pure, dry flowing air was injected into the tube furnace and recordings of the weight changes were taken when the target temperature of the tube furnace was reached.

The milled powders and oxidation products were characterized by x-ray diffraction, scanning electron microscopy (SEM), transmission electron microscopy (TEM) and X-ray Photoelectron Spectrometer (XPS). Grain size measurement was carried out using CLEMEX image analysis software on TEM dark field micrographs.

6.3 Engineering the Starting Powders

The concentration of Al as the solute in the powders should be above the critical concentration necessary to establish a continuous protective layer of aluminum oxide during oxidation.

The critical concentration of Al above which aluminum oxide is formed was calculated using the following equation [61]:

$$N_{Al} = \frac{v}{Z_{Al} M_0} \times \left(\frac{\pi k_p}{D} \right)^{\frac{1}{2}} \quad (12)$$

In this equation v is the molar volume of the milled powder; Z_{Al} is the valence of the Al atoms; M_0 is the atomic weight of oxygen; D is the diffusion coefficient of Al in the iron and nickel [104, 105]; and k_p is the rate constant for oxidation. Figure 6.1 presents the theoretical critical Al concentration in stainless steel powder and in Ni-20Cr-Al required to form the desired aluminum oxide scale as a function of temperature using the relationship presented in equation 12. The Al critical concentration curve presented represents the theoretical behavior of micro-sized grain material. The coefficient of diffusion of Al in conventional material was used to predict the curve as no values for the coefficient of diffusion of Al in nanostructured material were found in the literature. Nevertheless, the critical concentration curve of Al in nanostructured powder is expected to shift down. Studies performed by Gao and Zhengwei [5] on an Al-containing nickel based alloy (Ni-20Cr-Al) was verified using equation 12. At 1000 °C, the critical concentration of Al required to form the Al₂O₃ protective layer was calculated to be 6 wt.%. Gao and Zhengwei showed experimentally that for an alloy containing 6 wt.% Al and possessing an average grain size of 10 μm, the aluminum oxide scale was developed. In addition, they verified that for the same alloy with an average grain size of 60 nm, only 2wt% of Al was necessary to develop the Al₂O₃ scale, which is three times lower than for

the conventional materials. In this study, 6wt% Al in stainless steel was selected since the concentration is slightly above the critical concentration for the formation of aluminum oxide scale at 800 °C.

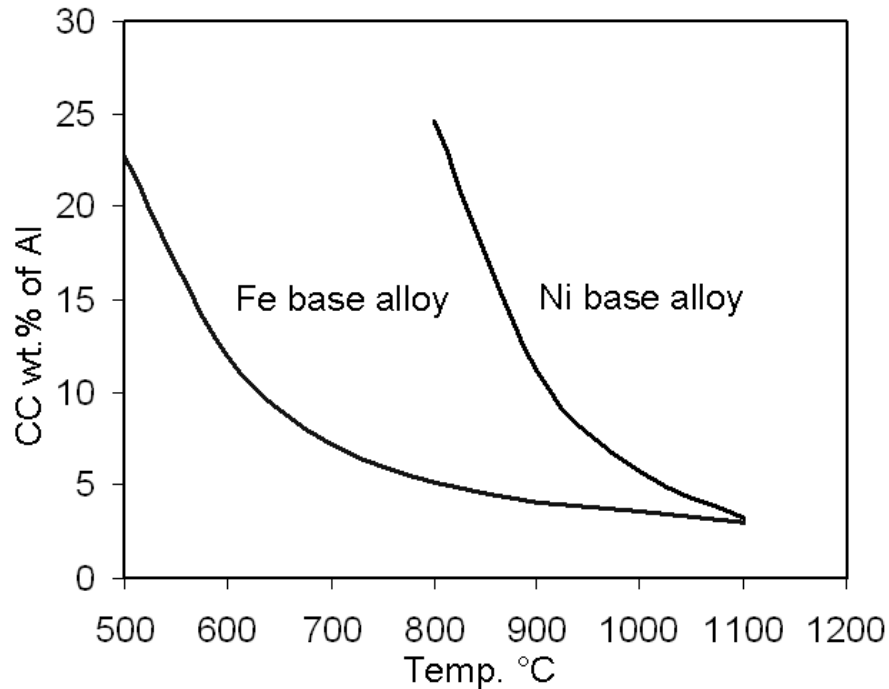


Figure 6.1 Theoretical Al concentration required to form the protective Al_2O_3 scale in iron and nickel based alloys.

6.4 Results and Discussions

The x-ray diffraction spectra of the cryomilled powders indicated that complete alloying of the Al was achieved after 32 hr of milling. Examination by TEM of the cryomilled powders after 32 hr reveals that the structure was in nanometer scale. A representative

dark field micrograph and grain size distribution of the as-milled nSS6Al powders are presented in Figure 6.2 (a) and (b). After examination of over 1100 individual grains, the measured average grain size of the as-milled powders was 6.7 nm. The grain size distribution shows a narrow distribution, where most of the grains are smaller than 10 nm. Combination of the XRD and the TEM results reveal successful mechanical alloying and grain refinements of the mixture by cryomilling due to good balance between cold welding and fracturing processes of the powders. Similar grain refinement and alloying kinetics was described by Huang and Lavernia for the Fe-10 wt.% Al powder system. They also reported in their study that complete alloying was obtained after 25 hr of milling and the final average grain size was 6 nm [17].

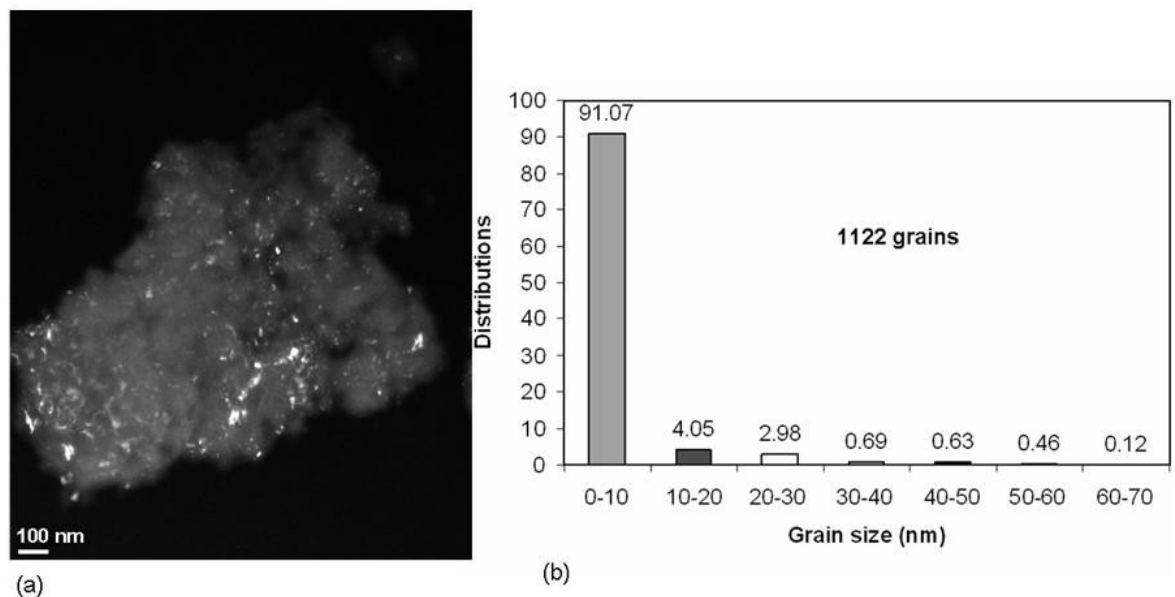
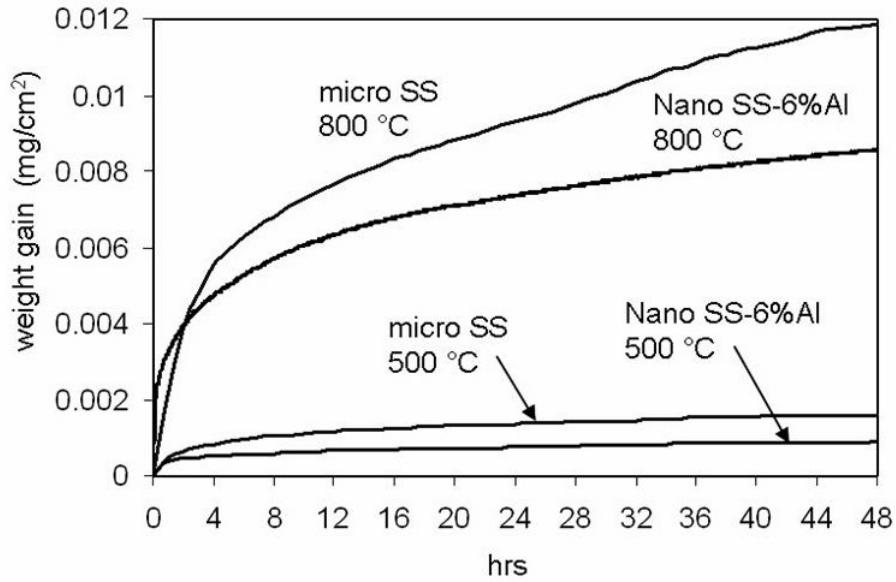
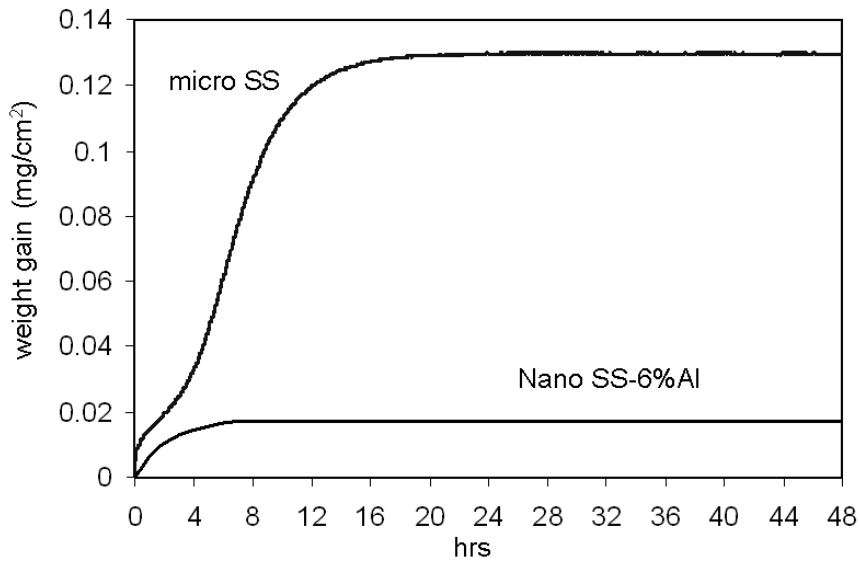


Figure 6.2 (a) Dark field TEM micrograph of a nanostructured particle as-milled for 32 hr and (b) grain size distribution measured from the TEM micrographs.

The oxidation kinetics results for the cryomilled powders tested for 48 hr at 500 °C, 800 °C and 1000°C, respectively, are presented in Figures 6.3 (a) and (b), respectively. For comparison, conventional stainless steel powders were also tested.



(a)



(b)

Figure 6.3 Oxidation kinetic of micro stainless steel and nSS6Al powders at (a) 500 °C and 800 °C and (b) 1000 °C.

For all tested temperatures, the nanocrystalline nSS6Al powders showed a lower weight gain and better oxidation than the conventional stainless steel powders. At 500 °C and 800 °C the weight gain of the nanostructured powders was almost two times lower than that of the micron-sized powders while the weight gain was seven times lower for the nanocrystalline nSS6Al at 1000 °C.

The morphology of the different oxide scales and the respective qualitative compositions were studied using SEM. Figure 6.4 (a) depicts the surface morphology of the oxide scale developed at the surface of conventional stainless steel powders after a heat treatment of 48 hr at 800°C and Figure 6.4 (b) shows the corresponding EDS analysis of the surface. As expected, the surface is covered by a Cr₂O₃ layer. The EDS spectra shows the presence of Fe, Si, Mn and Ni, which are believe to come from the bulk of the particle since the interaction volume is larger than the thickness of the scale. Some well defined crystals are observed and their analysis indicated Cr, Ni and O, which would correspond to NiCr₂O₄ spinel crystals. Figure 6.4 (c) shows the oxide grown on nanocrystalline powders containing 6wt%Al for the same heat treatment conditions and Figure 6.4 (d) presents the corresponding EDS analysis. It is worth mentioning that the EDS analyses were performed at 5keV, to limit the interaction volume between the beam and the material. Monte Carlo simulation using Electron Flight Simulator software indicated that the interaction volume would penetrate 250 nm deep into the substrate. The results suggest that the oxide layer is composed of Al₂O₃ and the detection of Fe and Ni would be generated by the bulk. The absence of Cr toward the surface of the particles would confirm that the formation of a Cr-based oxide was prevented by the preferred

development of the Al_2O_3 scale. A previous study has reported that during oxidation of nano-Aluminium, the $\alpha\text{-Al}_2\text{O}_3$ scale starts forming at 740°C [106] and thus it is expected that $\alpha\text{-Al}_2\text{O}_3$ will also be the grown oxide in the present work due to the faster nucleation of this stable reaction product.

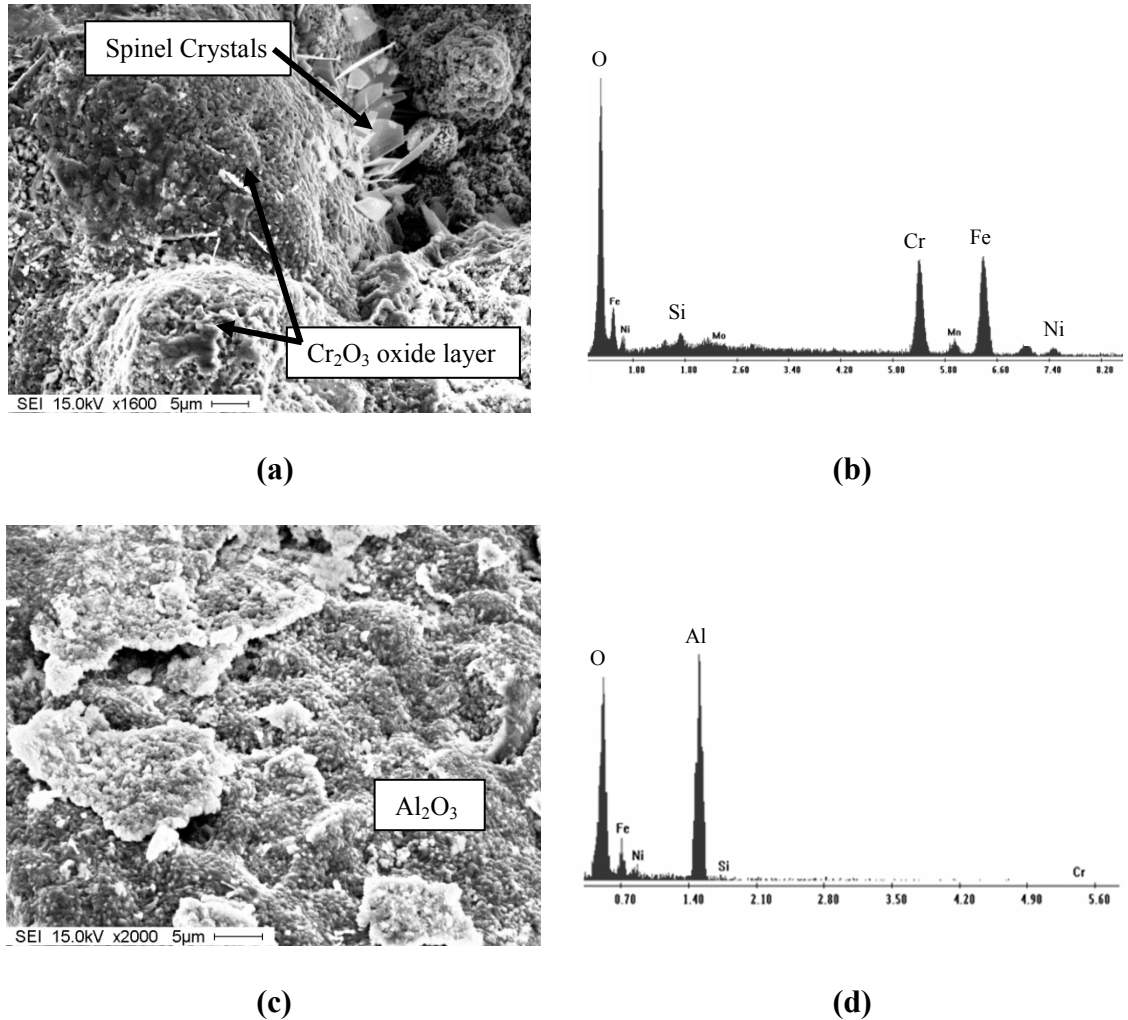


Figure 6.4 (a) Secondary electron SEM image illustrating the oxide scale of conventional stainless steel and (b) the corresponding EDS analysis, (c) SEM micrograph of the surface of the oxide scale present on cryomilled nSS6Al and (d) corresponding EDS analysis.

To validate the EDS analysis, XPS analysis of the thermally grown oxides was carried out for the three tested temperatures. Figure 6.5 shows the oxygen 1s spectra for the samples tested at 500, 800 and 1000°C, respectively. For the scale formed at 500°C, the O 1s reflection line of the surface oxide is located at 531.0 eV, which corresponds to the nominal value for Al₂O₃ [107]. With increasing the oxidation temperature, the position of the O 1s peak slightly shifts toward lower energy. For the oxide scale grown at 800°C, the reflection is observed at 530.2 eV, while the peaks for the oxide formed at 1000°C is located at 529.8eV. This reduction in bonding energy is in agreement with the results published by et al [108], which shown a reduction of 1eV in bonding energy between Al₂O₃ and Cr₂O₃ and the overall results correlate the SEM observations.

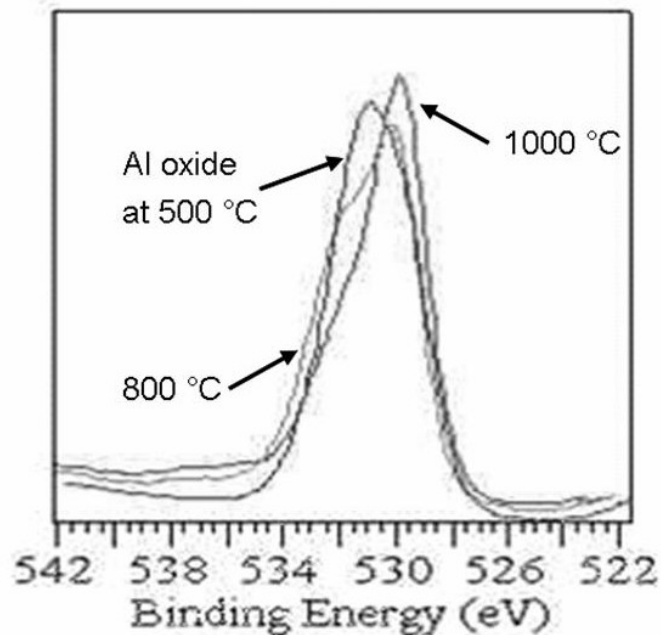
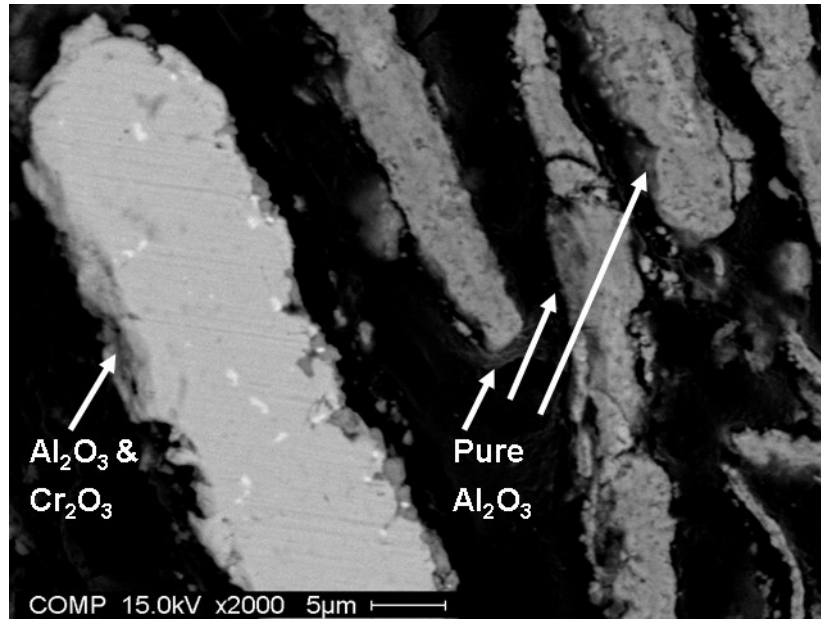


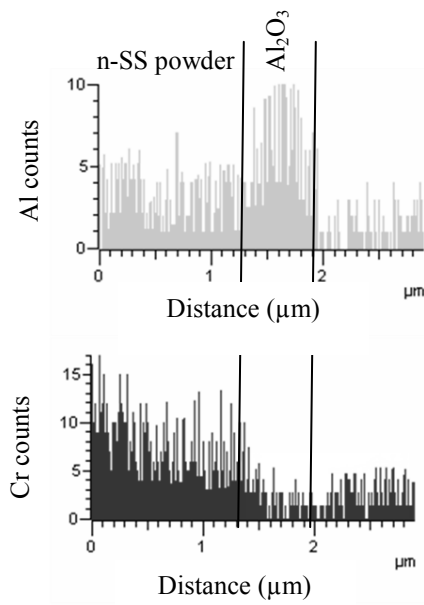
Figure 6.5 XPS multiplex spectra for nSS6Al powder samples after heat treatment at 500 °C, 800 °C and 1000 °C, respectively.

Figure 6.6 (a) shows a SEM micrograph of the cross section of a polished nSS6Al particles oxidized for 48 hr at 800 °C. As depicted in the surface oxide micrograph, most of the particles showed a completed outer Al₂O₃ scale, and a representative low voltage lines scans of this oxide scale is shown in Figure 6.6 (b). In some cases, the thermally grown oxide scale possesses a Cr₂O₃ layer underneath the Al₂O₃ scale, which is caused by local depletion of Al. Upon formation of the initial Al₂O₃ oxide scale, the concentration of Al becomes lower than the critical concentration to sustain growth of the oxide and nucleation of the second most favorable metal oxide begins. A representative low voltage line scan of this double oxide layer is shown in Figure 6.6 (c). It is believed that for such low oxidation time (48 hr), the premature depletion in Al is caused by a non-homogenous distribution of Al in the stainless steel powder after cryomilling.

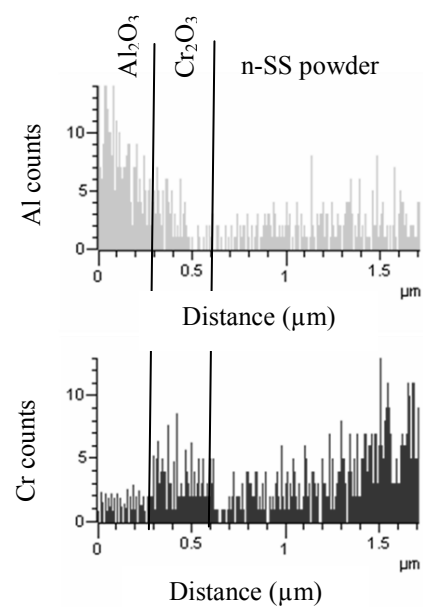
Figure 6.7 presents a representative TEM dark field micrograph and grain size distribution of a milled particle heat treated at 500 °C for 120 hr. Image analysis of the TEM micrographs yielded an average grain size of 11.4 nm after the heat treatment at 500 °C. The thermal stability shown by the powder is similar to other Al-containing iron powders manufactured by cryomilling. In fact, results from et al. have shown that the thermal stability of al-containing iron powders remains in the nanometric grain size range up to 0.7**M_p* of the alloy [16].



(a)



(b)



(c)

Figure 6.6 (a) SEM micrograph of the cross-section of nanostructured powders oxidized at 800 °C for 48 hr and (b) and (c) low voltage line scans of the single and double layers oxide scale.

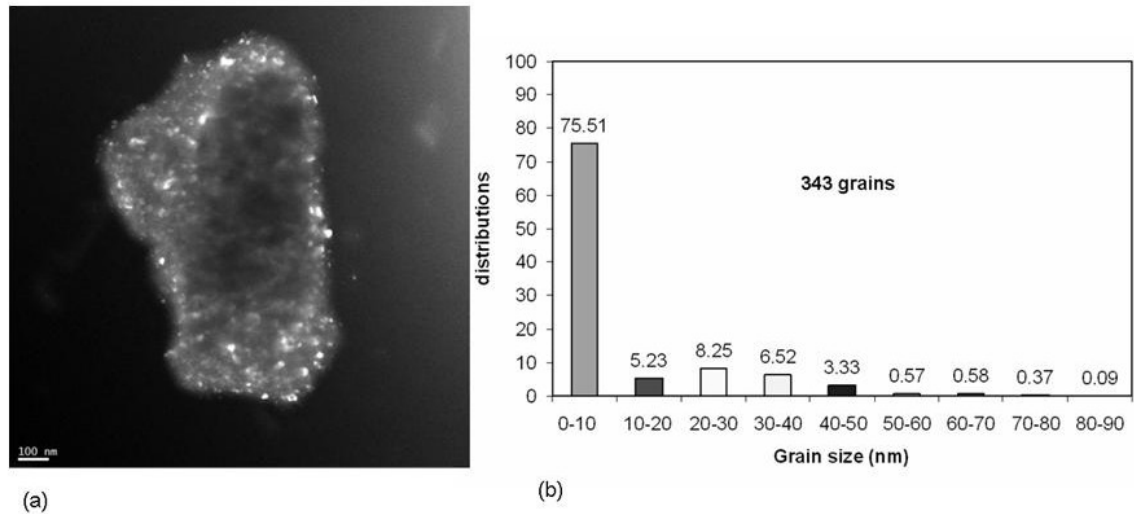


Figure 6.7 (a) Dark field TEM micrograph of a nanostructured particle heat treated at 500 °C for 120 hr. (b) Grain size distribution of the TEM image.

The results presented demonstrate that stainless steel containing ~6 wt% Al can form the desired protective Al_2O_3 scale at 500 °C while maintaining an average grain size in the nanometer range. In comparison with the theoretical behavior of micron-sized grain stainless steel (see Figure 6.1), the major benefit in using an alloy containing Al resides in the development of an Al_2O_3 scale which was found several times more resistant to weight gain than the scale developed in conventional material. It is also worth mentioning that the formation of Al_2O_3 at the tested temperatures in a nanostructured material occurs at a lower Al concentration than for an Al-containing iron based alloys with conventional grain size [68,69]. This is attributed to short-circuit outward diffusion of Al through the grain boundaries. In addition, the good grain growth stability may originate from fine

dispersed particles formed during cryomilling that subsequently impeded grain growth [13].

The activation energy from the oxidation reactions was calculated from the slope of the Arrhenius equation of oxidation rate constants (k_p) for conventional stainless steel and nanocrystalline nSS6Al powders, as shown in Figure 6.8. The calculated activation energy for the oxidation reaction of the nanocrystalline powders was 85 kJ/mole, which is approximately half the calculated activation energy of conventional stainless steel (181 kJ/mole). A study of the oxidation of Al powders showed that the activation energy of the nano-sized powders was approximately 33% lower than the activation energy of the same powder in the micron-scale range [106]. The reduction of the activation energy can be explained by the increased volume fraction of the grain boundaries in nanostructured materials compared to the conventional materials. Grain boundaries are sites of fast diffusion paths for atoms (D_{gb}), which significantly enhance the overall effect of diffusion (D_{eff}) and can be calculated by equation 16 [109].

$$D_{eff} = g D_{gb} + (1 - g) D_g \quad (16)$$

In the preceding equation D_g is the lattice diffusion and g is the volume fraction of the grain boundaries. Fast overall diffusion in nanocrystalline powders accelerate the oxidation process which lower the Al concentration needed to form healing oxide scale as was observed at 500 °C.

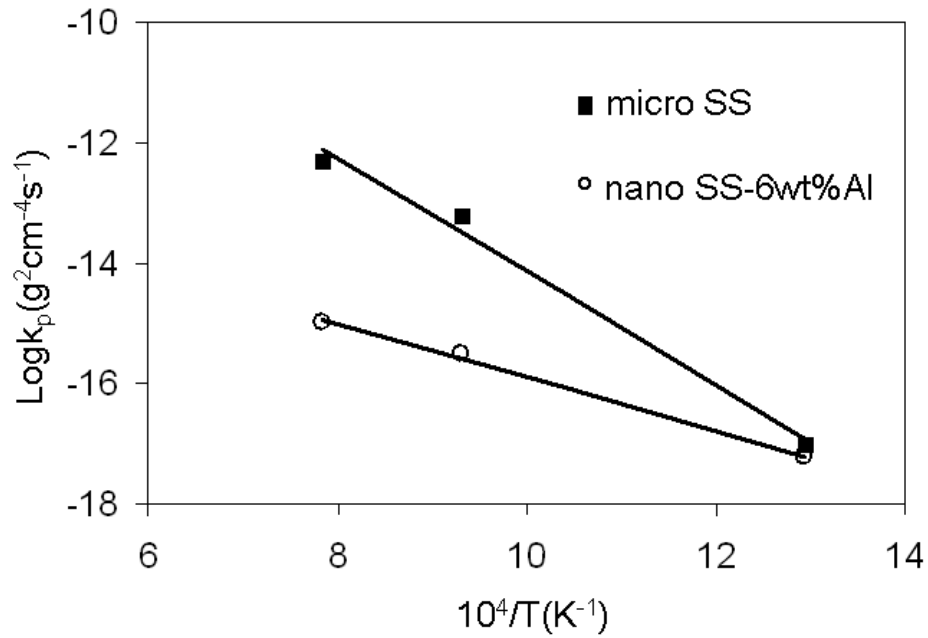


Figure 6.8 Arrhenius plot of the parabolic oxidation of micro stainless steel and nano SS6Al.

6.5 Conclusions

Nanocrystalline 316LSS containing 6 wt.% Al was successfully produced by cryomilling. The cryomilled powder demonstrated good grain growth stability at 500 °C when the powders had been heat treated for 120 hr and the average grain size was found to be 11.4 nm. The XPS and SEM/EDS analysis showed that pure aluminum oxide scale formed and was the predominant oxide phase after heat treatment at 500 °C. The activation energy of the nanostructured powders was found to be almost 50% lower (85 vs. 181

kJ/mol) than the conventional powders due the higher number of grain boundaries, which resulted in a higher rate of diffusion in the nanostructured powders.

7. OXIDATION BEHAVIOR OF AL-CONTAINING STAINLESS STEEL COATINGS PRODUCED BY CRYOMILLING AND SPS

7.1 Introduction

Stainless steel is one of the most important and widely used alloys and has found many applications in oil and nuclear industries, in which the material is often exposed to high temperature corrosion and mainly oxidation. Depending on the exposed environment, i.e. oxidizing species, oxygen partial pressure, temperature and time, the oxide layer formed at the surface is altered and can be composed of two distinct layers or a single mixed oxide. Several studies were performed to investigate the chemical composition of the oxide layer forming on stainless steel at different temperatures and oxygen partial pressure [52-58]. At a temperature above 400 °C and oxygen pressure lower than 10^{-3} Pa, a uniform Cr_2O_3 oxide layer is predominately developed. In air, at atmospheric pressure and throughout a wide temperature range, double oxide layers are present in the scale, an inner Cr_2O_3 oxide layer and outer $\alpha\text{-Fe}_2\text{O}_3$ oxide layer [52-58].

For higher temperature applications, Cr-based scales suffer in efficiency, which strives for the need of development of stainless steel grades possessing improved oxidation performance, like system forming Al_2O_3 -based scale for example. Significant efforts

have been made to partially replace Cr with Al in austenitic stainless steel in order to modify the scale composition during oxidation from Cr_2O_3 scale to Al_2O_3 [65]. A new Al-containing stainless steel based grade containing 5wt%Al showed good oxidation resistance in the temperature range between 800 and 1100 °C, and moderate resistance between 1100 and 1300 °C. Moreover, independently of the tested temperature, the oxidation resistance was higher for the Al-grade when compared to the conventional alloy [65].

The protective Al_2O_3 scale should be continuous and cohesive to provide maximum corrosion protection. To reach this objective, the Al solute concentration in the alloy must exceed the critical concentration necessary to establish a complete pore-free surface layer of Al_2O_3 . In practice, a relatively high Al content is necessary for the Al_2O_3 nucleation sites to coalesce and form a continuous layer [61, 103]. This concentration varies, depending on the diffusion of the solute elements and oxidation temperatures. Dunning et al. [69] investigated the effect of addition of Al and Si up to 2 wt% on the oxidation response of stainless steel (Fe-16Cr-16Ni-2Mn-1Mo) at 800 °C. The Al-containing stainless steel showed poor oxidation resistance and exhibited weight gain approximately two times greater than the baseline alloy. Dunning et al. concluded that 2 wt% Al is below the critical concentration to form the continuous Al_2O_3 scale at 800 °C. Although numerous trials have been made over the past 30 years to create Al_2O_3 -forming austenitic stainless steel for high temperature applications, it is still proven to be challenging [70].

The elevated Al concentrations required to improve corrosion resistance often degrade the mechanical properties of the alloy [110]. A potential solution at hand is nanostructured Al-containing stainless steel. These materials should produce high quality scales resisting to high temperature oxidation with lower Al content due to the higher volume fraction of grain boundaries enhancing diffusion of the Al solute to the surface [5]. Gao and Zhengwei [5] reported that a dense α -Al₂O₃ scale can be formed on Al-containing nanocrystalline nickel base alloy (Ni-20Cr-2Al) during a heat treatment at 1000 °C in air. The Al content in this nanocrystalline nickel alloy is just 1/3 of Al content required to form an Al₂O₃ scale for conventional micron-sized-grain alloy [5]. The relationship between the oxide products, coating grain size and Al content indicates that the selective formation of Al₂O₃ can be greatly promoted by the nanocrystalline structure [5]. Due to the same reason, the critical Al concentration in nanostructured stainless steel required to form a complete protective oxide scale can be substantially reduced in comparison to the conventional Al-containing stainless steel, which can minimize the detrimental impact of Al on the mechanical properties. Almathami et al. [96] have calculated the critical Al concentrations of FCC alloy to yield a continuous external Al-scale at 800 °C and 1000 °C to be 24, and 6 wt%, respectively. To take advantage of the oxide selectivity, the coating or cladding must retain the nano-sized grain upon deposition. SPS is a newly developed process which makes possible to consolidate various kinds of powders under the form of bulk nanomaterials or claddings while maintaining the nanograin size [38-42].

Numerous works were conducted on SS316L to determine the high temperature corrosion resistance in various environments. However, no study on the effect of modifying the

compositions through the addition of Al solute concentration and grain size on its high temperature performance has been conducted. In the present study, the influence of various Al-content to a SS316L on its microstructure development during milling, consolidation and its behavior during static oxidation tests has been investigated. Four different stainless steel coating systems were studied: conventional and nanostructured SS316L, and SS316L containing 2 and 6 wt% Al. The grain refinement to the nanoscale and the mechanical alloying were performed using cryomilling, and the claddings were produced by SPS process.

7.2 Experimental

Grade 316L austenitic stainless steel powder (17 % Cr, 13.5 % Ni, 2.2 % Mo, 0.14 % Mn, 0.81 % Si, 0.02 % C, balance Fe) supplied by North American Hoganas was used as a starting material. In addition, two alloys containing 2 and 6 wt% Al were produced through the mixing of elemental Al powder (Atlantic Equipment Engineers) into the stainless steel powder prior to milling. The SS0Al, SS2Al and SS6Al are used herein as acronyms to identify the stainless steel alloys containing 0, 2 and 6 wt% Al, respectively, while the prefix n was used to denote a nanostructured grade. A Union Process attritor (HD-01) was used to cryomill the mixture of powders, allowing for alloying and grain refinement to the nanometer scale. The level of liquid nitrogen was monitored by thermocouples to ensure a complete immersion of the powders during milling. The rotation speed was kept constant at 220 RPM and the powders were milled for 32 hr. A

powder to ball weight ratio of 1:20 was used. The surface area of the powders after milling was measured using the BET technique.

SPS process was used to coat the nanostructured powders onto stainless steel substrate. The nanostructured alloys were sintered in a doctor sinter 515-S press. A heating rate of 95°C/min was used to reach the sintering temperature of 950 °C followed by a holding time of 2 min. The consolidation was performed in a graphite mold in a vacuum environment.

High temperature oxidation tests of the cryomilled powders and coatings were conducted at three different temperatures: 500 °C, 800 °C, and 1000 °C. The powders were oxidized for 48 hr, while the coatings were oxidized for different time. Oxidation kinetics of the nanostructured feedstock were measured using a gravimetric balance from Thermo Cahn. The apparatus continuously monitors the specimen's weight during testing with a recording microbalance. The balance was installed in a tube furnace, which was purged with argon, evacuated and preheated at heating rate of 10 °C per minute. Dry air was injected into the tube furnace, and recordings of the weight changes were taken when the testing temperature was reached.

The milled powders, coatings and oxidation products were characterized by means of X-Ray Diffraction (XRD) in a Philips PW 1710 diffractometer using CuK_α radiation at 40 kV and 20 mA. Quantitative analysis of the volume fraction of crystal structures after high temperature exposure was performed using XRD patterns based on relative peak

intensity ratio, as described by Cullity [77]. An intensity ratio calibration curve was used so that the level of crystal structure reversion at the elevated temperatures was accurately inferred. A JEOL JSM-840A scanning electron microscope (SEM) operated at 15 kV was used to study the morphology and the cross sections of coatings after oxidations.

7.3 Results and Discussions

7.3.1 Fabrication of the Nanostructured Feedstock

Cryomilling was used to refine the grain size down to the nanometer level and to alloy the starting powders with Al to produce two Al-containing alloys possessing 2 and 6 wt% Al. The average grain size for the three milled systems measured by XRD was 13, 21 and 25 nano meter for nSS0Al, nSS2Al and nSS6Al, respectively. Complete alloying between Al and SS powders was obtained after 32 hr of milling. An interesting particularity of this system was the strain induced transformation occurring during milling, which yielded a BCC crystal structure. This metastable crystal structure reverted to the stable FCC during conventional heat treatments and its level of reversion was influenced by the Al content, where the Al strongly contributes to the stabilization of the FCC crystal structure. The complete investigation regarding the nanostructure powder stability and evolution can be found in Almathami et al. [98].

7.3.2 Thermodynamic Calculations for Oxidation Behaviors

Thermodynamic analyses of the oxidation behaviors of the present steel grades have been conducted with the FactSage thermochemical software [111]. Both FToxid database and FSSstel database were used in the calculations for oxide phases and metallic phases, respectively. During oxidation of stainless steel, the oxygen partial pressure can vary through the thermally grown oxide layers. The oxygen partial pressure at the oxide/metal interface can be considered to be in metallic saturation. The oxygen partial pressure can increase in oxide layer and eventually become 0.21 bar at oxide/air interface. The oxide phases developed during oxidation can be varied with steel compositions.

Figures 7.1 (a) and (b) show the calculated oxidation behaviors of the SS and SS6Al at 800 °C, respectively. For the SS grade, the substrate has a FCC structure at 800 °C and the first oxide on the metal/oxide layer interface is the corundum phase. The composition of corundum phase is Cr_2O_3 . The subsequent layer developing is a spinel oxide of $(\text{Fe,Cr,Ni})_3\text{O}_4$. This phase forms due to the increasing oxygen partial pressure. The predicted top layer of scale is a mixture of corundum $(\text{Fe,Cr})_2\text{O}_3$ and spinel $(\text{Fe,Ni})_3\text{O}_4$. For the SS6Al, the predicted scale composition was found different. The metallic substrate is mainly composed of FCC phase, but the calculation indicated the possibility of having BCC and AlNi phases. The first layer adjacent to the substrate should be a corundum phase, Al_2O_3 , as the oxygen partial pressure necessary for its formation ranges between $-38 < \log \text{PO}_2 \text{ (bar)} < -27$. Due to the consumption of the Al from the substrate

through the oxidation, the AlNi and BCC phases are expected to disappear. With the increase of oxygen partial pressure, Cr oxidizes to form $(\text{Al,Cr})_2\text{O}_3$ spinel phase and this phase develop above the initially formed Al_2O_3 layer. With further increase in oxygen partial pressure, spinel $(\text{Fe,Cr,Ni})_3\text{O}_4$ should develops. The predicted top layer of the scale can be a mixture of $(\text{Fe,Cr})_2\text{O}_3$ and $(\text{Fe,Ni})_3\text{O}_4$. Since the Al initially available in the substrate is consumed to form the Al_2O_3 and $(\text{Al,Cr})_2\text{O}_3$ layers near the metal/oxide interface, the concentration of Al in the spinel and top layer should be low. The calculated scale microstructures are summarized in Figures 7.2 (a) and 2 (b) for the two respective alloys. The calculation of the oxidation behavior for the SS2Al is similar to that of the SS6Al, although the amount of Al oxides are less. In addition, from a thermodynamic viewpoint, the scale evolutions for these three systems at other temperatures, such as 500 °C and 1000 °C are similar to the results obtained at 800 °C.

As the thermodynamic calculations were carried out without any consideration of diffusion and the entire steel was forced to be oxidized at given oxygen partial pressures, the calculated results can be inconsistent with experimental results. However, the initial oxidation behavior such as Al_2O_3 layer formation in Al containing stainless steel can be well predicted.

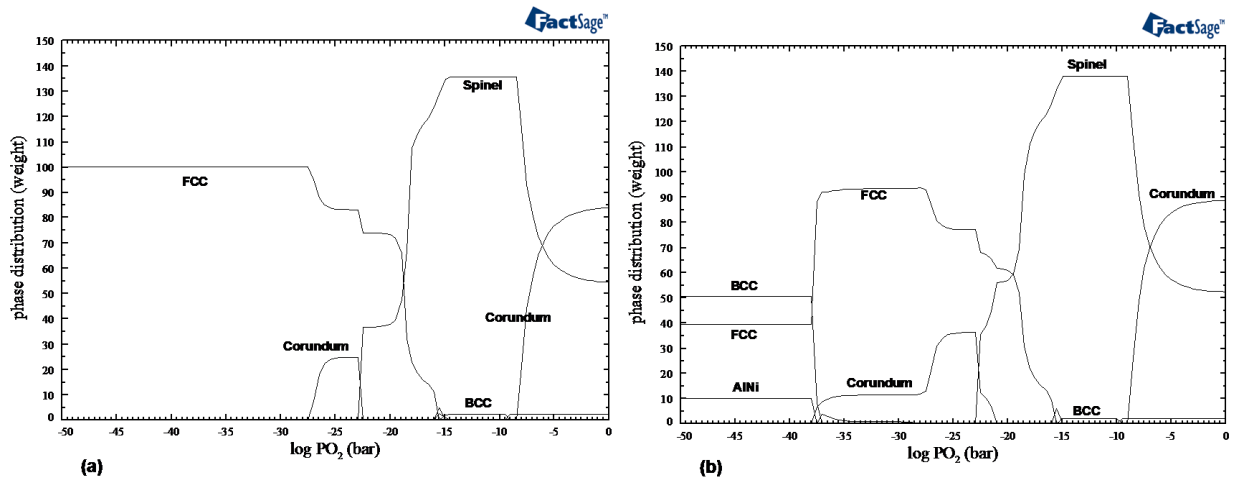


Figure 7.1 Calculated oxidation behavior of stainless steels at 800 °C. (a) SS (b) SS6Al. In the calculation, the initial metal was set to be 100 gram.

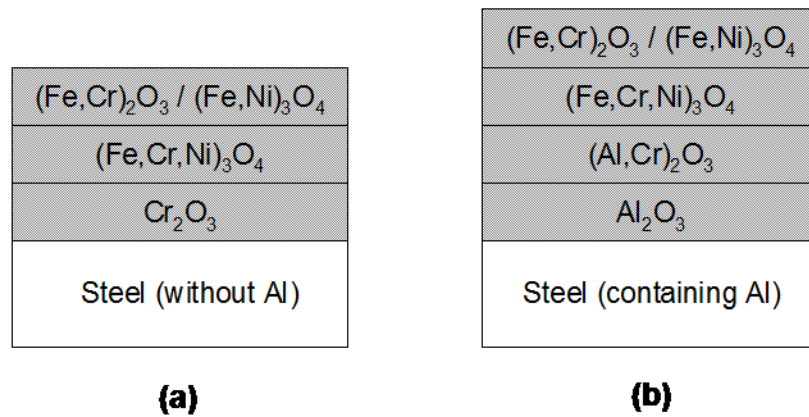


Figure. 7.2 Schematics of the oxidation layer, thermodynamically calculated from FactSage [111]. (a) SS and (b) SS6Al.

7.3.3 Oxidation of the Nanostructured Feedstock

The measurement of the oxidation kinetics was conducted for the four alloys, namely conventional SS, nSS0Al, nSS2Al and nSS6Al with a TGA at 500 °C, 800 °C and 1000

°C for 48 hr. Figure 7.3 presents the TGA traces for the two Al-free compositions, the conventional and the nanostructured feedstock, and the Al-containing compositions, nSS2Al and nSS6Al at 800 °C oxidation. The oxidation curves follow parabolic oxidation which indicate diffusion reaction kinetics [112,113]. The diffusion kinetics of nSS was very fast compared to the other alloys and the parabolic trend was shown for the first two hr of oxidation. For all tested temperatures, the Al-containing alloys showed a lower weight gain than the Al-free compositions. At 500 °C and 800 °C the weight gain of the Al-containing alloys was almost two times lower than that of the Al-free compositions while the weight gain was seven times lower for the Al-containing alloys at 1000 °C.

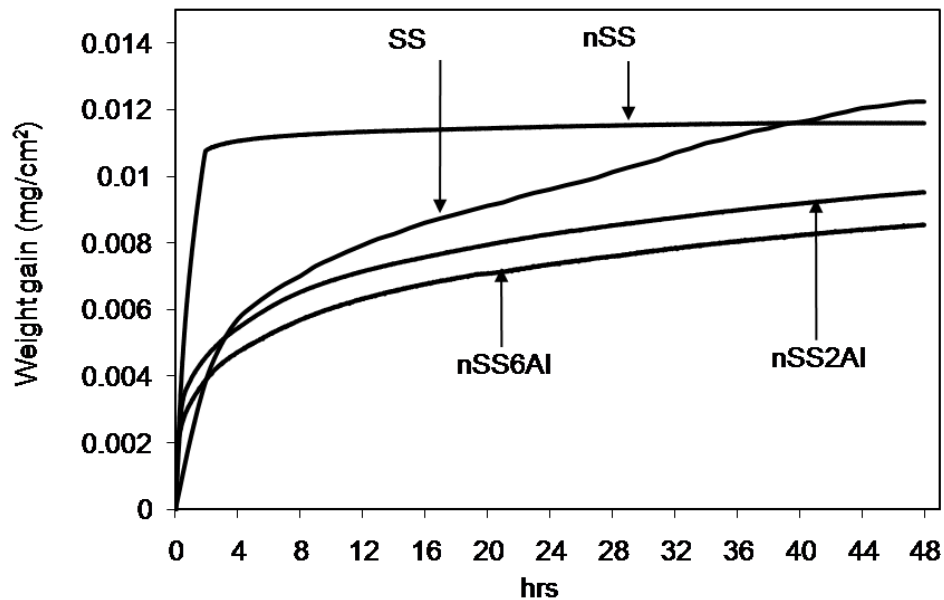


Figure 7.3 Oxidation kinetic of the four SS-based powder systems oxidized at 800 °C.

The oxidation rate constant for the feedstock was calculated for all systems and all tested temperatures and the results are presented in Table 7.1. The oxidation rate constants of the nano-structural SS are higher than the oxidation rates of conventional SS for all tested

temperatures due to the faster diffusion caused by the nanograins. The oxidation rate constants of Al-containing alloys are lower than the rate constant of free Al-free alloys at all tested temperature, which is caused by the outward diffusion of Al and slower oxidation kinetics once the initial Al₂O₃ formed. The rate constants for the growth of Cr₂O₃ and Al₂O₃ oxides reported in the literature are plotted in Figure 7.4 [114]. The oxidation rate at 1000 °C for Al-free alloys are lower than the growth of Cr₂O₃ and also the rate constants for Al-containing alloys are lower than the Al₂O₃ growth as shown from Figure 7.4 The presence of FCC crystal structure in stainless steel and the alloying elements have more control in the solute diffusion compared to metals.

Table 7.1 Oxidation rate constants calculated from weight gains at the tested temperatures.

Temperature (°C)	System	Rate constant (g ² cm ⁻⁴ s ⁻¹)
500	SS	2.0 x 10 ⁻¹⁷
	nSS0Al	4.3 x 10 ⁻¹⁴
	nSS2Al	4.8 x 10 ⁻¹⁷
	nSS6Al	2.3 x 10 ⁻¹⁷
800	SS	1.3 x 10 ⁻¹³
	nSS0Al	5.0 x 10 ⁻¹²
	nSS2Al	7.2 x 10 ⁻¹⁵
	nSS6Al	1.2 x 10 ⁻¹⁵
1000	SS	9.6 x 10 ⁻¹³
	nSS0Al	1.3 x 10 ⁻¹¹
	nSS2Al	1.1 x 10 ⁻¹⁴
	nSS6Al	6.0 x 10 ⁻¹⁵

The activation energies for the oxidation reactions were calculated from the slopes of the Arrhenius equations of the oxidation rate constant (k_p) plots for the four alloys, as shown in Figure 7.4, and the results are presented in Table 7.2. The calculated activation

energies for the three nanostructured alloys are 97 kJ/mol for nSS, 93 kJ/mol for nSS2Al and 85 kJ/mol for the nSS6Al. The values are all within the same order of magnitude and approximately half the calculated activation energy of 181 kJ/mol obtained for the conventional stainless steel. The reduced activation energy for the nanostructured alloys can be explained by the higher diffusivity arising from a higher volume fraction of grain boundaries for the nanostructured alloys which act as fast diffusion paths for elements. Grain boundaries are sites of fast diffusion paths for atoms (D_{gb}), which significantly enhance the overall effect of diffusion (D_{eff}) and can be calculated by Equation 16 [109].

$$D_{eff} = g D_{gb} + (1 - g) D_g \quad (16)$$

In the preceding equation D_g is the lattice diffusion and g is the volume fraction of the grain boundaries. The grain boundaries diffusion D_{gb} decreases much less than the lattice diffusion D_g with a decrease in temperature [115]. The rate constants in Figure 7.4 of the diffusion oxidation kinetic mechanism shows greater decrease of the rate constants for the conventional stainless steel (where lattice diffusion D_g is more effective) with a decrease in the oxidation temperatures compared to nanostructured alloys (where grain boundaries diffusion D_{gb} is more effective) which show smaller reduction of the rate constants, lower slope for the Arrhenius plot and lower activation energy.

The calculated activation energies of strain induced phase reversion (90 kJ/mol) [98] and oxidation (85 kJ/mol) for alloy nSS6Al are similar which may suggest that the two processes have similar diffusion-based mechanism. Murayama et al. [84] showed that the

strain induced phase reversion in 316 SS during heat treatment is produced by a dislocation gliding and mobility mechanism across the crystal structure. This diffusion based phase transformation could enhance the diffusion of elements and solutes during oxidation for nSS0Al, nSS2Al and nSS6Al. Thus, in addition to the high volume fraction of fast diffusion paths (D_{gb}) present in nanomaterials, the dislocation mobility occurring during the crystal structure reversion when the coatings are exposed to oxidation can facilitate the diffusion of Cr and Al towards the surface. As shown in Figure 7.3, more than 50% of oxidation and weight gains of the nanostructured alloys take place at the first hour of oxidation which correspond to the period during which the strain induced phase reversion was fully reverted for the alloys [98].

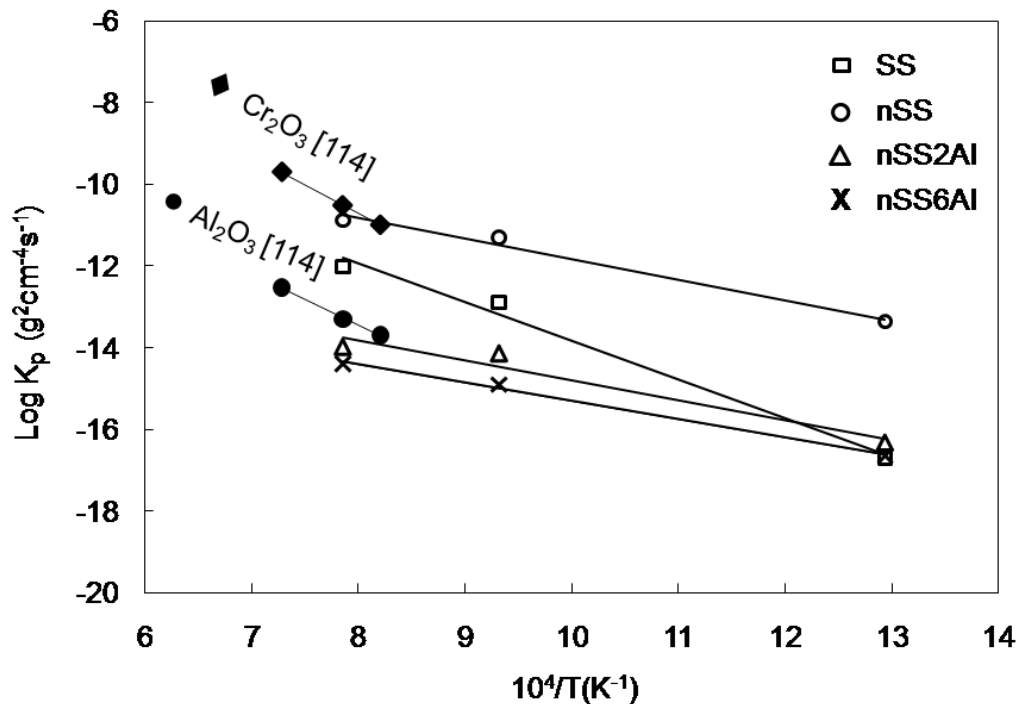


Figure 7.4 Arrhenius plot calculated from the oxidation traces of the SS, nSS, nSS2Al and nSS6Al and the rate constants of Cr₂O₃ and Al₂O₃ growth from literature [114].

Table 7.2 Activation energy calculated from the TGA curves for the present alloy systems.

System	Activation energy (kJ/mol)
SS	181
nSS0Al	97
nSS2Al	93
nSS6Al	85

7.3.4 Coating Microstructures Obtained by SPS

The coatings were fabricated by SPS for which the conventional and nanostructured feedstock were sintered at the surface of a conventional stainless steel substrate. SPS was used since this process is known to maintain nano and near nano-grains upon consolidation. Figure 7.5 presents an optical micrograph of a coating fabricated using conventional stainless steel powders. The level of porosity in the coatings was measured by image analysis and the results have shown that for all systems, the coatings were above 98% dense. Also, the SPS process had a minimal influence on the crystal structure reversion, which is the opposite behavior observed for conventional heat treatments. Thus, the nSS0Al system remained with a BCC structure upon consolidation, while the system with nSS2Al and nSS6Al retained 93 and 68 wt% of the BCC structure, respectively. The complete description of the microstructure evolution occurring during the consolidation of the three systems is presented in Almathami and Brochu [116].

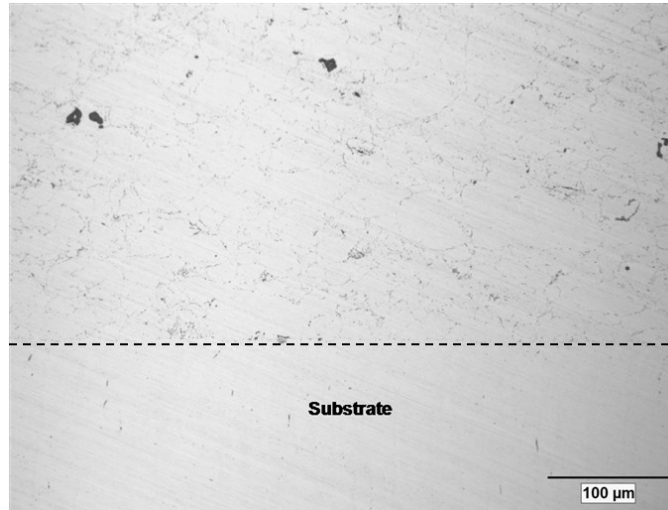


Figure 7.5 Optical micrograph of a cross section of a SS coating on a SS substrate.

7.3.5 Oxidation of the Al-Free Stainless Steel

The surface morphology of the oxide scales developed on the Al-free SS has been studied. Figure 7.6 presents a secondary image micrograph of the surface scale developed on the SS after a holding time of 48 hr at 800 °C. The EDS analysis of the surface scale highlighted only Fe and O, suggesting that the oxide scale developed is solely composed of iron oxide. It is worth mentioning that the EDS analyses were performed at 15 keV. Monte Carlo simulation using Electron Flight Simulator software indicated that the interaction volume would penetrate 920 nm within the scale. The results suggest that the surface oxide layer is composed of Fe_2O_3 and the electron beam did not interact with either a sub-scale layer or the substrate. Iron oxide-based scales grow rapidly and are known to provide weak oxidation resistance. The scale exhibits surface micro-cracks, and

well-defined spinel crystals are also observed. The combination of literature data [117-119] and current EDS analysis indicated that the spinels would correspond to Fe_3O_4 .

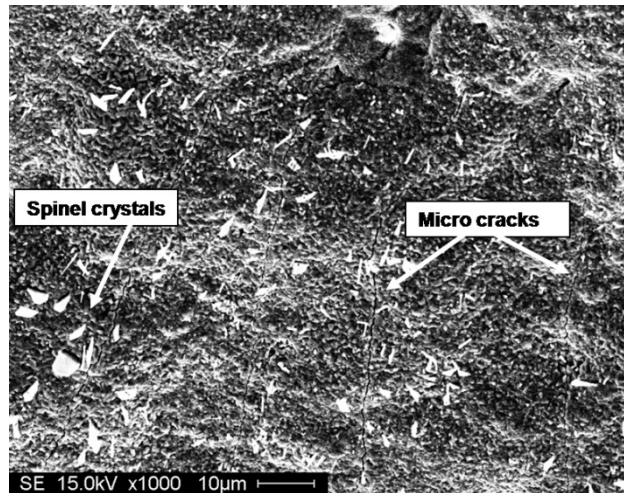


Figure 7.6 Secondary electron micrograph depicting the surface oxide morphology of SS alloy oxidized at 800 °C for 48 hr.

Polished cross sections of the various scales developed at 500, 800 and 1000 °C were examined using SEM and EDS analysis. Figure 7.7 (a) and (b) depict a micrograph of the cross section of the scale for the SS alloy and the corresponding EDS line scan of the oxide layer developed after an oxidation treatment of 200 hr at 800 °C, respectively. The oxide scale of SS is composed of the outer Fe_2O_3 scale and the thin inner Cr_2O_3 layer at the metal/oxide interface. Between these two layers, an intermediate oxide containing Fe, Cr and O formed. The gradual increase in the Fe signal and gradual decrease in the Cr signal suggest a $(\text{Fe,Cr})_2\text{O}_3$ local solid solution chemistry evolving towards the outer Fe_2O_3 oxide layer. The results obtained in this study are in agreement with the TEM work combined with chemical composition analysis performed by Sun et al. [120] on oxidized

316 SS sheet, which showed that the outer to inner oxide layers are $(\text{Fe,Cr})_2\text{O}_3$, $(\text{Fe,Cr})_3\text{O}_4$ and Cr_2O_3 , respectively. These results are in agreement with the thermodynamic predictions aside from the fact that the detected outer scales do contain neither Cr nor Ni. It is worth mentioning that the thermodynamic calculations has no consideration of the oxidation diffusion of alloying elements, but the calculation are for the complete oxidation of the initial metallic component. The absence of Ni can be explained by the non-complete oxidation of the substrate and that for even longer oxidation experiments, the Ni-based compounds would appear. Sun et al. [120] also showed that Ni was not present in the outer oxide scale during oxidation of 316 SS, suggesting that their oxidation tests were not long enough to obtain oxidation equilibrium.

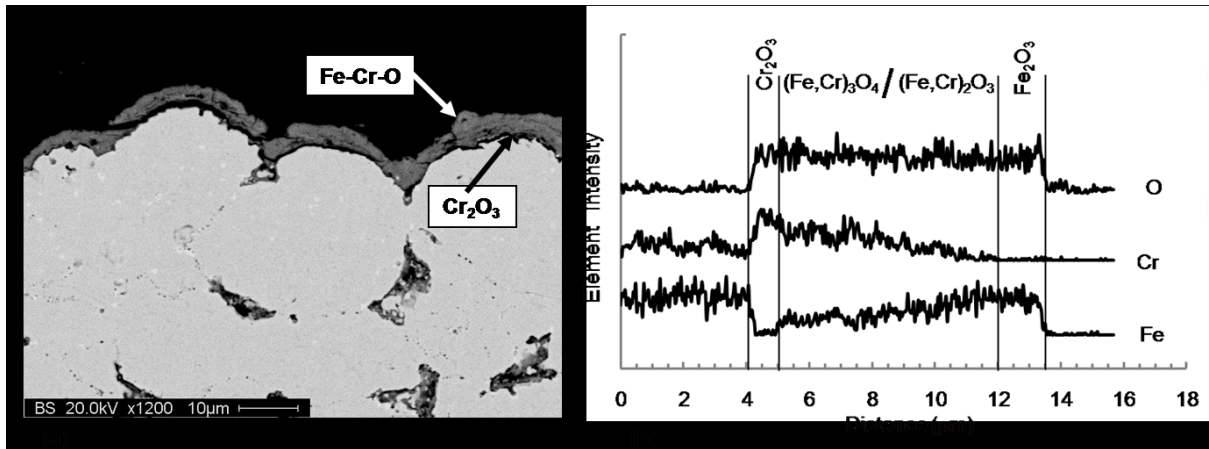


Figure 7.7 (a) SEM micrograph of the cross-section of SS alloy oxidized at 800 °C for 200 hr, (b) line scans illustrating layers of oxide scale.

The same three layers (Fe-based, Fe- and Cr-based, and Cr-based layers) were observed at the surface of the nSS0Al alloy after the same oxidation treatment, but the respective thicknesses ratio were different. Figure 7.8 (a) and (b) depict the cross section of the scale

for the nSS alloy and the corresponding EDS line scan of the oxide layer formed after 200 hr of oxidation at 800 °C, respectively. Similarly to the SS coating, the oxidation behavior seems to be in agreement with the thermodynamics aside from the absence of the detection of Ni in the various layers of the scale, which is again explained by the fact that the substrate did not reach oxidation equilibrium.

The thickness measurements of the scale developing during oxidation performed using the line scan traces for the nSS0Al show that both the outer and inner layers are thicker. The outer Fe_2O_3 scale had a thickness of $16 \pm 4 \mu\text{m}$ while the inner protective Cr_2O_3 and the intermediate Cr-rich oxide are $3 \pm 1 \mu\text{m}$ and $18 \pm 6 \mu\text{m}$ thick, respectively. Fe to Cr intensity ratio acquired from the EDS analysis suggests that the intermediate oxide scale of nSS alloy is the more Cr rich oxide, $(\text{Fe,Cr})_3\text{O}_4$. High diffusion paths for the nSS0Al alloy at this temperature result in enhanced diffusion of Cr that form the thicker inner protective Cr_2O_3 and the Cr enrichment intermediate layer.

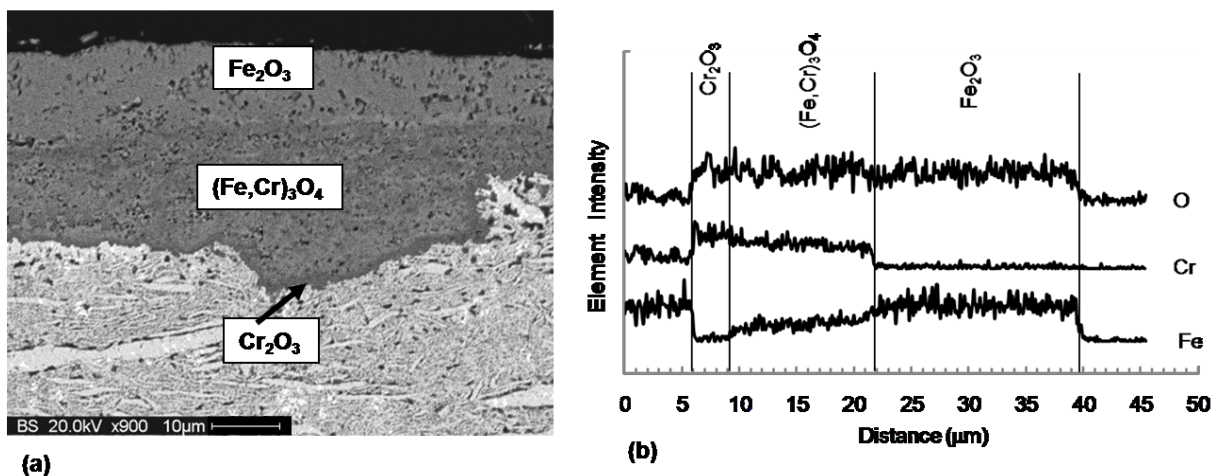


Figure 7.8 (a) SEM micrograph of the oxide scale developed for nSS at 800 °C (b) line scans illustrating layers of oxide scale.

Cyclic oxidation tests consisting of 10 cycles of heat up to 800 °C followed by a soaking of 50 hr and finally cooled down to room temperature were performed to investigate the adhesion strength of the developed scale. As presented in Figure 7.9, for the nSS0Al samples, the results indicate that the remnants of the thermally grown oxide are the inner layer of Cr₂O₃ and the intermediate layers containing Fe, Cr and O. The outer layer composed of Fe₂O₃ had completely spalled out of the scale. The most probable explanation is the high stresses generated during the growth of the Fe₂O₃, despite its relatively higher plasticity compared to other oxide. Growth stresses could be due a number of causes, while the most important reason being the volume difference occurring during oxidation between the growing iron oxide and the underneath layers [121], explaining the spallation of the Fe₂O₃ layer.

Oxidations of Al-free SS at 500 °C 1000 °C show similar oxide compositions at 800 °C. The oxide scales formed at 500 °C is thinner and at 1000 °C is thicker compared to oxidation at 800 °C.

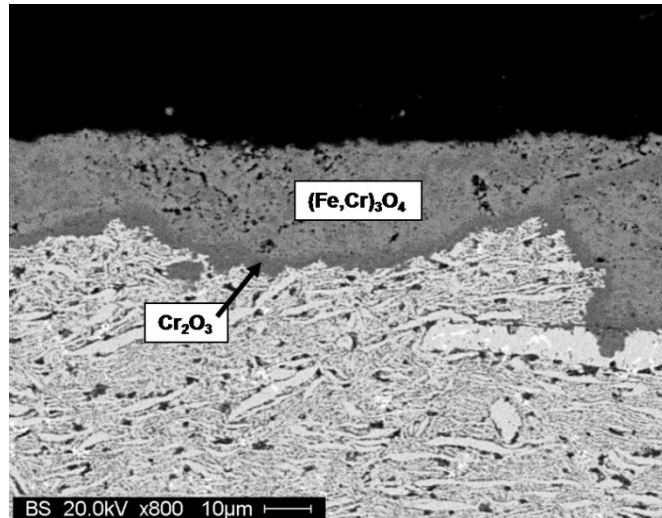


Figure 7.9 SEM micrograph of the oxide scale present for the nSS0Al after cyclic oxidation: 10 cycle of 50 hr holding time at 800 °C per cycle.

7.3.6 Oxidation of the Al-Containing Stainless Steel

Figure 7.10 shows the surface morphology developed on the nSS6Al coating. Qualitative EDS analysis of the oxide scale shows Al-Cr-O and the number of counts for Al is relatively small compared to the Cr signal, which suggest that a thin Cr_2O_3 oxide layer developed on the top of Al_2O_3 scale. The EDS analysis had not detected the presence of neither Fe nor Ni in the scale.

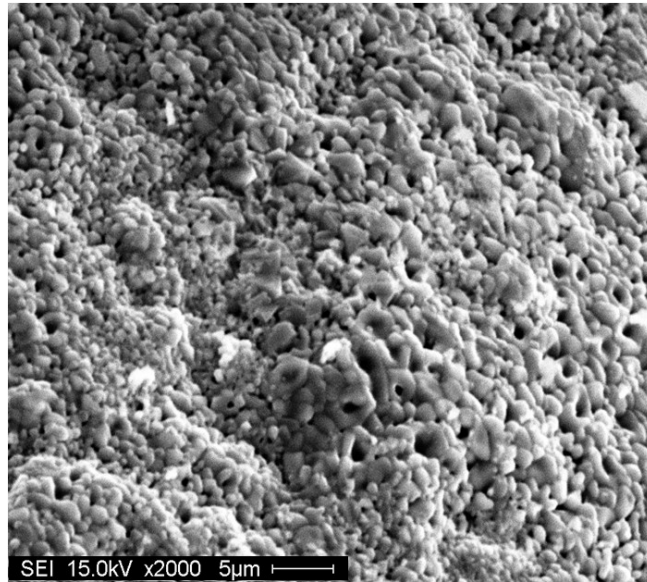


Figure 7.10 SEM micrograph of the surface scale for the nSS6Al system after oxidation of 200 hr at 800 °C.

As demonstrated before, the modification of the chemical composition by Al has shown to improve significantly the oxidation resistance of the base SS material. Figure 7.11 shows the microstructure of the scale developed after oxidation of 200 hr at 800 °C for the nSS6Al system and the corresponding line scan of the material. Results from the line scan of nSS6Al suggests Al_2O_3 forming around the particles within the coating and also show the double layers Al_2O_3 and Cr_2O_3 forming at the top surface of the coating from inner to outer, respectively. Oxidation of nSS2Al at 800 °C showed the formation of a non-continuous Al_2O_3 scale at the metal oxide interface, which allowed Fe to diffuse and form with Cr outer Fe-Cr oxide layer. At 800 °C, the Al concentration in nSS6Al was sufficient to develop the continuous external Al_2O_3 and Cr_2O_3 scales, while 2 wt% Al was insufficient to create a similar diffusion barrier.

A cross section of the oxidation product for the nSS2Al oxidized at 1000 °C is shown in Figure 7.12 and demonstrated that a continuous Al_2O_3 scale can form for this particular oxidation condition. The conditions for the formation of a complete Al_2O_3 scale for the nSS2Al require grain size within the nano-regime and oxidation temperature around 1000 °C.

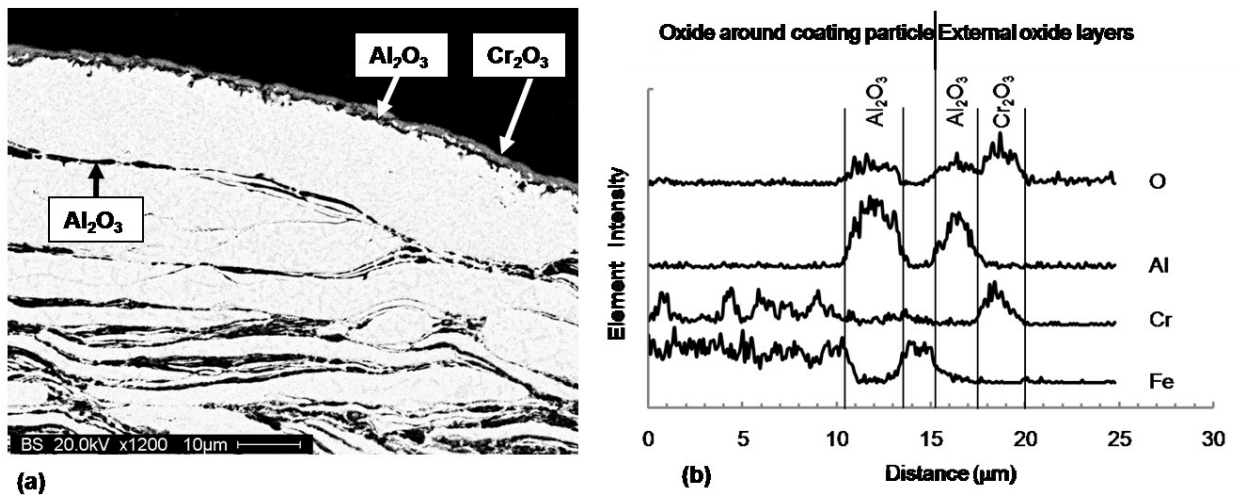


Figure 7.11 (a) SEM micrograph of oxide scales developed at 800 °C for nSS6Al (b) line scans illustrating layers of oxide scale presented in (a).

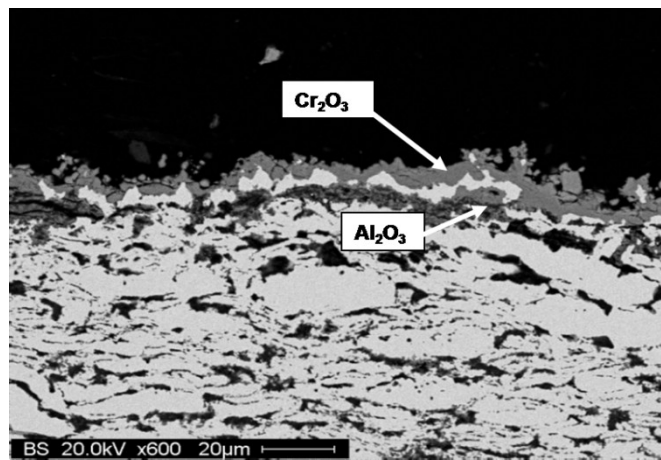


Figure 7.12 SEM backscatter electron micrograph of the cross-section of nSS2Al oxidized at 1000 °C showing the outer double oxide layers.

Theoretical calculations based on diffusion regarding the minimum Al solute concentration in a conventional grain size FCC based alloy is approximately 24 wt% at 800 °C and 6 wt% at 1000 °C to form external Al₂O₃ [96]. On the other hand, the thermodynamic predictions performed in this work, which are independent on diffusion, are predicting that for the SS2Al and SS6Al alloys, an Al₂O₃ scale should form and this, independently on the temperature. The discrepancy between the diffusion based value and the thermodynamic value is important for oxidation at 800 °C, as the Al content in SS6Al is four times lower than what is required according to diffusion theories. The significant increased in grain boundary present in nanomaterials is providing and increased number of traveling path for the Al solute to reach the surface when compared to what is available in conventional materials, for which diffusion would occurs through the lattice. Thus, the higher volume fraction of grain boundaries in nSS2Al and nSS6Al is the effective diffusion mechanism allowing the formation of the continuous external Al₂O₃ layer at 1000 °C for nSS2Al and at 800 and 1000 °C for the nSS6Al system. The results obtained in this study are supported by the work of He et al. [122] who showed that for a stainless steel containing 4.5 wt% Al and a grain size of 500 nm, a mixed scale of Cr, Al and O has develop at the surface of the coating during oxidation at 900 °C. For such grain size, a lower volume of grain boundary will be present and thus the lattice diffusion of the solute will be more important and thus the kinetic advantage found in nanomaterials is not observed due to the absence of the two layer-scale system. In addition, work performed by Adams et al. [123] regarding the oxidation of stainless steel 304L containing 3 wt% Al possessing a conventional micron-scale grain size at 600 °C and 1000 °C showed that

at both temperatures, the scale was composed of two layers, an outer layer composed of Cr-Fe-O and an inner layer containing Cr-Fe-Al-O.. In the present case, for a lower Al concentration, i.e. 2 wt%, the coating exhibited an Al₂O₃ forming during the oxidation at 500 °C and a two layers scale during oxidation at 1000 °C Al₂O₃ (inner layer and Cr₂O₃ outer layer). This comparison also demonstrate the effectiveness in the nanostructure coating to enhance diffusion of the solute Al atoms at the surface and provide oxide selectivity.

7.4 Conclusions

The results on the modification of the composition of 316LSS combined to a grain refinement to the nanometer level on the potential oxidation resistance improvement of coatings produced using the SPS technique is summarized as follows:

1. For the base SS316L alloy, the nanostructure enhance the oxidation activity at 500 °C, 800 °C and 1000 °C when compared to the micron-scale counterpart. The increased volume fraction of grain boundaries, responsible for the enhanced outward diffusivity, results in thicker oxide scales and Cr-enrich spinel phase ((Fe,Cr)₃O₄). On the other hand, the thickening of the scale combine to potential improved adhesion was found to increase the resistance to spallation caused by thermal cycling.

2. The modification of the based SS316L composition through the addition of 2 and 6 wt% Al combined to nanostructuring of the precursors increases significantly the resistance against high temperature oxidation through the initial formation of an Al₂O₃ layer. The combination of Al content and oxidation temperature dictated the scale composition. For the nSS2Al, the system was not able to develop a continuous Al₂O₃ scale at the interface, while it occurred during oxidation at 1000 °C. For the nSS6Al system, at 800 and 1000 °C, a two-layer scale was formed, composed of a continuous inner layer of Al₂O₃ and an outer layer of Cr₂O₃.
3. The activation energies for the development of the scale during oxidation for the nanostructured alloys: nSS (97 kJ/mol), nSS2Al (93 kJ/mol) and nSS6Al (85 kJ/mol) were found to be almost 50% lower than the conventional stainless steel (181 kJ/mol) due the higher volume fraction of high diffusivity paths through the grain boundaries and potential contribution of the dislocations mobility.
4. The calculated activation energies of phase transformation (90 kJ/mol) and oxidation (85 kJ/mol) for nSS6Al are similar. This result proposed that the two processes are interacted and have similar mechanism and suggest that the diffusion mechanism of cation and ion during oxidation for nSS, nSS2Al and nSS6Al in addition to the fast diffusion paths is catalyzed and accelerated by dislocation mobility during phase transformations when the coatings initially exposed to the high temperatures oxidation.

8. GENERAL DISCUSSION

8.1 Introduction

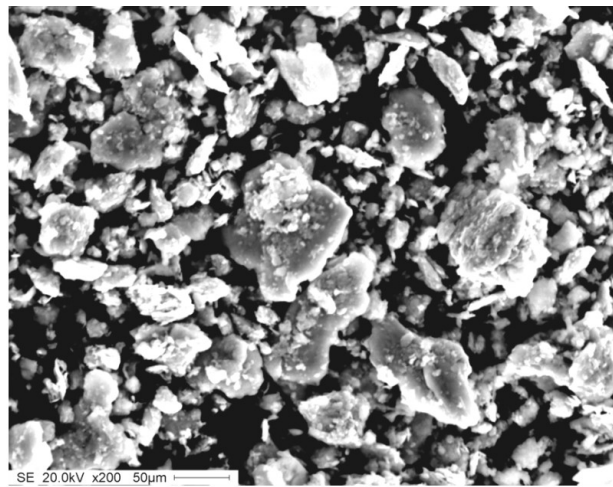
The microstructure evolution, the high temperature grain stability and oxidation of SS316L, SS316L containing 2 wt% Al and 6 wt% Al synthesized using cryomilling and consolidated using SPS were presented in the previous Results and Discussion Chapters. The present Chapter is a general discussion of the microstructure evolution and high temperature performance of the alloys studied in this work, in which the results were compared to some works that attempted to consolidate powders using hot pressing. A comparison of the performance of alloys reported in the literature, and manufactured from different synthesis and consolidation processes will also be discussed.

8.2 Mechanical Milling and Alloying using Cryomilling Versus other Ball Milling Processes

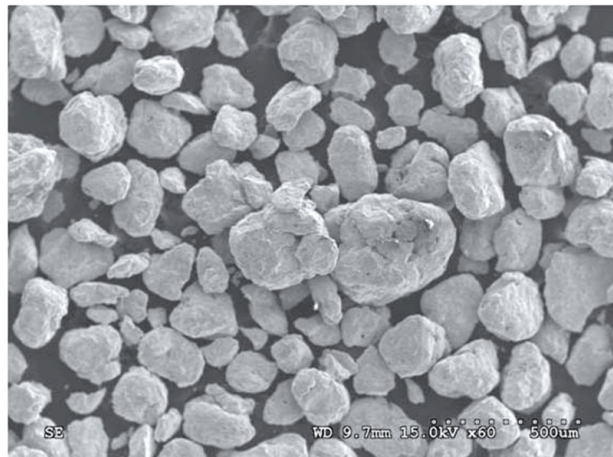
Cryomilling is a process that relies on severe plastic deformation for the formation of the nanocrystalline structure within the particles, which is similar to other ball milling operations. Exxon Research was the first developer of cryomilling. They indicated that

mechanical alloying of iron alloys in liquid nitrogen allowed much shorter milling times to reach a finer particle size and smaller grain sizes when compared to the mechanical alloying operation performed in air or in argon [124]. Figure 8.1 (a) and (b) present SEM micrographs showing (a) the powder morphologies of 316LSS after 32 hr of milling in liquid nitrogen, as studied in the present work and (b) for the same powder after 100 hr of Fritsch P5 planetary ball milling, as reported by Szymanska et al. [30]. The average particle size distribution for both starting powders for the two milling processes was about 50 μm . After cryomilling, the average particle size was 10 to 20 μm , while average particle size as large as 250 μm were obtained for the planetary milling. Regardless of the energy given to the process, cryomilling produces smaller milled powder particle. Due to the higher operating temperature, planetary ball milling has the tendency of forming larger agglomerates, which for the reported case, were 5 times larger than the average starting powders size. Cryogenic milling modifies the deformation mode of the particles so that they undergo enhanced fracture to smaller particle size before they are exposed to the large compressive strains inducing flattening and cold welding, leading to an increase in agglomerated particle size [10]. The efficiency to reduce the particle size is very low in a conventional ball milling. The mechanical energy is mostly lost through the generation of heat and thus, small amount is utilized in the elastic and plastic deformation of the powder particles [97]. The average crystalline grains size estimated from Sherrer formula for the 316LSS is 13 nm for the cryomilling process and 35 nm for the planetary ball milling.

Mechanical alloying during cryomilling is more effective than through other ball milling. The process can be completed in a shorter time due to the cryogenic environment that modifies the deformation mode and increases the exposed clean particle surfaces necessary for elemental diffusion during metal-to-metal contact [10]. Mechanical alloying of 316LSS blended with 2 and 6 wt% of Al was obtained after 32 hr of cryomilling, as presented and discussed in Chapter 4.



(a)



(b)

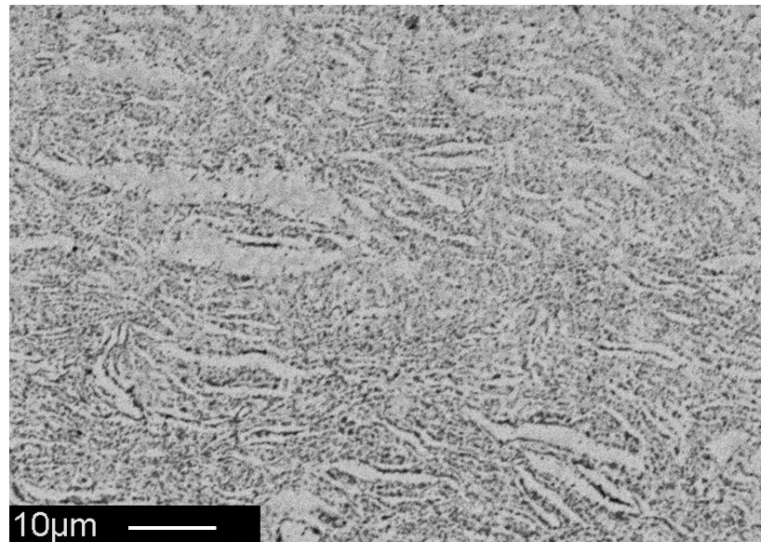
Figure 8.1 SEM images for 316LSS particle morphology (a) after 32 hr of cryomilling (b) after 100 hr of planetary ball milling [30].

8.3 Comparison between SPS and other Processes

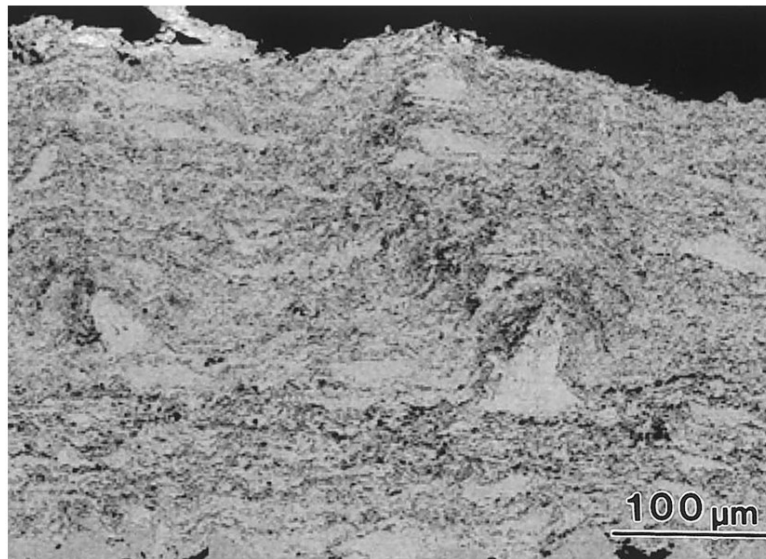
8.3.1 Microstructure Evolution during Processes Application

The properties of the coatings depend strongly on the microstructural evolution during the coating process. SPS coatings provide appropriate densification and limited grain growth compared to other coating processes. Figure 8.2 (a) shows SPS cladding made out of the cryomilled 316LSS powder, and for which the results were presented in a previous Chapter, while Figure 8.2 (b) shows a coating made out of cryomilled 316LSS deposited by high-velocity oxygen fuel spraying (HVOF) [12]. The cryomilled-SPS coating combination shows better microstructure integrity than the cryomilled-HVOF route, in term of porosities, hardness and purity. The hardness of SPS coating is 42% higher than for an SPS cladding made out of conventional 316LSS, while the hardness of the HVOF coating is 31% higher than the conventional 316LSS coating. The rapid consolidation process obtained through the SPS in the vacuum environment produces hi-quality coatings, free of second phase precipitation, as shown by the SEM and EDS analyses. The backscattered SEM micrographs reported for the cryomilled-HVOF combination revealed a higher level of second-phase particles present in the microstructure [12]. The second-phase precipitates were various oxide phases (Cr_2O_3 , FeO , Fe_2O_3 and $\gamma\text{-Fe}_2\text{O}_3$) embedded in the SS matrix, which were identified by selected area diffraction. This observation

suggested that in-flight oxidation have occurred during the spraying of the cryomilled feedstock [12].



(a)



(b)

Figure 8.2 Backscattered SEM image of a cross-sectioned 316LSS cryomilled coating produced by (a) SPS (b) HVOF [12].

Some attempts were made to consolidate the cryomilled powders by hot pressing for comparison purposes. The pressing parameters included a compaction force of 11-15 tons performed at 450°C in a mechanical vacuum environment. The cross-section of a consolidated SS2Al through hot pressing is shown in Figure 8.3. The measured level of porosity was 29% while it was 1.17% for SS2Al coating prepared by SPS as presented in Chapter 5. The consolidation of SS0Al, and SS6Al using hot pressing also showed a high level of porosity and apparent poor inter-particle bonding. The consolidation of hot compacts can be improved by increasing the consolidation pressure and temperature, which was limited by the existing hot press, and that may cause alteration of the grain size due to higher heat input imposed by this conventional process.

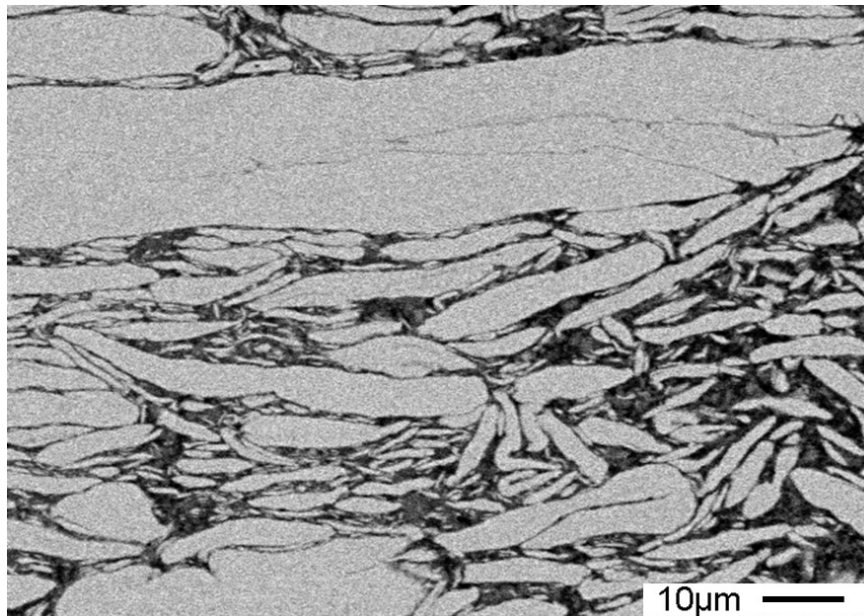


Figure 8.3 SEM image of a cross-sectioned SS2Al prepared by hot pressing.

8.3.2 Oxidation Behaviors

Oxidation behaviors and oxide morphologies for the nanostructured stainless steel and Al-containing stainless steel coatings produced by SPS were discussed in details in Chapter 7. Oxidation of wrought 316LSS at 1000 °C showed catastrophic oxidation when compared to what was observed for the 316LSS produced by SPS, as depicted in Figure 8.4 (a) and (b), respectively. This severe oxidation of the wrought 316LSS at 1000 °C is in part attributed to the high driving force that accelerate the outward Fe cation diffusion in an isotropic media before the complete formation of the inner Cr₂O₃ layer. The opposite behavior is occurring for the SPS coatings as the microstructure retards and controls the Fe outward diffusion prior of the formation of the inner protective Cr₂O₃ layer. The wrought 316LSS alloy possesses a cubic structure, in which the diffusion can be considered to occur in an isotropic medium, and thus independent of the directions. For the SPS coatings, after initial stages of oxidation and when the porosities in the coating matrix filled with oxide scale, a combination of diffusion mechanism is occurring, as there is bulk diffusion through the matrix of the coating and bulk diffusion through the reacted oxides, which is slower than for the metallic portion due to the nature of the atomic bonds, and thus begins to be influenced by orientation [125].

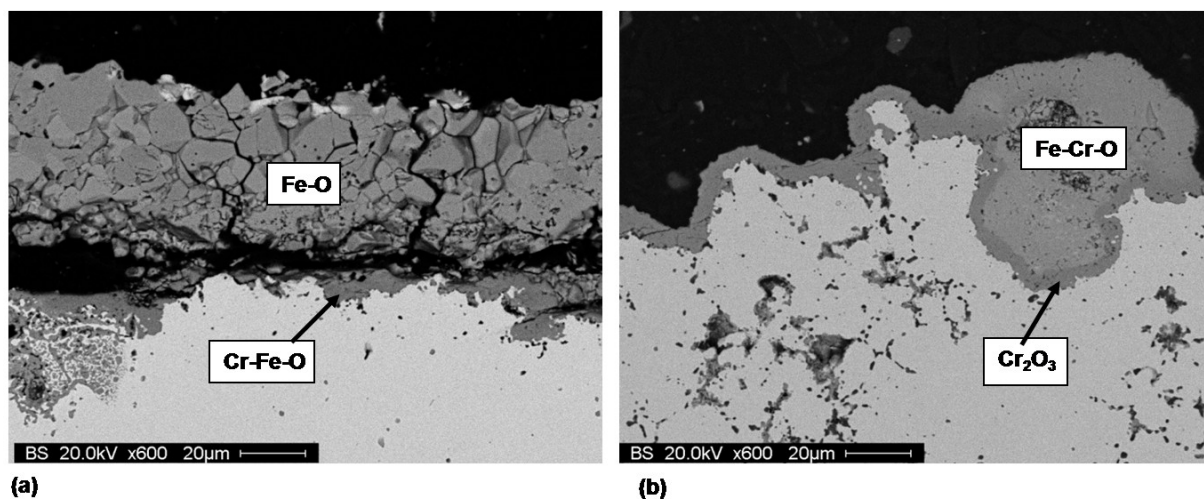


Figure 8.4 SEM micrograph of the oxide scale developed for 316LSS at 1000 °C showing the difference of oxidation behavior between (a) wrought alloy and (b) SPS coating.

Oxidation behavior of hot pressed samples showed an increase of oxidation of the individual particles, instead of showing the external oxide development occurring for the SPS coatings. This oxidation behavior is caused by the higher level of porosity and weak bonding between the particles detaching from one-another at high temperature. Figure 8.5 shows the oxide scale forming on a hot pressed sample oxidized at 800 °C for 48 hr. The SEM/EDS analysis showed that Fe-Cr-O oxides formed around the individual particles. A thinner inner Cr₂O₃ should surround each particle but was too thin to be detected by SEM/EDS. The oxidation treatment at 1000 °C of the hot pressed samples destroyed the integrity of the sample, as shown in Figure 8.6. This is associated with the stresses of thick oxide scale growing on each individual particles. Oxidation of hot pressed Al-containing stainless steel showed a behavior similar to the cryomilled powder particles, which results were presented and discussed in Chapter 6.

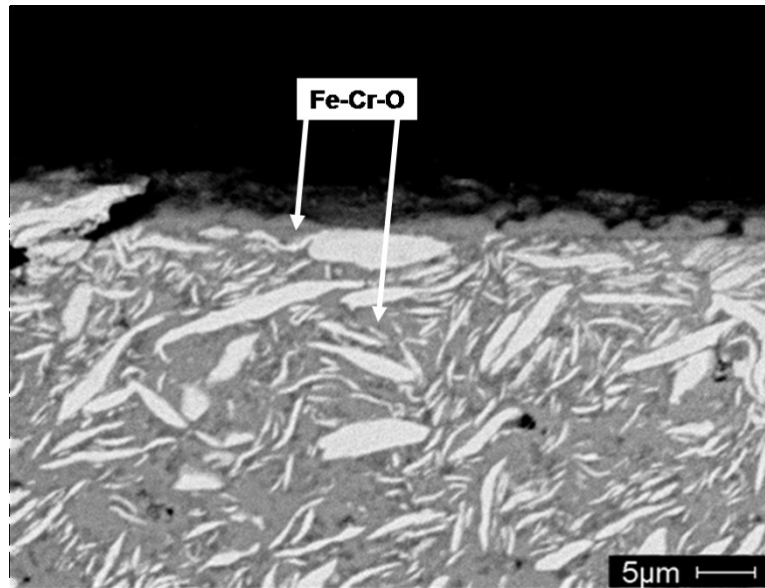


Figure 8.5 SEM micrograph of oxide scale forming at 800 °C for 316LSS hot pressed sample.



Figure 8.6 Hot pressed 316LSS samples oxidized at 1000 °C showing complete spallation of its structure.

9. GENERAL SUMMARY

The initial objectives of this research project were reached. The final goal of the project was to fabricate nanostructured stainless steel and Al-containing stainless steel coatings and evaluate their high temperature oxidation behavior for high temperature applications in oil and gas industries. Cryomilling was used to refine the grain size down to the nanometer level and to alloy the starting feedstock powders with Al to produce the two Al-containing alloys. The coatings were fabricated by SPS for which the conventional and nanostructured feedstock were sintered at the surface of a wrought stainless steel substrate. The oxidation performance of the coatings was studied. In addition to the oxidation performance, the effect of cryomilling, heat treatment and SPS process on the stability and transformation of the microstructure of the austenitic stainless steel and Al-containing stainless steel was investigated in this research project. The results from this project are summarized as follow:

1. The criterion for the engineering of Al-containing stainless steel was based on diffusion kinetic. Critical concentration of Al in the alloys to form Al_2O_3 was calculated for BCC and FCC base alloys as a function of temperature. The diffusion mechanism of Al was selected based on the microstructure and grain size. The theoretical Al concentration in the BCC base alloy was found to be 6 wt% to form protective Al_2O_3 at 800 °C and around 4 wt% at 1000 °C. In

comparison, the FCC structure required 4 times the amount of Al for the formation of the Al_2O_3 scale at 800 °C and 2 times for the formation of the Al_2O_3 scale at 1000 °C higher than the amount calculated for BCC structure. This due to the increased diffusivity of Al in a BCC structure when compared to a FCC structure. nSS2Al and nSS6Al were selected and studied throughout this research project. The selected Al concentrations were lower than the calculated critical concentration to form the Al_2O_3 scale, in order to determine the effect of the nanostructure on the reduction of the necessary Al concentration to form the selective Al_2O_3 oxide scale due to short-circuit outward diffusion of solute through the grain boundaries.

2. Nanocrystalline structure for nSS0Al, nSS2Al and nSS6Al was successfully produced by cryomilling after 32 hr of milling. The average grain sizes calculated using the Scherer equation from the respective diffraction patterns after 32 hr of milling were 13 nm for nSS0Al, 21 nm for nSS2Al and 25 nm for nSS6Al. The average grain size of the SS6Al cryomilled powders was verified by TEM and was found to be 6.7 nm. Mechanical alloying of Al for concentration of 2 and 6wt.% in 316LSS was successfully achieved after 32 hr of cryomilling.
3. Cryomilling of the three alloys resulted in a strain induced phase transformation from FCC to BCC. The strain induced phase transformation is influenced by the Al concentration, as the Al-containing stainless steel exhibited earlier strain induced transformation in the stage of milling, while the rate of transformation became similar thereafter for all systems.

4. The milled powders consisted of finely dispersed particles with the powder particle size distribution increasing with Al concentration. The coating morphology produced by SPS is entirely dependant on the morphology of the starting feedstock. Fully dense SPS coatings have been successfully produced with the three starting cryomilling powders. The nSS2Al and nSS6Al SPS consolidated coatings exhibit a lamellar structure due to the increased aspect ratio of the particles while the SS0Al coating yields an equiaxed structure due to the original particle morphology resulting from cryomilling.
5. The degree of the FCC recovery from the induced BCC structure during annealing at various temperatures differs for all three alloys. Complete recovery of the FCC phase was achieved between 565 and 594 °C for nSS6Al and 605 to 618 °C for nSS2Al, depending on the heating rate. Heat treatment up to 1000 °C for the SS0Al results in an incomplete recovery of FCC. The SPS process (950 °C for 2 min) was found to have a small influence on the BCC to FCC phase reversion when compared to the level of transformation induced during the heat treatment trials. The thermal load imposed by the SPS process was insufficient to provide the energy necessary to recover the FCC structure for the nSS0Al while 7 wt% FCC was recovered for SS2Al and 32 wt% FCC for nSS6Al during SPS consolidation.
6. Al enhances the reversion transformation from BCC to FCC for both SPS and heat treatment trials. The weight fraction of transformed FCC increases with the concentration of Al. The addition of Al increases in the overall Stacking Fault Energy (SFE) of the alloy, which results in faster austenite recovery.

7. During heating and SPS consolidation, two phenomenons are competing: grain growth of the nanostructure and the crystal structure reversion, which is driven by the SFE. From the nSS0Al results (lowest SFE of the three systems studied), it is suggested that the first event occurring is the growth of the BCC crystals up to approximately 100-110nm, followed by the crystal structure transformation towards the equilibrium FCC structure, which is then followed by further grain growth. As previously described, the presence of Al in the alloy causes increase of the SFE, which is believed to facilitate the crystal structure reversion. Thus, it is believed that the grain size at which the BCC to FCC transformation begins will be smaller than the Al-free system and the main coarsening of grain were achieved after the FCC recovery.
8. Oxidation of nanocrystalline nSS6Al cryomilling feedstock powders at 500 °C resulted in protective aluminum oxide scale formed at the surface. At 800 °C and 1000 °C, most of the nanocrystalline nSS6Al particles showed completed outer aluminum oxide scale. However, at 800 °C and 1000 °C, some particles showed growth of aluminum oxide and chromium oxide scales.
9. Oxidation resistance of coatings produced by SPS technique was investigated. For the base nSS0Al alloy, the nanostructure enhances the oxidation activity at 500 °C, 800 °C and 1000 °C when compared to the micron-scale counterpart. The increased volume fraction of grain boundaries, responsible for the enhanced outward diffusivity, results in thicker oxide scales and Cr-enriched spinel phase ((Fe,Cr)₃O₄). On the other hand, the thickening of the scale combined to

potential improved adhesion was found to increase the resistance to spallation caused by thermal cycling.

10. The modification of the based SS316L coating composition through the addition of 2 and 6wt%Al combined to nanostructuring of the precursors increases significantly the resistance against high temperature oxidation through the initial formation of an Al_2O_3 layer. The combination of Al content and oxidation temperature dictated the scale composition. For the nSS2Al, the system was not able to develop a continuous Al_2O_3 scale at the interface, while it occurred during oxidation at 1000°C . For the nSS6Al system, at 800 and 1000°C , a two-layer scale was formed, composed of a continuous inner layer of Al_2O_3 and an outer layer of Cr_2O_3 . The oxidation rate constant for the Al-containing stainless steel alloys studied was found to be lower than for the Al-free grades, which is associated with the Al_2O_3 layer providing a diffusion barrier.
11. The activation energies of phase transformation, grain growth and oxidation for nSS6Al alloy were calculated and found to be 90 kJ/mole, 126 kJ/mole and 85 kJ/mole, respectively. The calculated activation energies of phase transformation and oxidation were similar. This result proposed that the two processes are interconnected, have similar mechanism and suggested that the diffusion mechanism of cation and ion during oxidation for nSS0Al, nSS2Al and nSS6Al in addition to the fast diffusion paths is catalyzed and accelerated by dislocation mobility during phase transformations when the coatings are initially exposed to high temperature oxidation.

10. CONTRIBUTION TO THE ORIGINAL KNOWLEDGE

The main contributions of this research project to the original knowledge are summarized as follow:

- The systematic study demonstrates that the strain induced phase transformation occurring during cryomilling produces a FCC to BCC crystal structure change, and clarifies the discrepancy found in the literature surrounding the crystal structure of stainless steel obtained after deformation using mechanical milling.
- The work presents for the first time the effect of Al on the FCC to BCC strain-induced phase transformation during mechanical alloying and also its effect on the FCC recovery during heat treatment and powder consolidation using SPS.
- This research also demonstrates the relation and microstructure evolution between the phase transformation and grain growth of Al-free and Al-containing stainless steel during heat treatment and SPS consolidation.

- For the first time, Al-containing nanostructured stainless steel coatings manufactured by cryomilling and SPS promoting enhanced resistance against oxidation were produced.
- This project allowed the determination of the critical Al concentration to develop an Al₂O₃ scale during oxidation of stainless steel and proposed foundation for the engineering of improved nanostructured stainless steel alloys based on the relation between composition, grain size and operating conditions.
- This work also proposes an interaction mechanism between the solute diffusion during oxidation and dislocation mobility during BCC to FCC phase recovery for the selective oxidation behavior observed for these alloys.

REFERENCES

1. G. Lai, High Temperature Corrosion of Engineering Metals, Park OH, ASM International (1990).
2. M. Uunsitalo, et al., Materials Science and Engineering A 346 (2003) 168-177.
3. W. Quadackers, et al., Proceeding of the International Conference of Corrosion 1, (1998) 199-207.
4. R. Tems, A. Al zahrani, Saudi Aramco Journal of Technology summer (2006) 3-14.
5. W. Gao, L. Zhengwei, Mat. Res. 7 (2004) 175-185.
6. J. Picas, et al., Powder Technology 148 (2004) 20-23.
7. J. Schoenung, et al., Materials Forum 29 (2005) 414-419.
8. H. Fecht, Nanostruct Mater 6 (1995) 385-388.
9. Y. Xun, et al., Metall Mater Trans A 35 (2004) 573-581.
10. P. Gilman, Ann. Rev. Mater. Sci. 13 (1983) 279-300.
11. C. Suryanarayana, et al., Materials Science and Engineering A 304-306 (2001) 151-158.
12. L. Maggy, E. Lavernia, Materials Science and Engineering A 272 (1999) 222-229.
13. R. Perez, et al., NanoStructured Materials 7 (1996) 565-572.
14. M. Lau, et al., NanoStructured Materials 7 (1996) 847-856.
15. L. Ajdelsztajn, et al., Materials Science and Engineering A 338 (2002) 33-43.
16. D. Witkin, E. Lavernia, Progress in Materials Science 51 (2006) 1-60.

17. B. Huang, et al., *Materials Science and Engineering A* 225 (1998) 124-132.
18. K. Lo, Shek CH, Lai JKL et al., *Materials Science and Engineering R* 65 (2009) 65-131.
19. Ozsarac U, et al., *Materials & Design* 27 (2006) 69-73.
20. R. Latanision, A. Ruff, *Metallurgical Transactions* 2 (1971) 505-514.
21. M. Gonzalez, et al., *Materials Science and Engineering A* 343 (2003) 51-56.
22. M. Fujita, et al., *ISIJ International* 34 (1994) 697-703.
23. G. Frommeyer, et al., *ISIJ International* 43 (2003) 438-446.
24. Y. Han, S. Hong, *Materials Science and Engineering A* 222 (1997) 76-83.
25. A. Rohatgi, et al., *Metall. Trans. A* 32 (2001) 135-145.
26. J. Talonen, H. Hanninen, *Acta Materialia* 55 (2007) 6108-6118.
27. L. Bracke, et al., *Metallurgical and Materials Transactions A* 37 (2006) 307-317.
28. C. Rhodes, A. Thompson, *Metallurgical Transactions A* 8 (1977) 1901-1906.
29. H. Fujiwara, et al., *Scripta Materialia* 44 (2001) 2039-2042.
30. A. Szymanska, et al., *Rev. Adv. Mater. Sci.* 8 (2004) 143-146
31. M. Enayati, et al., *J Mater Sci* 42 (2007) 2844–2848.
32. M. Enayati, M. Bafandeh, *Journal of Alloys and Compounds* 454 (2008) 228-232
33. D. Oleszak, et al., *Journal of Alloys and Compounds* 434 (2007) 340-343.
34. H. Huang, et al., *Materials Science and Engineering A* 216 (1996) 178 – 184.
35. R. Davis, B. McDermott, C.C. Koch, *Matall. Trans. A* 19 (1988) 2867-2874.
36. H. Yang, P. McCormick, *J Soild State Chem.* 107 (1993) 258-263.
37. A. Chen, et al., *Surface & coatings Technology* 201 (2007) 7462-7466.

38. F. Bernard, J. Niepce, Nanomaterials and nanochemistry book, SpringerLink, 2008, p. 489-495.
39. M. Tokita, J. Soc. Powder Technol. 30 (1993) 790-804.
40. M. Omori, J. Jpn. Soc. Powder Metallurgy 45 (1998) 1055-1060.
41. N. Hong-wei, N., H. Hang, L. Guang-qiang, L. Jing, J. of Iron and Steel Research 15 (2008) 73-76.
42. M. Omori, Materials Science and Engineering A 287 (2000) 183-188.
43. Eugene, S. Kandukuri, L. Froyen, Journal of Applied Physics 102 (2007) 114913-114913-12.
44. O. Yanagisawa, H. Kuramoto, K. Matsugi, M. Komatsu, Materials Science and Engineering A 350 (2003) 184-189.
45. W. Chen, U. Anselmi-Tamburini, J.E. Garay, J.R. Groza, Z.A. Munir, Materials Science and Engineering A 394 (2005) 132-138.
46. A. ZuNiga, L. Ajdelsztajn, A. Lavernia, Metallurgical And Materials Transactions A 37 (2006) 1343-1352.
47. G. Xie, O. Ohashi, N. Yamaguchi, A. Wang, Metallurgical And Materials Transactions A 34 (2003) 2655-2661.
48. A. Khanna, Introduction to high temperature oxidation and corrosion, Materials Park (OH): ASM, 2002.
49. P. Kofstad, High Temperature Corrosion, Elsevier Applied Science Publishers Ltd, New York, 1988.
50. R. Davis, Heat-Resistant Materials, Materials Park (OH): ASM, 1997.

51. N. Birks, G. Meier, Introduction to High Temperature Oxidation of Metals, Edward Arnold (Publishers) Ltd., London, 1982.
52. X. Peng, J. Yan, Y. Zhou, F. Wang, Acta Materialia 53 (2005) 5079-5088.
53. Y. Ishikawa and T. Yoshimura, J. Vac. Sci. Technol. **13** (1995) 1847-1852.
54. N. Yoshimura, H. Hirano, T. Sato, I. Ando and S. Adachi, J. Vac. Sci. Technol. **9** (1991), 2326-2330.
55. S. Ohkido, Y. Ishikawa and T. Yoshimura, Appl. Surf. Sci. **76-77** (1994) 261-265.
56. I. Saeki, H. Konno and R. Furuichi, Corros. Sci. **38** (1996) 19-31.
57. S. Shibagaki, A. Koga, Y. Shirakawa, H. Onishi, H. Yokokawa and J. Tanaka, Thin Solid Films **303** (1997) 101-106.
58. Vesel, M. Mozeti, A. Zalar, Applied Surface Science 200 (2002) 94-103.
59. V.Trindade, U. Krupp, B. Hanjari, S.Yang, H. Christ, Materials Research 8 (2005) 371-375.
60. J. Nychka, and D. Clarke, Oxidation of Metals 63 (2005) 325-352.
61. G Wood, Oxidation of Metals 2 (1970) 11-59.
62. I. Wolff, L. Iorio, T. Rumpf, P. Scheers, H. Potgieter , Materials Science and Engineering A 241 (1998) 264-276.
63. K. Wambach, J. Peters, H. Grabke, Materials Science and Engineering 88 (1987) 205-212.
64. N. Belen, P. Tomaszewicz, D. Young, Oxidation of Metals 22 (1984) 227-245.
65. V. Ramakrishnan, J. McGunty, N. Jayaraman, Oxidation of Metals 30 (1988) 185-200.
66. C. Barrett, J. Johnston, W. Sanders, Oxidation of Metals 12 (1978) 343-377.
67. C. Rawers, D. Larsont, Oxidation of Metals 27 (1987) 103-120.

68. X. Jun-huai, *Trans. Nonferrous Met. Soc of China* 16(2006) s829-s833.
69. J. Dunning, D. Alman, J. Rawe rs, *Oxidation of Metals* 57 (2002) 409-425.
70. Y. Yamamoto, M. Brady, Z. Lu, P. Maziasz, C. Liu, B. Pint, K. More, H. Meyer, E. Payzant, *Science* 316 (2007) 433-436.
71. F. Stott, G. Wood, F. Golightly, *Corrosion Science*, 19 (1979) 869-887.
72. J. Stringer, G. Wright, *Oxidation of Metals* 5 (1972) 59-84.
73. C. Giggins, F. Pettit, *Trans. TMS-AIME* 245 (1969) 2495-2507
74. F. Wang, *Oxidation of Metals* 48 (1997) 215-224.
75. F. Tang, L. Ajdelsztajn, J. Schoenung, *Oxidation of Metals*, 61 (2004) 219-238.
76. G. Chen, H. Lou, *Oxidation of Metals* 54 (2000) 155-162.
77. B. Cullity, *Elements of x-ray diffraction*, Addison-Wesley Publishing Company, Inc, (1978) p. 410.
78. L. Van Vlack, *Trans. AIME* 191 (1951) 251-259.
79. D. Birnie, E. Machlin, L. Kaufman, K. Taylor, *Calphad* 6 (1982) 93-126.
80. L. Li, B. De Cooman, P. Wollants, Y. L. He, X. D. Zhu, *J. Mater. Sci. Technol.* 20 (2004) 135-138.
81. D. C. Madeleine, *Microstructure of steels and cast iron*, Springer (New York), (2004) p. 306.
82. Z. Guo, W. Sha, D. Li, *Materials Science and Engineering A* 373 (2004) 10-20.
83. *Metals Handbook*, Materials Park (OH), ASM International (1990) p. 1119.
84. M. Murayama, K. Hono, H. Hirukawa, T. Ohnuma, S. Matsuoka, *Scripta Materialia* 41 (1999) 467-473.
85. R. Schramn, R. Reed, *Metallurgical Transactions A* 6 (1975) 1345-1351.

86. K. S. Vecchio, R. W. Hertzber, *Journal of Materials Science* 23 (1988) 2220-2224.
87. E. Mazancova, Z. Jonsta, K. Mazanec, *Archives of Materials Science* 28 (2007) 90-94.
88. M. Polcarova, J. Zura, *Czechoslovak Journal of Physics* 27 (1977) p. 322.
89. E. Mittemeijer, L. Chang, P. Schaaf, *Metallurgical Transactions A* 17 (1986) 1441-1445.
90. L. Cheng, C. M. Brakman, B. M. Korevaar and E. J. Mittemeije, *Metallurgical Transactions A* 19 (1988) 2415-2426.
91. K. H. Chung, R. Rodriguez, E. J. Lavernia, J. Lee, *Metallurgical and Materials Transactions A* 33 (2002) 125-134.
92. A. Belyakov, T. Sakai, H. Miura, R. Kaibyshev, K. Tsuzakie, *Acta Materialia* 50 (2002) 1547-1557.
93. D.H. Trinh, K. Back, G. Pozina, H. Blomqvist, T. Selinder, M. Collin, I. Reineck, L. Hultman, H. Hogberg, *Surface & Coatings Technology* 203 (2009) 1682-1688.
94. Y. Wu, Y. Zhang, G. Pezzotti, J. Guo, *Materials Letters* 52 (2002) 366-269.
95. C. Stosiek, S. Brehme, G. Scholz, E. Kemnitz, *Journal of the European Ceramic Society* 29 (2009) 2713-2720.
96. A. Almathami, E. Elhachmi, M. Brochu, *J. Mater Sci.* 43 (2008) 3452-3458.
97. C. Surynarayana, *Progress in Materials Science* 46 (2001) 1-184.
98. A. Almathami, G. Goodall, M. Brochu, *Materials Science and Engineering A* (2010).
99. A. Bautista, F. Velasco, M. Campos, M. Rabanal, J. Torralba, *Oxidation of Metals* 59 (2003) 373-393.
100. J. Benjamin, M. Bomford, *Metall. Trans. A* 8 (1977) 1301-1305.

101. P. Gilman, W. Nix, Metall. Trans. A 12 (1981) 813-824.
102. I. Ucok, T. Ando, N. Grant, Materials Science and Engineering A 133 (1991) 284-287.
103. F. Stott, and F. Wei, Oxidation of Metals 31 (1989) 369-391.
104. M. Gemmaz, et al., Surface Science Letters 227 (1990) L109-L111.
105. R. Nakamura, et al., Intermetallics 10 (2002) 195-204.
106. A. Pivkna, et al., Journal of Materials Science 39 (2004) 5451-5453.
107. Handbook of X-ray Photoelectron Spectroscopy, Perkin-Elmer Corporation, (1992) p. 44.
108. G. Gewinner, et al., Surface science 78 (1978) 439-458.
109. E. W. Hart, Acta Metall., 5, (1957) p. 597.
110. A. Khanna, Introduction to high temperature oxidation and corrosion, Materials Park (OH): ASM, 2002, p. 122.
111. C. Bale, et al., Calphad, 33 (2009) 295-311
112. P. Kofstad, High Temperature Corrosion, Elsevier Applied Science Publishers Ltd, New York, 1988, p. 259.
113. P. Kofstad, High Temperature Corrosion, Elsevier Applied Science Publishers Ltd, New York, 1988, p. 18.
114. N. Birks, G. Meier, Introduction to High Temperature Oxidation of Metals, Edward Arnold (Publishers) Ltd., London, 1982, P.54.
115. A. Khanna, Introduction to high temperature oxidation and corrosion, Materials Park (OH): ASM, 2002, p. 52.
116. A. Almathami, M. Brochu, Journal of Materials Processing Technology (2010).

117. H. Khatak, B. Rag, Corrosion of Austenitic Stainless Steel: Mechanism, Mitigation and Monitoring, Woodbead Publishing, Cambridge, 2002, P.273.
118. M. Carbuicchio, et al., Hyperfine Interactions 141/142 (2002) 403–408.
119. A. Hansson, et al., Oxidation of Metals 73 (2020) 289-309.
120. M. Sun, X. Wu, E. Han, J. Rao, Scripta Materialia 61 (2009) 996-999.
121. N. Birks, G. Meier, Introduction to High Temperature Oxidation of Metals, Edward Arnold (Publishers) Ltd., London, 1982, P.118.
122. K. He, H. Gong, K. Zeng, Z. Li , W. Gao, Materials Letters 46 (2000) 53-59.
123. T. Adams, P. Korinko, A. Duncan, Materials Science and Engineering A 424 (2006) 33-39.
124. R. Petkovic-Luton, J. Vallone, Exxon Research and Engineering Company, Florham Park, NJ, United States of America, US Patent Number 4619699; 1986.
125. H. Mhrer, Diffusion in Solid: Fundamentals, Methods, Materials, Diffusion-Controlled Process, Springer Berlin Heidelberg New York, 2007.

APPENDIX A

Determine the Critical Concentration of Aluminum to Form Al_2O_3

The critical concentration of Al is given by:

$$N_{Al} = \frac{v}{z_{Al} M_0} \times \left(\frac{\pi k_p}{D} \right)^{\frac{1}{2}}$$

z_{Al} is the valence of the Al atoms (3)

M_0 is the atomic weight of oxygen (16, g/mol)

The calculation is for ferritic steel and similar calculation was done for austenitic stainless steel.

Molar volume v

Element	Wt. %	MW (g/mol)	Density (g/cm ³)
Fe	0.84	55.8	7.87
Cr	0.1	52	7.19
Al	0.06	26.98	8.9

Average MW (g/mol)	53.7
Average Density (g/cm ³)	7.5
Molar volume v (cm ³ /mol)	7.167

Diffusion Coefficient of Al, D

$$D = D_0 \exp\left(\frac{-Q}{RT}\right), D_0 = 5.13 \times 10^{-4} \text{ cm}^2/\text{s}, Q = 196.5 \text{ kJ/mol.}$$

Parabolic Rate Constant for Aluminum Oxide, k_p

The parabolic rate constant of Al oxide as a function of temperature can be obtained from the below Figure [51].

